Self-Consistent *Ab Initio* Embedding Results for Real Materials

by

Runxue Yu

A dissertation submitted in partial fulfillment
of the requirements for the degree of
Doctor of Philosophy
(Physics)
in the University of Michigan
2024

Doctoral Committee:

Professor Emanuel Gull, Chair
Assistant Professor Na Hyun Jo
Professor Kai Sun
Professor Dominika Zgid

Runxue Yu
runxueyu@umich.edu
ORCID iD: 0000-0002-7509-9514

© Runxue Yu 2024

Acknowledgments

I am filled with profound gratitude as I acknowledge the individuals who have contributed significantly to my journey, propelling me towards the completion of this PhD thesis. Their unwavering belief in my abilities, support, and mentorship have made this accomplishment possible.

First and foremost, I express my deepest gratitude to my advisor, Professor Emanuel Gull. His expert advice and guidance have been invaluable throughout my research. His support has not only enriched my academic pursuits but has also significantly impacted my personal and professional life.

I am equally grateful to my co-advisor, Professor Dominika Zgid. Her guidance, shared experience, and constant support have been instrumental in my journey. Her steadfastness during tough times was a beacon of hope that kept me going.

I would like to extend my heartfelt thanks to the Gull and Zgid groups, particularly Dr. Chia-Nan Yeh, whose assistance with the real material calculation framework was fundamental to my research. His attention to detail in simulations and discussions on my project were immensely helpful. My gratitude also goes to Dr. Sergei Iskakov, whose technical and coding prowess made a significant impact on my work. My sincere thanks to Dr. Yanbing Zhou for her invaluable collaboration and to Dr. Xinyang Dong and Lei Zhang for their constant support, both academically and personally. I am also appreciative of the support and interactions with my other colleagues: Thomas Blommel, Yang Yu, Dr. Jia Li, Dr. Pavel Pokhilko, and Dr. Andre Erpenbeck.

My appreciation extends to my committee members, Professor Kai Sun and Professor Na Hyun Jo. Their time, constructive feedback, and insightful comments have greatly helped refine my thesis.

I am also incredibly grateful for the companionship and support of my friends, Dr. Yuewei Wen, Dr. Yudan Liu, Meichen Liu, Yichen Liu, Yuhan Peng, Dr.Heqiu Li, Dr. Siwen Li and Dr. Harold Liu. Our shared moments of laughter, stress, and triumph

have been among the most memorable aspects of my graduate life.

Lastly, to my parents and my cousin, Shi Yu, words cannot express my gratitude for your unwavering love and support. You have given me the strength to persevere, even when the odds were stacked against me. Your belief in me has been a driving force behind my achievements.

In conclusion, I consider myself fortunate to have been surrounded by such a supportive and inspiring group of people during my PhD journey. Your collective wisdom, kindness, and friendship will forever be treasured.

Table of Contents

List of Figures

List of Tables

List of Acronyms

AO atomic orbital.

BZ Brillouin zone.

CI configuration interaction.

DFT Density Functional Theory.

DIIS direct inversion in the iterative subspace.

DMFT Dynamical mean-field theory.

ED Exact Diagonalization.

GDF Gaussian density fitting.

GF2 self-consistent second-order Green's function method.

GGA gradient-corrected approximation.

GS ground-state.

GTO Gaussian-type orbital.

HF Hartree-Fock.

HK Hohenberg-Kohn.

KS Kohn-Sham.

LCAO Linear Combinations of Atomic Orbitals.

LDA local-density approximation.

MaxEnt Maximum Entropy Method.

MBPT many-body perturbation theory.

MLWF maximally localized Wannier functions.

MP2 Møller-Plesset second order.

PAW Projector Augmented Wave.

PBE Perdew-Burke-Ernzerhof.

SAO symmetric atomic orbitals.

sc*GW* self-consistent GW.

SCF self-consistent field.

SEET self-energy embedding theory.

TDDFT time-dependent density functional theory.

VASP Vienna ab initio simulation package.

xc exchange-correlation.

Abstract

This thesis focuses on applying self-consistent embedding methods to strongly correlated materials. The ab initio simulation of periodic solids with strong correlation is an active area of research, since reliable parameter-free methods exist only for weakly correlated solids, which are less suitable where the independent electron approximation fails. We report a calculation framework from a fully self-consistent parameter-free ab initio self-energy embedding theory (SEET) consisting of a weakly correlated environment (treated at the level of GW) and strongly correlated orbitals (treated with Exact Diagonalization). Unlike previous work, the theory does not require any adjustable parameters and is fully ab initio, while being able to treat both the strong correlation and the nonlocal screening physics of these materials. Importantly, our method is applied to real materials with not only transition metal d orbitals but also rare-earth element f orbitals to obtain information about the spectral function and thermodynamic properties, which can be compared with experimental measurement. Real materials of my interest are the parent compound of a recent discovered superconductors, namely $NdNiO_2$, whose intrinsic mechanism remain as a hot topic in condensed matter. Analysis of these materials includes, besides spectral function, the optical properties of the solids, which are related directly to the experimental observations.

Chapter 1

Introduction

It has been difficult to theoretically describe strongly correlated materials. Condensed matter physics have substantial difficulties when dealing with strongly correlated systems, such as materials containing transition metal atoms. Since both the strong and weak correlations between electrons must be taken into account, a quantitative description of these systems is challenging. The interaction of subtle electronic correlation effects on low energy scales is the root cause of many of their intriguing features. The primary factor making it difficult to describe these systems is the interaction between the localized and delocalized electrons. In order to get thermodynamic quantities and spectra, a computational approach must take into consideration both itinerant and localized electrons that are present in a material.

Our calculation framework follows a fully self-consistent parameter-free ab initio self-energy embedding theory (SEET) [1–6]. This method combines a diagrammatic perturbative theory, i.e., the GW approximation [7, 8], with nonperturbative solution of quantum impurity solvers. Due to the perturbative nature of the GW approximation, only the weak correlation regime is reliably accessible with the method. But unlike other embedding methods such as a combination of the Dynamical mean-field theory (DMFT) [9–11] with Density Functional Theory (DFT) [12], the fully self-consistent GW approximation is free from adjustable parameters and double counting correction and independent of a choice of functional. In addition, its expression in diagrammatic language makes the method is suited to embedding theory. In order to go beyond the weakly correlated regime, embedding theory solves nonperturbative strong-correlation problem in a small but potentially strongly correlated subset of orbitals, using the so-

lution from the GW approximation as a weakly correlated environment. Consequently, SEET is a hybrid approach where we use two Green's function methods, one is strongly correlated and another one is weakly correlated. In their Green's function language, it is possible to calculate experimentally observable quantities such as the spectral function, realizing the comparison between computational calculations and experimental observation.

Our main goal is to study the real materials following the above framework. A solid can be modeled as a periodic arrangement of atoms in a Bravais lattice, described by a basis of single-particle Bloch-wave function under the Born-Oppenheimer approximation. In our work, we use a finite basis of Gaussian functions to construct Bloch waves [13–16]. Since it is difficult to assess the Gaussian basis functions independently, we compare the results of simple DFT calculations in this basis from a Python package PySCF [15, 17] with those obtained in a plane-wave code called Vienna ab initio simulation package (VASP) [18, 19]. Meanwhile, the DFT solution can also provide an initial guess to the GW approximation. Then we solve the system in the fully self-consistent finite temperature GW approximation introduced by Hedin [7]. Based on the weakly-correlated environment from the GW approximation, SEET with Exact Diagonalization (ED) as the impurity solver is iterated fully to self-consistency.

At present, embedding methods for treating realistic problems can be applied to perform calculations for systems with relatively complicated electronic structure such as transition metal oxide [6, 20–23] or oxide perovskites [24–26]. Most commonly, only the local transition metal d orbitals in cubic geometry are embedded as impurity problems containing the t_{2g} and e_g orbitals in order to achieve a good comparison with experiments [6, 26]. Therefore, we choose to apply our methods to the superconductor $NdNiO_2$ [27–29], where not only the transition metal Ni d orbitals but also the rare-earth element Nd f orbitals make great contribution to characteristics of the electronic structure. Due to self-interaction errors, rare-earth element f electrons are not handled well by traditional methods and the only way to cope with it is to place the $4f$ electrons in the core [30]. In our method, Nd f electrons are also placed in the valence basis and are important objects of research.

Besides its capability of showing the reliance of our calculation framework, $NdNiO_2$ has also attracted much attention due to the recent discovery of superconductivity in Sr-doped $NdNiO_2$ [27]. The interest of investigating this material is motivated by cuprates,

a family of high temperature superconductors [31, 32]. The quasi-two-dimensional $d_{x^2-y^2}$-dominiated electronic structure in copper oxide (CuO_2) planes is believed to be crucial to the high transition temperature [33]. This discovery has motivated the study of compounds with similar crystal and electronic structure, with the aim of finding additional superconductors and understanding the origins of copper oxide superconductivity. Since nickel is just besides copper in the periodic table, it becomes a promising candidate for constructing a kind of nickel oxide planes with superconductivity [34, 35]. Harold Hwang and colleagues [27] have reported the observation of superconductivity in an infinite-layer nickelate that is isostructural to infinite-layer copper oxides.

Since most correlations in $NdNiO_2$ are not qualitatively captured by the weakly correlated method, an outer-loop self-consistency connecting weak and strong correlation [36] is considered to improve the calculation, which helps relax the weakly correlated orbitals in the presence of strong correlation coming from impurity orbitals. In the outer loop of SEET, we use the converged Green's function that contains the self-energy obtained by impurity solvers and pass it back to the GW approximation as a zeroth-order Green's function. Then GW prepare a modified weakly correlated solution and inner-loop SEET is iterated fully to self-consistency. These procedures are repeated until the outer-loop self-consistency is achieved. Due to the self-consistent nature of the loop, the converged GW Green's function will be consistent at the end.

In the Green's function language, it is easier to perform calculations with imaginary time and Matsubara quantities than real time and real frequency ones. So what we obtained from numerical simulations are Matsubara quantities. To compared with experimental measurements, analytical continuation [37] is required to obtain real axis quantities from Matsubara ones. Two methods are applied for this purpose: one is MaxEnt [38–40], and another one is Nevanlinna analytical continuation [41]. From our data, Nevanlinna method, together with Wannier interpolation [42], give momentum-resolved spectral function near Fermi energy with higher resolution.

Besides spectral function, the optical properties of solids are also common and direct observations in experiments. Experiments on optical reflectivity, transmission and refraction provide the way to determine the dielectric constant and the optical conductivity of the solid, which is of much significance for the quantitative determination of the electronic band structure of the solids. From numerical perspective, we are encouraged to derive the optical conductivity for real materials in Green's function language

from lowest order to higher order, in order to compare with the experimental data. The optical conductivity in Gaussian-type Bloch wave basis at lowest order is derived from linear response theory. Further investigation is promising to implement.

In this thesis, we will proceed as follows: In Chp. 2, we overview the existing methods on real material calculation and point out the advantages and limitations of each method. Then in Chps. 3-5, the methodology of the calculation framework will be presented, where the background of DFT is shown in Chp. 3, many-body perturbation theory (MBPT) is introduced in Chp. 4 and the quantum embedding theory is discussed in Chp. 5. After that, Chp. 6 explains the required techniques to obtain momentum-resolved spectrum and thermodynamic quantites. Then, the theory of optical conductivity in real materials is derived in Chp. 7. Finally, the implementation of the above calculation framework on $NdNiO_2$ is demonstrated in Chp. 8.

Chapter 2

Motivation

In this chapter, we will overview the existing methods on real material calculations, especially the ones dealing with the strongly correlated systems, and discuss the merits and limitations of each method.

In order to quantitatively describe the strongly correlated systems, it is important to treat both strong and weak correlations simultaneously. Two typical conceptual approaches are used here: one is processing the entire system by means of significant approximation of correlated effects, while the other one is construction of the model system with a reduction to a few "relevant" degrees of freedom or essential orbitals near the Fermi level.

DFT [12], as a typical example of the first approach, has revolutionized the way we deal with the many-electron problem. It can be considered to be a generally accepted model of condensed matter physics due to the low computational cost. However, DFT is well known to fail to treat strong correlations properly and is difficult to identify the most suitable method for a particular application [43].

Green's function formalism provides an extensive series of many-body perturbation theories (MBPTs) for the first approach beyond DFT. It accounts for electron correlation by treating it as a perturbation to the Hartree-Fock wave function [44]. To the first order approximation, the Hartree-Fock (HF) theory enables one to determine the best set of single particle states that is optimized for each Hamiltonian and for a given number of particles. Its computational efficiency enables it to provide a good starting point for more accurate methods. But its disability of taking the effects of electron correlation beyond the mean-field theory allows for the exploration of the higher-order approximations,

such as the self-consistent second-order Green's function method (GF2) [45–48] and the self-consistent GW (scGW) approximation [7]. They are believed to be more accurate in predicting the band gaps than DFT. GF2 is computationally less expensive than GW and can be used to study larger systems. GW is more accurate than GF2 for strongly correlated systems but is computationally more expensive. In spite of their theoretical merits, the applications of scGW and GF2 are typically orders of magnitude more expensive than those of DFT, which prohibit straightforward applications of realistic materials [49].

Instead of treating the full Hamiltonian with potentially severe approximations to electron correlations as the first approach states, the second approach can yield precise results for the effective model systems. ED [50–53], for example, has been used early on as a solver for the Anderson impurity model. The ED method works on a finite Hamiltonian whose size is the limiting factor for its applicability. Hence, the effective hybridization function needs to be "discretized", i.e., the number of energy levels of the bath needs to be finite and small, while it is infinite in the thermodynamic limit [54]. When used in realistic systems, the construction of the parameters of the effective model accounts for significant uncertainties and potential sources for errors.

In the presence of strong electron correlations, quantum embedding theories combine the best aspect of the above two approaches, by solving the systems using DFT or MBPT and construct a model system based on the results. DMFT and its variants are such a widely used method. Ordinary DMFT [9–11] schemes assume the lattice self-energy to be a momentum-independent quantity so that a many-body lattice problem can be mapped to a many-body local problem. This approximation becomes exact in the limit of lattices with infinite coordination and then constrains the application of DMFT to the situation where the interactions are predominantly local and self-energy contributions from non-local terms (in both interactions and propagators) are negligible [1].

LDA+DMFT is a technique that combines DFT and DMFT to account for non-local correlation between unit cells [55, 56]. It has been widely used to describe strongly correlated materials, as shown in References. [56–58]. However, The DFT component cannot be improved in a systematic manner, and LDA+DMFT is plagued by the issue of double counting. Additionally, on-site Coulomb interactions are adjusted to fit experiments empirically, which is used to parameterize the impurity Hamiltonian in

LDA+DMFT [59].

A combined GW+DMFT [60, 61] was introduced several years back with a view to avoiding ad hoc nature of the Hubbard parameter and double counting arising out of traditional LDA+DMFT combinations. This scheme inherits the virtues of its two parent theories: a good description of the local low energy correlation physics encoded in a renormalized quasi-particle band structure, spectral weight transfer to Hubbard bands, and the physics of screening driven by long-range Coulomb interactions [61]. In practice, numerous technical and theoretical limitations exist. It is extremely technically difficult to achieve a fully consistent solution for the GW problem. The various approximations employed (quasi-particles, no full self-consistency, etc) at the level of GW along with the difficulty of numerically solving multi-orbital impurity problems with general non-local time-dependent interactions means that the rigorous diagrammatic footing described above is severely approximated in practical implementations of the GW+DMFT method [62].

Chapter 3

Density Functional Theory

Prior to the 1960s, approximate methods, such as the Hartree approximation [63], were generally used to calculate the electron junction of condensed matter systems. Although these methods have certain limitations, they still provide tools for relevant research. In the 1960s, Kohn and his collaborators proposed density functional theory (DFT) [64, 65] and established the Kohn-Sham equation, which, combined with the local density functional approximation, laid the foundation for modern electronic structure calculations. For this, Kohn and Pople, the founder of computational chemistry, shared the 1998 Nobel Prize in Chemistry. With the continuous development of density functional theory and the progress of computational methods and computer performance, computational condensed matter physics has gradually shifted from the qualitative interpretation of experimental data to the quantitative prediction of physical and chemical properties of actual materials with first principles.

The development of density functional theory led to the study of electronic structure and is regarded as a major breakthrough in computational condensed matter physics. In many fields such as nuclear physics, molecular physics, chemistry and so on have been paid attention to and widely used. In fact, density functional theory has not only widely influenced many disciplines, but also received feedback from various research fields. During the long period of development of density functional theory, due to its dependence on the mean field approximation in specific applications, the physics community has not paid enough attention to density functional theory. With the establishment of exchange-correlation (xc) energy parameterization [66] under local-density approximation (LDA) and the development of gradient-corrected approximation (GGA)

[67], density functional theory was widely used to describe the many-body systems.

It is still a grand challenge to understand the many-body effects in materials, by all means, since the early days of the quantum mechanics. In fact, the general electronic Hamiltonian which describes all possible systems, is shown in the non-relativistic limit and the Born-Oppenheimer approximation [68] as

$$H = \sum_{i}^{N} \left(-\frac{1}{2}\nabla^2 + v(\mathbf{r}_i) \right) + \sum_{i<j} U(\mathbf{r}_i, \mathbf{r}_j) \tag{3.1}$$

where N is the number of electrons, $v(\mathbf{r}_i)$ is the potential for a single electron and $U(\mathbf{r}_i, \mathbf{r}_j)$ is the electron-electron interaction. For a Coulomb system (the only type of system we consider in this thesis) one has

$$\hat{U} = \sum_{i<j} U(\mathbf{r}_i, \mathbf{r}_j) = \sum_{i<j} \frac{1}{|\mathbf{r}_i - \mathbf{r}_j|}. \tag{3.2}$$

Note that it is universal over any system of particles interacting with the Coulomb interaction, just as the kinetic energy operator

$$\hat{T} = -\frac{1}{2} \sum_{i} \nabla_i^2. \tag{3.3}$$

For a molecule or a solid one has

$$\hat{V} = \sum_{i} v(\mathbf{r}_i) = \sum_{ik} \frac{Z_k}{|\mathbf{r}_i - \mathbf{R}_k|}, \tag{3.4}$$

where the sum on k extends over all nuclei in the system, each with atomic number Z_k and position $\mathbf{R}_k$.

There are many powerful methods developed for solving Schrodinger's equation, such as diagrammatic perturbation theory (based on Feynman diagrams and Green's functions) [69–71] in physics and configuration interaction (CI) methods [72] in chemistry. The high demand for the computational resources makes these approaches simply impossible to be applied to large and complex systems.

Many studies are dedicated to how to improve the efficiency but still study the systems in a very fundamental way. Fortunately, DFT provides a viable alternative, less accurate

perhaps, but much more versatile. Although DFT is formally exact, it makes complex systems tractable at the expense of a little accuracy where its performance depends on the quality of the approximate density functionals used.

The big picture for DFT is that it no longer takes electrons as individuals, but consider it as a whole and then the main concern becomes electron density. DFT shifts the perspective from the electronic wave function, which depends on N three dimensional coordinates, $\Psi(\mathbf{r}_1, \dots, \mathbf{r}_N)$, to the electron density $n(\mathbf{r})$

$$n(\mathbf{r}) = N \int d^3r_2 \int d^3r_3 \cdots \int d^3r_N \Psi^*(\mathbf{r}, \mathbf{r}_2, \dots, \mathbf{r}_N)\Psi(\mathbf{r}, \mathbf{r}_2, \dots, \mathbf{r}_N), \tag{3.5}$$

a function of a single coordinate, which provides a way to systematically map the many-body problem, with $\hat{U}$, onto a single-body problem, without $\hat{U}$.

3.1 The Hohenberg-Kohn theorem

The Hohenberg-Kohn (HK) theorem [64] lies at the heart of DFT. Among the series of theorems Hohenberg and Kohn proposed, there are three statements that are of the most importance.

1. The ground-state (GS) wave function is a unique functional of the GS density

$$\Psi_0 = \Psi[n_0] \tag{3.6}$$

and thus observables are also unique functionals of the GS density

$$O_0 = O[n_0] = \langle \Psi[n_0] | \hat{O} | \Psi[n_0] \rangle . \tag{3.7}$$

2. The GS energy has the following properties, which states that energy evaluated from density that is not ground state energy will be never below the true ground state energy.

$$E_{v,0} = E_v[n_0] = \langle \Psi[n_0] | \hat{H} | \Psi[n_0] \rangle \leq E_v[n'] \tag{3.8}$$

where $\hat{H} = \hat{T} + \hat{U} + \hat{V}$. This follows from the Rayleigh-Ritz variational principle [73]. Much like the variational principle used in quantum mechanics, we can adopt a similar approach in the realm of DFT to calculate the energy of a system with an approximate

density. In this method, a single parameter is introduced as a flexible variable, and the energy is initially computed. Subsequently, this parameter is adjusted to minimize the energy until it converges to the ground state (GS) energy. This parameter could be the lattice constant or the angle between two atoms, for instance. DFT predominantly provides information about ground states, and while this might seem limiting, it's worth noting that in many solid-state systems, excitations can be effectively described as a collection of quasi-particles. Therefore, it becomes possible to investigate the properties of these quasi-particles within the ground state. For those solid-state materials where excitations cannot be adequately represented as quasi-particles, alternative theories, such as time-dependent density functional theory (time-dependent density functional theory (TDDFT)) [74], have been developed to address the properties of excited states.

3. GS density does determine not only the GS wave function Ψ_0, but also the potential $v(\mathbf{r})$ [75–77]

$$v(\mathbf{r}) = v[n_0](\mathbf{r}). \tag{3.9}$$

As a consequence, n_0 now is able to determine the complete Hamiltonian, with the operator $\hat{T}$ and $\hat{U}$ fixed and the operator $\hat{V}$ as

$$V[n] = \int d^3r n(\mathbf{r}) v(\mathbf{r}), \tag{3.10}$$

and thus all excited states too:

$$\Psi_k(\mathbf{r}_1, \mathbf{r}_2, \dots, \mathbf{r}_N) = \Psi_k[n_0], \tag{3.11}$$

where k labels the entire spectrum of the many-body Hamiltonian $\hat{H}$. When considering the GS energy as a functional of the external potential, this can be viewed as a Legendre transform [78].

3.2 The Kohn-Sham equations

The minimization of $E_v[n]$ is, in general, a tough numerical problem on its own. To begin with, reliable approximations for $T[n]$ and $U[n]$ are required. In the Thomas-Fermi

approximation [79, 80], the full interaction energy is approximated by the Hartree energy

$$U[n] \approx U_H[n] = \frac{1}{2}\int d^3r \int d^3r' \frac{n(\mathbf{r})n(\mathbf{r}')}{|\mathbf{r}-\mathbf{r}'|} \tag{3.12}$$

and the kinetic energy is approximated by that of a system of non-interacting electrons

$$T[n] \approx T_s[n] = -\frac{1}{2}\sum_i^N \int d^3r \phi_i^*(\mathbf{r})\nabla^2\phi_i(\mathbf{r}). \tag{3.13}$$

Then the GS energy can be split into

$$E_v[n] = T_s[\{\phi[n]\}] + \int d^3r n(\mathbf{r}) v^{ext}(\mathbf{r}) + \frac{1}{2}\int d^3r \int d^3r' \frac{n(\mathbf{r})n(\mathbf{r}')}{|\mathbf{r}-\mathbf{r}'|} + E_{xc}[n] \tag{3.14}$$

where $v^{ext}(\mathbf{r})$ is the external potential of the system, and the last term defines the xc energy E_{xc}, for which one can give no simple expression.

However, if $n(\mathbf{r})$ varies slowly sufficiently, one can assume that

$$E_{xc}[n] = \int d^3r n(\mathbf{r})\epsilon_{xc}[n] \tag{3.15}$$

where $\epsilon_{xc}[n]$ is the xc energy per electron of a uniform electron gas of density $n(\mathbf{r})$.

From the stationary property of Eq.3.14, we can perform the minimization

$$\begin{aligned} 0 = \frac{\delta E_v[n]}{\delta n(\mathbf{r})} &= \frac{\delta T_s[n]}{\delta n(\mathbf{r})} + \frac{\delta V[n]}{\delta n(\mathbf{r})} + \frac{\delta U_H[n]}{\delta n(\mathbf{r})} + \frac{\delta E_{xc}[n]}{\delta n(\mathbf{r})} \\ &= \frac{\delta T_s[n]}{\delta n(\mathbf{r})} + \varphi(\mathbf{r}) + \mu_{xc}[n(\mathbf{r})] \end{aligned} \tag{3.16}$$

where

$$\varphi(\mathbf{r}) = v^{ext}(\mathbf{r}) + \int d^3r' \frac{n(\mathbf{r}')}{|\mathbf{r}-\mathbf{r}'|} \tag{3.17}$$

and

$$\mu_{xc}[n(\mathbf{r})] = \frac{d(n(\mathbf{r})\epsilon_{xc}[n(\mathbf{r})])}{dn(\mathbf{r})} \tag{3.18}$$

is the exchange and correlation contribute to the chemical potential of a uniform electron gas of density $n(\mathbf{r})$.

Based on the derivation above, Kohn and Sham [65] proposed an auxiliary reference

system of non-interacting electron gas, which has the same GS energy as the interacting system. One can define the Kohn-Sham (KS) potential as

$$v^{KS}(\mathbf{r}) = \varphi(\mathbf{r}) + \mu_{xc}[n(\mathbf{r})]. \tag{3.19}$$

Then the many-body Schrodinger equation becomes separable and the density $n(\mathbf{r})$ can be obtained by simply solving the one-particle Schrodinger equation, which is called as the KS equation,

$$\left[-\frac{1}{2}\nabla^2 + v^{KS}(\mathbf{r})\right]\psi_i(\mathbf{r}) = \epsilon_i\psi_i(\mathbf{r}) \tag{3.20}$$

where $\psi_i(\mathbf{r})$ is the GS eigenstates of the one-particle reference system of electron i, and setting

$$n(\mathbf{r}) = \sum_{i=1}^{N} |\psi_i(\mathbf{r})|^2. \tag{3.21}$$

The scheme can be solved self-consistently. Begin with an assumed $n(\mathbf{r})$, $\varphi(\mathbf{r})$ and $\mu_{xc}[n(\mathbf{r})]$ are obtained by Eq.3.17 and Eq.3.18. Then the new $n(\mathbf{r})$ can be found from Eq.3.20 and Eq.3.21. The energy is given by

$$E = \sum_{i=1}^{N}\epsilon_i - \frac{1}{2}\int d^3r \int d^3r' \frac{n(\mathbf{r})n(\mathbf{r}')}{|\mathbf{r}-\mathbf{r}'|} + \int d^3r n(\mathbf{r})\left(\epsilon_{xc}[n(\mathbf{r})] - \mu_{xc}[n(\mathbf{r})]\right). \tag{3.22}$$

3.3 Exchange-correlation potentials and gradient-corrected approximation (GGA)

The difference in kinetic and interacting energy between the true and fictitious system, i.e. $T - T_s$ and $U - U_H$, has been cast into the xc energy.

The deviation of the xc function in relation to the total number of particles is among the most interesting characteristics of an exact functional, which has opposed all attempts at describing it within local or semilocal approximations, shown as [81–83]

$$\left.\frac{\delta E_{xc}[n]}{\delta n(\mathbf{r})}\right|_{N+\delta} - \left.\frac{\delta E_{xc}[n]}{\delta n(\mathbf{r})}\right|_{N-\delta} = \epsilon_{xc}^{+}(\mathbf{r}) - \epsilon_{xc}^{-}(\mathbf{r}) = \Delta_{xc}. \tag{3.23}$$

where δ is an infinitesimal shift of the electron number N, and Δ_{xc} is a system-dependent,

but $\mathbf{r}$-independent shift of the xc potential $v_{xc}(\mathbf{r})$ as it passes from the electorn-poor to the electron-rich side of integer N. The noninteracting kinetic energy functional has a similar discontinuity, given by

$$\left.\frac{\delta T_s[n]}{\delta n(\mathbf{r})}\right|_{N+\delta} - \left.\frac{\delta T_s[n]}{\delta n(\mathbf{r})}\right|_{N-\delta} = \epsilon_{N+1} - \epsilon_N = \Delta_{KS} \tag{3.24}$$

where ϵ_N and ϵ_{N+1} are the KS one-particle energies of the highest occupied and lowest unoccupied eigenstate. The true fundamental gap is the discontinuity of the total ground-state energy functional [81–84],

$$\Delta = \left.\frac{\delta E[n]}{\delta n(\mathbf{r})}\right|_{N+\delta} - \left.\frac{\delta E[n]}{\delta n(\mathbf{r})}\right|_{N-\delta} = \Delta_{KS} + \Delta_{xc}. \tag{3.25}$$

Standard density functionals predict $\Delta_{xc} = 0$, and thus often underestimate the fundamental gap. The most common approximations are LDA and GGA [67]. LDA divides the whole inhomogeneous system into a lot of small pieces, and in the region of each piece, subsystem is regarded as homogeneous. However, any real system is spatially inhomogeneous, i.e., it has a spatially varying density $n(\mathbf{r})$, and thus it would be useful to include information on the rate of this variation in the functional

$$E_{xc}^{GGA}[n] = \int d^3r f(n(\mathbf{r}), \nabla n(\mathbf{r})), \tag{3.26}$$

which have become known as GGA [67].

Different GGA differs in the construction of $f(n(\mathbf{r}), \nabla n(\mathbf{r}))$. The most common GGA is PBE functional [85], and is applied to both molecule and solids, including metals. It is a non-empirical functional, though not the most accurate GGA [86, 87], that is able to hold reasonable accuracy and can be generalized for a wide range of systems.

3.4 Implementations of DFT – Basis sets

There are basically three distinct types of approximations involved in DFT calculation. One is the utilization of a fictitious reference system with the sum of single particle to represent the true many-body system. The second approximation refers to constructing

the expression for the unknown xc functional. The third one consists of the numerical approximations involved in solving the differential equation, whose main aspect is the selection of a suitable basis set.

In practice, the numerical solution of the KS differential equation Eq.3.20 is typically obtained by expanding the KS orbitals to a suitable set of basis functions and solving for the coefficients in this expansion and its eigenvalues from the resulting secular equation. In the electronic structure theory, one of the main tasks is to construct such a set of basis functions, which is of relevance to a wide range of other areas beyond DFT.

Plane-wave basis sets are popular in calculations involving periodic solids. The choice of a plane wave basis set is normally determined by the cutoff energy. The calculation then includes the plane waves in the simulation cell that are below the energy criterion. In practical applications, plane-wave basis sets are frequently employed in conjunction with an 'effective core potential' or pseudopotential. This approach allows the plane waves to specifically describe the valence charge density, focusing on the electrons that primarily participate in chemical interactions. The rationale behind this choice lies in the fact that core electrons are typically tightly localized in the vicinity of atomic nuclei. Consequently, they generate substantial wavefunction and charge density gradients near the nuclei. These gradients pose a challenge for accurate representation using a plane-wave basis set, unless an extremely high energy cutoff is used, resulting in exceptionally small wavelengths that can become computationally burdensome.

Although any basis set that sufficiently spans the space of electron distribution could be used, the concept of Molecular Orbitals as Linear Combinations of Atomic Orbitals (LCAO) [88] suggests a very natural set of basis functions: AO-type functions centered on each nuclei. One common used choice are Gaussian-type orbital (GTO) [89] for basis functions. A Gaussian basis function has the form

$$G_{nlm}(r,\theta,\phi) = N_n \underbrace{r^{n-1}e^{-\alpha r^2}}_{\text{radial part}} \underbrace{Y_l^m(\theta,\phi)}_{\text{angular part}} . \tag{3.27}$$

Note that in all the basis sets, only the radial part of the orbital changes, and the spherical harmonic functions are used in all of them to describe the angular part of the orbital.

The primary motivation for utilizing Gaussian basis functions in molecular quantum chemical calculations is the Gaussian Product Theorem [90–92]. This theorem assures

that when two Gaussian-type orbitals (GTOs) centered on distinct atoms are multiplied, the result is a finite summation of Gaussians centered along the axis connecting those atoms. This property facilitates the reduction of four-center integrals to finite combinations of two-center integrals and, subsequently, to finite sums of one-center integrals. Handling GTOs is numerically more tractable because the product of two GTOs from different atoms yields another GTO positioned in between.

Conversely, the primary advantage of employing a plane-wave basis set lies in its guaranteed smooth and monotonous convergence towards the target wavefunction. In contrast, when localized basis sets are employed, achieving monotonous convergence to the basis set limit can be challenging due to issues related to over-completeness. In larger basis sets, functions associated with different atoms tend to exhibit similarities, and numerous eigenvalues of the overlap matrix tend to approach zero. Additionally, certain integrals and operations are more straightforward to program and execute with plane-wave basis functions compared to their localized counterparts. When this property is coupled with separable pseudopotentials of the Kleinman-Bylander type [93] and preconditioned conjugate gradient solution techniques, it becomes possible to dynamically simulate periodic systems containing hundreds of atoms. Furthermore, as all functions within the plane-wave basis are mutually orthogonal and not tied to specific atoms, plane-wave basis sets do not exhibit basis-set superposition errors. However, it's important to note that the size of the simulation cell has an influence on the plane-wave basis set, which can complicate the optimization of cell size.

3.5 The merits and shortcomings of DFT

DFT has been widely spread in the condensed matter community since it provides surprisingly good results for a wide range of materials with regard to the experiments. Furthermore, its computational cost remains relatively low and make the manipulation of complex systems tractable with growing computer power. Even though there are intrinsic approximations, DFT is usually able to provide a good starting point for the further study, such as diagrammatic perturbation methods and quantum embedding methods.

The difficulty of identifying the most suitable method for a particular application is one of the main disadvantages. The user should refer to the literature to identify which

setup is suitable for the particular problem or application. Another disadvantage of density field theory is the fact that it does not appropriately take into account exchange interactions. While the existence of a functional that can correct exchanges has been demonstrated, this function is not known and approximations to it are based on semi-parametric methods. Despite notable advancements in recent years, challenges persist in applying DFT to accurately depict various intermolecular interactions, which are crucial for comprehending chemical reactions. These challenges are particularly pronounced in the context of Van der Waals forces (dispersion); charge transfer excitations; transition states, global potential energy surfaces, dopant interactions and some strongly correlated systems; and in calculations of the band gap and ferromagnetism in semiconductors. These intricacies underscore the ongoing need for advancements in DFT methodologies to effectively tackle these complex aspects of molecular and materials science.

Chapter 4

Many-Body Perturbation Theory

One powerful tool that has revolutionized our understanding of many-body systems is Many-Body Perturbation Theory (MBPT) [94]. This theory has unveiled a comprehensive framework for comprehending various phenomena in condensed matter physics, nuclear physics, and quantum chemistry. Central to this theory is the idea that the complex interactions between multiple particles can be approximated by summing progressively more terms in a series. The approximations based on this theory, such as the HF approximation [63], GF2 [95], and the GW approximation [96], have all proven to be useful for addressing the complexities associated with many-body systems.

The HF approximation [63] treats each particle as moving independently under the effect of an averaged field created by other particles. Even though this approximation cannot capture correlation effects between particles, it offers reasonably good predictions about the behavior of complex systems.

On the other hand, the GF2 [45–48] is more sophisticated, involving the creation of a self-consistent field that accounts for both the quantum fluctuations and the correlations between the particles, leading to a refined estimate of ground-state energy and excitations.

The GW approximation [96] is a formalism that goes beyond the HF approximation by incorporating the screened Coulomb interaction and is largely used in the field of quantum chemistry and solid-state physics to calculate the properties of electrons in solids. By having these approximations and methodologies at our disposal, it is possible to build a more complete picture of the behavior of many-body systems, sequentially unveiling the mysteries of quantum world.

4.1 Electronic Hamiltonian and atomic Gaussain-type orbital

In the second quantization formalism, the Hamiltonian in Eq.3.1 can be expressed as

$$\hat{H} = \sum_{ij}\sum_{\sigma}(H_0)_{ij}\hat{c}^{\dagger}_{i\sigma}\hat{c}_{j\sigma} + \sum_{ijkl}\sum_{\sigma\sigma'}U_{ijkl}\hat{c}^{\dagger}_{i\sigma}\hat{c}^{\dagger}_{k\sigma'}\hat{c}_{l\sigma'}\hat{c}_{j\sigma} \tag{4.1}$$

where $\hat{c}^{\dagger}_{i\sigma}$ ($\hat{c}_{i\sigma}$) is the creation (annihilation) electronic operators in a single-particle basis $\phi_i(\mathbf{r})$ with spin σ, and $(H_0)_{ij}$ (U_{ijkl}) are the matrix elements of the one-electron (two-electron) part of the Hamiltonian.

Atomic GTO [13–16] $\phi_i(\mathbf{r})$ are specifically designed as a finite basis set of linear superposition of Gaussian functions to model the behavior of electrons in isolated atoms. They are characterized by their center, exponent, and normalization factor. The center represents the position of the atom, the exponent determines the spread of the orbital, and the normalization factor ensures that the orbital is properly normalized (i.e., its integral squared over all space is equal to one). Atomic GTOs provide a flexible and efficient representation of electron density and wavefunctions in atoms, enabling accurate calculations of atomic properties.

However, the adoption of GTOs is accompanied by several notable drawbacks. Firstly, GTOs lack correct asymptotic behavior, as they decay with an e^{-r^2} behavior rather than the expected exponential e^{-r} decay of true atomic orbitals. This discrepancy can introduce inaccuracies, notably in the calculation of ionization potentials and electron affinities. Additionally, addressing the incorrect asymptotic behavior necessitates employing multiple GTOs to approximate a single atomic orbital, thereby increasing computational costs. Furthermore, GTO-based results are sensitive to the choice of basis set, which adds complexity and system-dependent variability to the calculations. Core orbitals pose another challenge, as GTOs struggle to accurately represent their tightly bound, peaked-at-the-nucleus nature. Lastly, GTOs have limitations in capturing electron correlation effects, requiring more advanced methods in some cases. Despite these limitations, GTOs are favored for their mathematical simplicity and computational efficiency, particularly in moderately sized systems where a balance between accuracy and cost is sought.

The matrix element in Eq.4.1 can be expressed as

$$(H_0)_{ij} = \int d\mathbf{r}\phi_i^*(\mathbf{r})\hat{H}_0\phi_j(\mathbf{r}) \tag{4.2}$$

and

$$U_{ijkl} = \int d\mathbf{r} \int d\mathbf{r}'\phi_i^*(\mathbf{r})\phi_j(\mathbf{r})\frac{1}{|\mathbf{r}\mathbf{r}'|}\phi_k^*(\mathbf{r}')\phi_l(\mathbf{r}') \tag{4.3}$$

Atomic GTOs are non-orthogonal, so the anti-communication relation of the electronic operators is given by

$$\left\{\hat{c}_{i\sigma}^\dagger, \hat{c}_{j\sigma'}\right\} = S_{ij}\delta_{\sigma\sigma'} \tag{4.4}$$

where $\mathbf{S}$ is the overlap matrix

$$S_{ij} = \int d\mathbf{r}\phi_i^*(\mathbf{r})\phi_j(\mathbf{r}) \tag{4.5}$$

4.1.1 Bloch Gaussian-type orbital

Bloch GTOs [13–16] are used to describe the electronic structure of solids. Solids have a periodic crystal structure, and the Bloch's theorem plays a fundamental role in describing the behavior of electrons in such systems. It states that the wavefunctions of electrons in a crystalline solid can be expressed as a product of a plane wave and a periodic function [97]. The periodic part is represented by Bloch functions, and can be expanded as a sum of periodic GTOs. These Bloch GTOs capture the localized behavior of electrons within individual unit cells of the crystal lattice, while the plane wave component represents the delocalized nature of electrons in the solid.

Bloch GTOs can be regarded as transitional-symmetry-adapted linear combination of Gaussian atomic orbitals (AOs) of the form [13]

$$\phi_i^{\mathbf{k}}(\mathbf{r}) = \sum_{\mathbf{T}} e^{i\mathbf{k}\cdot\mathbf{T}}\tilde{\phi}_i(\mathbf{r}-\mathbf{T}) \equiv e^{i\mathbf{k}\cdot\mathbf{r}}u_i^{\mathbf{k}}(\mathbf{r}) \tag{4.6}$$

where $\mathbf{T}$ is the lattice translation vector and $\mathbf{k}$ is crystal momentum vector in the first Brillouin zone (BZ). The latter equivalence in Eq.4.6 comes from the Bloch's theorem, where $u_i^{\mathbf{k}}(\mathbf{r})$ is a Bloch function that is fully periodic with regard to all lattice translations.

We can expand the Bloch GTOs in a set of auxiliary plane waves:

$$\phi_i^{\mathbf{k}}(\mathbf{r}) = \sum_{\mathbf{G}} \phi_i^k(\mathbf{G}) e^{i(\mathbf{k}+\mathbf{G})\cdot\mathbf{r}} = \sum_{\mathbf{R}} \phi_i^{\mathbf{R}}(\mathbf{r}) e^{i\mathbf{k}\cdot\mathbf{R}} \tag{4.7}$$

$$\phi_i^{\mathbf{k}}(\mathbf{G}) = \frac{1}{\Omega} \int_{\Omega} d\mathbf{r} \phi_i^{\mathbf{k}}(\mathbf{r}) e^{-i(\mathbf{k}+\mathbf{G})\cdot\mathbf{r}} \tag{4.8}$$

where Ω represents the unit cell volume, $\mathbf{G}$ represents a reciprocal lattice vector, $\mathbf{R}$ represents unit cell index and $\phi_i^{\mathbf{R}}(\mathbf{r})$ are atomic-centered Gaussian functions shifted to the unit cell with label $\mathbf{R}$, i.e. $\phi_i^{\mathbf{R}}(\mathbf{r}) = \varphi_i(\mathbf{r} - \mathbf{R})$ in which $\varphi_i(\mathbf{r})$ are these functions in the central unit cell.

For two Bloch basis functions, the overlap matrix is defined

$$S_{ij} = \int d\mathbf{r} \phi_i^{\mathbf{k}*}(\mathbf{r}) \phi_j^{\mathbf{k}'}(\mathbf{r}) = N\delta_{\mathbf{k}\mathbf{k}'} \sum_{\mathbf{R}} e^{i\mathbf{k}'\cdot\mathbf{R}} \int d\mathbf{r} \phi_i^0(\mathbf{r}) \phi_i^{\mathbf{R}}(\mathbf{r}) \tag{4.9}$$

The Gaussian-type Bloch waves are orthogonal for different crystal momenta.

Then the corresponding Hamiltonian in Bloch GTOs can be expressed as

$$\begin{aligned} \hat{H} = & \sum_{\mathbf{k}} \sum_{ij} \sum_{\sigma\sigma'} (H_0)^{\mathbf{k}}_{i\sigma,j\sigma'} \hat{c}^{\mathbf{k}\dagger}_{i\sigma} \hat{c}^{\mathbf{k}}_{j\sigma'} \\ & + \frac{1}{2N_k} \sum_{ijkl} \sum_{\mathbf{k}\mathbf{k}'\mathbf{q}} \sum_{\sigma\sigma'} U^{\mathbf{k},\mathbf{k}-\mathbf{q},\mathbf{k}',\mathbf{k}'+\mathbf{q}}_{ijkl} \hat{c}^{\mathbf{k}\dagger}_{i\sigma} \hat{c}^{\mathbf{k}\dagger}_{i\sigma} \hat{c}^{\mathbf{k}'\dagger}_{k\sigma'} \hat{c}^{\mathbf{k}'+\mathbf{q}}_{j\sigma'} \hat{c}^{\mathbf{k}-\mathbf{q}}_{j\sigma'} \end{aligned} \tag{4.10}$$

where $\hat{c}^{\mathbf{k}\dagger}_{i\sigma}$ ($\hat{c}^{\mathbf{k}}_{i\sigma}$) are the creation (annihilation) electronic operators for the single-particle spin-orbital basis with crystal momentum k, spin σ and basis function index i.

4.2 Hartree-Fock theory

The HF approximation [63] is a mean-field approach used in electronic structure calculations to describe the behavior of electrons in many-body systems. It plays a central role in understanding the electronic structures of molecules, atoms, and solids. The HF approximation assumes that each electron moves in an average potential generated by all other electrons in the system, neglecting the dynamic correlation effects, and that the wavefunction of each electron is independent of the wavefunctions of the other electrons. This simplification leads to some limitations in the accuracy of the approximation, but

still provides a practical starting point and valuable insights into the properties of materials. It serves as a stepping stone to more accurate but computationally intensive methods that consider electron-electron correlation effects [73].

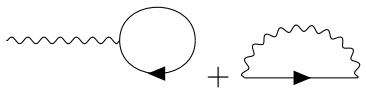

Figure 4.1: Feynman diagrams for the self-energy in the Hartree-Fock approximation.

The HF theory is the first order approximation to the self-energy, which is shown using Feynman diagrams [98] in Fig. The HF self-energy is static and can be further divided into a Hartree term ($\mathbf{J}$) and an exchange term ($\mathbf{K}$)

$$(\Sigma_{HF})^{\mathbf{k}}_{i\sigma,j\sigma'} = J^{\mathbf{k}}_{i\sigma,j\sigma'} + K^{\mathbf{k}}_{i\sigma,j\sigma'} \tag{4.11}$$

where in the Bloch GTOs,

$$\begin{aligned} J^{\mathbf{k}}_{i\sigma,j\sigma'} &= \frac{1}{N_k\beta}\sum_{\mathbf{k}'n}\sum_{ab\sigma'} G^{\mathbf{k}'}_{b\sigma',a\sigma'}(i\omega_n)U^{\mathbf{kkk}'\mathbf{k}'}_{ijab} = \frac{1}{N_k}\sum_{\mathbf{k}'}\sum_{ab\sigma'} G^{\mathbf{k}'}_{b\sigma',a\sigma'}(\tau=0^-)U^{\mathbf{kkk}'\mathbf{k}'}_{ijab} \\ &= \frac{1}{N_k}\sum_{\mathbf{k}'}\sum_{ab\sigma'} \gamma^{\mathbf{k}'}_{b\sigma',a\sigma'}U^{\mathbf{kkk}'\mathbf{k}'}_{ijab}, \end{aligned} \tag{4.12}$$

$$\begin{aligned} K^{\mathbf{k}}_{i\sigma,j\sigma'} &= -\frac{1}{N_k\beta}\sum_{\mathbf{k}'n}\sum_{ab\sigma} G^{\mathbf{k}'}_{a\sigma,b\sigma}(i\omega_n)U^{\mathbf{kk}'\mathbf{k}'\mathbf{k}}_{iabj} = -\frac{1}{N_k}\sum_{\mathbf{k}'}\sum_{ab\sigma} G^{\mathbf{k}'}_{a\sigma,b\sigma}(\tau=0^-)U^{\mathbf{kk}'\mathbf{k}'\mathbf{k}}_{iabj} \\ &= -\frac{1}{N_k}\sum_{\mathbf{k}'}\sum_{ab\sigma} \gamma^{\mathbf{k}'}_{a\sigma,b\sigma}U^{\mathbf{kk}'\mathbf{k}'\mathbf{k}}_{iabj} \end{aligned} \tag{4.13}$$

N_k is the number of $\mathbf{k}$ grids and $\gamma^{\mathbf{k}}$ is the density matrix.

In the HF method, the Fock matrix $\mathbf{F}$ is used to include the static part of the single-electron energy operator of a given quantum system, which, in our case, is,

$$\mathbf{F} = \mathbf{H}_0 + \mathbf{J} + \mathbf{K} \tag{4.14}$$

Since the dynamic correlations are neglected by the HF approximation, the frequency-

dependent HF Green's function is

$$G^{\mathbf{k}}_{\mathrm{HF}}(i\omega_n) = \left[(i\omega_n + \mu)\mathbf{S}^{\mathbf{k}} - \mathbf{F}^{\mathbf{k}}\right]^{-1} \tag{4.15}$$

The HF equations are a set of integro-differential equations and cannot be solved analytically for systems larger than a single electron. Therefore, they must be solved iteratively. The iterative process typically begins with an initial guess for the molecular orbitals. These are plugged into the Fock operator to compute an initial Fock matrix. The Fock matrix is then diagonalized to give a new set of molecular orbitals. These new orbitals are then used to construct a new Fock matrix, and the process is repeated. This is known as a self-consistent field (SCF) procedure. The goal is to find a set of orbitals that are unchanged by this process; in other words, they are self-consistent. The iterative process is repeated until the energy converges to a predetermined level of accuracy. This means that the difference in total energy between successive iterations is less than a certain threshold.

While the Hartree-Fock method gives a reasonable approximation for many systems, it does not include electron correlation effects. Therefore, it is often used as a starting point for more accurate methods that do include these effects.

4.3 Self-consistent second-order Green's function method

The self-consistent second-order Green's function method, also known as GF2, aims to go beyond the limitations of the HF theory by incorporating electron-electron interactions up to second order.

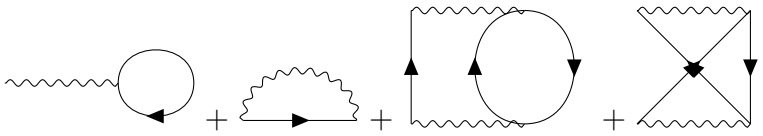

Figure 4.2: Feynman diagrams for the second order self-energy within GF2. The first two diagrams are frequency-independent, and are included in the Fock matrix. The next two diagrams are frequency-dependent, and represent the second-order correlation effects covered by $\Sigma(\omega)$.

Based on the Hamiltonian expressed in a Bloch basis in reciprocal space shown in Eq.4.10, the second-order self-energy is evaluated in an imaginary time formalism,

$$\Sigma_{ij}^{\mathbf{k},(2)}(\tau) = -\frac{1}{N_k^2} \sum_{\mathbf{k}_1\mathbf{k}_2\mathbf{k}_3} \sum_{klmnpq} G_{kl}^{\mathbf{k}_1}(\tau) G_{mn}^{\mathbf{k}_2}(\tau) G_{pq}^{\mathbf{k}_3}(\tau) U_{imqk}^{\mathbf{k}\mathbf{k}_2\mathbf{k}_3\mathbf{k}_1} \times (2U_{lpnj}^{\mathbf{k}_1\mathbf{k}_3\mathbf{k}_2\mathbf{k}} - U_{nplj}^{\mathbf{k}_2\mathbf{k}_3\mathbf{k}_1\mathbf{k}}) \delta_{\mathbf{k}+\mathbf{k}_2,\mathbf{k}_1+\mathbf{k}_3} \tag{4.16}$$

With the self-energy constructed, we can fast Fourier transform $\Sigma(\tau)$ to the frequency domain and build the Green's function as

$$G(i\omega_n) = [(i\omega_n + \mu)\mathbf{S} - \mathbf{F} - \Sigma(\omega)]^{-1} \tag{4.17}$$

In the bare second-order perturbation theory, known as Møller-Plesset second order (MP2) [99–102], the HF Green's function is employed in Eq.4.16 and the Dyson equation is evaluated only once to yield the interacting Green's function. MP2 widely fails to predict gaps for materials with band gaps smaller than 6 eV [103].

In renormalized perturbation theories such as GF2, in order to obtain the full self-consistency in both the static quantities (such as the density matrix, the Fock matrix as well as the frequency-independent part of the self-energy Σ_∞) and the dynamical self-energy $\Sigma(\omega)$, we employ the following iterative procedures [45]: start from a restricted HF calculation; adjust the chemical potential to obtain the electron number of HF solution, then rebuild the Fock matrix and the HF Green's functions using the Dyson equation, repeat this step until we got a consistent static solution; construct the dynamical self-energy and then the interacting Green's function for the next second-order self-energy evaluation, until convergence is achieved in all quantities.

4.4 Self-consistent finite temperature GW approximation

The GW approximation [96] is the simplest working approximation beyond the HF approximation that takes screening into account. This screening arises from the correlations between electrons, which prevent them from occupying the same single-particle state due to the large Coulomb energy associated with it. As a result, a screening

hole is created around each electron, reducing their interaction with other electrons and lowering the Coulomb energy. By including screening effects, the GW approximation can be regarded as a generalization of the HF approximation but with a dynamically screened Coulomb interaction by replacing the bare Coulomb interaction U by a screened interaction W [104]:

$$\Sigma^{GW}(\mathbf{r}, \mathbf{r}'; \omega) = \frac{i}{2\pi} \int d\omega' G(\mathbf{r}, \mathbf{r}'; \omega + \omega') W(\mathbf{r}, \mathbf{r}'; \omega') \tag{4.18}$$

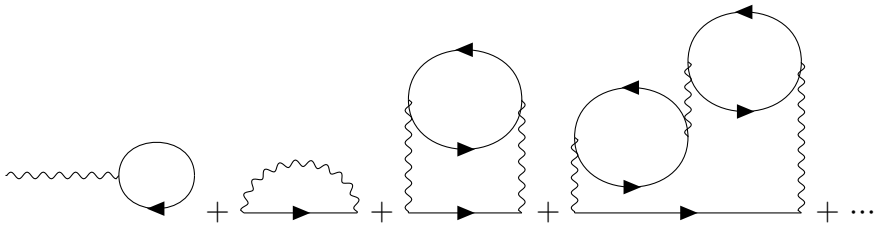

Figure 4.3: Feynman diagrams for the self-energy in the GW approximation.

Separating the self-energy into its static and dynamical part and considering on the Matsubara axis, which is easy to tackle during the self-consistent process without resorting to analytical continuation,

$$(\Sigma_{GW})^{\mathbf{k}}[\mathbf{G}](i\omega_n) = (\Sigma_{GW,\infty})^{\mathbf{k}}[\mathbf{G}] + (\tilde{\Sigma}_{GW})^{\mathbf{k}}[\mathbf{G}](i\omega_n) \tag{4.19}$$

where $(\Sigma_{GW,\infty})^{\mathbf{k}}$ is the static HF self-energy, i.e. $(\Sigma_{HF})^{\mathbf{k}}$ and $(\tilde{\Sigma}_{GW})^{\mathbf{k}}(i\omega_n)$ is associated with the GW self-energy that depends on frequency, derived through summing an unlimited series of diagrams similar to those in the Random Phase Approximation (RPA), often referred to as 'bubble' diagrams. And $\omega_n = (2n+1)\pi/\beta, n \in \mathcal{Z}$ are fermionic Matsubara frequencies, where β is the inverse temperature.

On the imaginary-time axis $\tau \in [0, \beta]$, $(\tilde{\Sigma}_{GW})^{\mathbf{k}}$ reads

$$(\tilde{\Sigma}_{GW})^{\mathbf{k}}_{i\sigma,j\sigma}(\tau) = -\frac{1}{N_k} \sum_{\mathbf{q}} \sum_{ab} G^{\mathbf{k}-\mathbf{q}}_{a\sigma,b\sigma}(\tau) \tilde{W}^{\mathbf{k},\mathbf{k}-\mathbf{q},\mathbf{k}-\mathbf{q},\mathbf{k}}_{iabj}(\tau) \tag{4.20}$$

where $\tilde{W}$ is the effective screened interaction tensor, defined as the difference between the full dynamically screened interaction W and the bare interaction U, i.e. $\tilde{W} = W - U$.

Fourier transforms between imaginary-time and Matsubata frequency are defined as

$$G^{\mathbf{k}}_{i\sigma,j\sigma}(i\omega_n) = \int_0^\beta d\tau G^{\mathbf{k}}_{i\sigma,j\sigma}(\tau) e^{i\omega_n \tau} \tag{4.21}$$

and

$$G^{\mathbf{k}}_{i\sigma,j\sigma}(\tau) = \frac{1}{\beta} \sum_n G^{\mathbf{k}}_{i\sigma,j\sigma}(i\omega_n) e^{-i\omega_n \tau} \tag{4.22}$$

Given an interacting Green's function $G^{\mathbf{k}}(\tau)$, the correlated density matrix is determined as

$$\gamma^{\mathbf{k}} = -G^{\mathbf{k}}(\tau = \beta^-) \tag{4.23}$$

and thus the total number of electrons N_e can be obtained by

$$N_e = \frac{1}{N_k} \sum_{\mathbf{k}} \mathrm{tr}[\gamma^{\mathbf{k}} S^{\mathbf{k}}] \tag{4.24}$$

where the trace implies a sum over the diagonals in the spin-orbital space.

In the Matsubara frequency domain, the Dyson equation relating self-energies to Green's functions is

$$\begin{aligned} [G^{\mathbf{k}}(i\omega_n)]^{-1} &= (i\omega_n + \mu) S^{\mathbf{k}} - H_0^{\mathbf{k}} - \Sigma^{\mathbf{k}}[G](i\omega_n) \\ &= [G_0^{\mathbf{k}}(i\omega_n)]^{-1} - \Sigma^{\mathbf{k}}[G](i\omega_n) \end{aligned} \tag{4.25}$$

where $G_0^{\mathbf{k}}(i\omega_n)$ is the non-interacting Green's function of the one-electron Hamiltonian $H_0^{\mathbf{k}}$ and $\Sigma^{\mathbf{k}}[G]$ is the self-energy being a functional of the full interacting Green's function $G^{\mathbf{k}}(i\omega_n)$. $(\Sigma_{GW})^{\mathbf{k}}[\mathbf{G}](i\omega_n)$ is the GW approximation of $\Sigma^{\mathbf{k}}[G](i\omega_n)$.

Combining Eq.4.4 with the Dyson equation (Eq.4.4), the self-energy is solved as a functional of the interacting Green's function $G^{\mathbf{k}}(i\omega_n)$ iteratively until self-consistency between $G^{\mathbf{k}}(i\omega_n)$ and $(\Sigma_{GW})^{\mathbf{k}}(i\omega_n)$ is achieved [8].

4.4.1 Decomposition of two-electron Coulomb interaction and the screened interaction

In the GW approximation, the screened interaction W is expressed as [96]

$$W_{ijkl}^{\mathbf{k}_1\mathbf{k}_2\mathbf{k}_3\mathbf{k}_4}(\tau) = U_{ijkl}^{\mathbf{k}_1\mathbf{k}_2\mathbf{k}_3\mathbf{k}_4} + \frac{1}{N_k}\sum_{\mathbf{k}_5\mathbf{k}_6\mathbf{k}_7\mathbf{k}_8}\sum_{abcd} U_{ijab}^{\mathbf{k}_1\mathbf{k}_2\mathbf{k}_5\mathbf{k}_6}\Pi_{abcd}^{\mathbf{k}_5\mathbf{k}_6\mathbf{k}_7\mathbf{k}_8}(\tau)W_{cdkl}^{\mathbf{k}_7\mathbf{k}_8\mathbf{k}_3\mathbf{k}_4}(\tau) \tag{4.26}$$

where Π is the non-interacting polarization function

$$\Pi_{abcd}^{\mathbf{k}_1\mathbf{k}_2\mathbf{k}_3\mathbf{k}_4}(\tau) = \sum_{\sigma} G_{d\sigma,a\sigma}^{\mathbf{k}_1}(\tau)G_{b\sigma,c\sigma}^{\mathbf{k}_2}(-\tau)\delta_{\mathbf{k}_1\mathbf{k}_4}\delta_{\mathbf{k}_2\mathbf{k}_3} \tag{4.27}$$

Given the substantial memory consumption of a two-electron Coulomb interaction tensor U, it's necessary to perform a decomposition on this tensor, which is displayed as follows:

$$U_{ijkl}^{\mathbf{k},\mathbf{k}-\mathbf{q},\mathbf{k}',\mathbf{k}'+\mathbf{q}} = \sum_{Q} V_{ij}^{\mathbf{k}\mathbf{k}-\mathbf{q}}(Q)V_{kl}^{\mathbf{k}'\mathbf{k}'+\mathbf{q}}(Q) \tag{4.28}$$

where Q denotes an auxiliary decomposition index and $V_{ij}^{\mathbf{k}\mathbf{k}-\mathbf{q}}$ is a tensor with two momenta, two orbital indices and an auxiliary index.

The processes of decomposition encompass methods such as the Cholesky decomposition [105] and the density fitting technique, also referred to as the resolution-of-identity (RI) approximation [106–108]. In the work of [8], they utilized periodic Gaussian density fitting (GDF) with the overlap metric [109–111]. With an extra set of auxiliary Gaussian orbitals $\chi_Q^{\mathbf{q}}(\mathbf{r})$ acting as the auxiliary basis, we calculate Equation 6 as follows:

$$V_{ij}^{\mathbf{k}_1\mathbf{k}_2}(Q) = \sum_{PP'}(J^{\mathbf{q}})_{QP'}^{1/2}(A^{\mathbf{q}})_{P'P}^{-1}B_{ij}^{\mathbf{k}_1\mathbf{k}_2}(P) \tag{4.29}$$

where $\mathbf{q} = \mathbf{k}_2 - \mathbf{k}_1$, and

$$A^{\mathbf{q}}_{P'P} = \int_\Omega d\mathbf{r} \chi^{\mathbf{q}*}_P(\mathbf{r}) \chi'^{\mathbf{q}}_P(\mathbf{r}), \tag{4.30}$$

$$B^{\mathbf{k}_1\mathbf{k}_2}_{ij}(P) = \int_\Omega d\mathbf{r} \chi^{\mathbf{q}*}_P(\mathbf{r}) g^{\mathbf{k}_1*}_i(\mathbf{r}_1) g^{\mathbf{k}_2}_j(\mathbf{r}), \tag{4.31}$$

$$J^{\mathbf{q}}_{PQ} = \int\int d\mathbf{r} d\mathbf{r}' \frac{\chi^{\mathbf{q}*}_P(\mathbf{r}) \chi^{\mathbf{q}}_Q(\mathbf{r}')}{|\mathbf{r} - \mathbf{r}'|} \tag{4.32}$$

The above decomposition of Coulomb integrals enables us to repsent the effective screened interaction tensor $\tilde{W}$ as

$$\tilde{W}^{\mathbf{k},\mathbf{k}-\mathbf{q},\mathbf{k}-\mathbf{q},\mathbf{k}}_{ijkl}(i\Omega_n) = \sum_{QQ'} V^{\mathbf{k}\mathbf{k}-\mathbf{q}}_{ij}(Q) \left\{ \tilde{P}^{\mathbf{q}}_{0,QQ'}(i\Omega_n) + [\tilde{P}^{\mathbf{q}}_0(i\Omega_n)]^2_{QQ'} + ... \right\} V^{\mathbf{k}-\mathbf{q},\mathbf{k}}_{kl}(Q') \tag{4.33}$$

$$= \sum_{QQ'} V^{\mathbf{k}\mathbf{k}-\mathbf{q}}_{ij}(Q) \tilde{P}^{\mathbf{q}}_{QQ'}(i\Omega_n) V^{\mathbf{k}-\mathbf{q},\mathbf{k}}_{kl}(Q') \tag{4.34}$$

where $\Omega_n = 2n\pi/\beta$ ($n \in \mathcal{Z}$) are bosonic Matsubara frequencies. The non-interacting auxiliary function $\tilde{P}^{\mathbf{q}}_0(i\Omega_n)$ is defined as

$$\tilde{P}^{\mathbf{q}}_{0,QQ'}(i\Omega_n) = \int_0^\beta d\tau \tilde{P}^{\mathbf{q}}_{0,QQ'}(\tau) e^{i\Omega_n \tau} \tag{4.35}$$

where

$$\tilde{P}^{\mathbf{q}}_{0,QQ'}(\tau) = -\frac{1}{N_k} \sum_{\mathbf{k}} \sum_{\sigma\sigma'} \sum_{abcd} V^{\mathbf{k}\mathbf{k}+\mathbf{q}}_{da}(Q) G^{\mathbf{k}}_{c\sigma',d\sigma}(-\tau) G^{\mathbf{k}+\mathbf{q}}_{a\sigma,b\sigma'}(\tau) V^{\mathbf{k}+\mathbf{q},\mathbf{k}}_{bc}(Q') \tag{4.36}$$

Thus the normalized auxiliary function can be calculated through the geometric series

$$\tilde{P}^{\mathbf{q}}(i\Omega_n) = \sum_{m=1}^{\infty} [\tilde{P}^{\mathbf{q}}_0(i\Omega_n)]^m = [I - \tilde{P}^{\mathbf{q}}_0(i\Omega_n)]^{-1} \tilde{P}^{\mathbf{q}}_0(i\Omega_n) \tag{4.37}$$

Transforming $\tilde{P}^{\mathbf{q}}(i\Omega_n)$ from the Matsubara frequency to the imaginary-time domain

$$\tilde{P}^{\mathbf{q}}_{QQ'}(\tau) = \frac{1}{\beta} \sum_n \tilde{P}^{\mathbf{q}}_{QQ'}(i\Omega_n) e^{-i\Omega_n \tau} \tag{4.38}$$

At the end, the dynamical self-energy can be expressed in this way,

$$(\tilde{\Sigma}_{GW})^{\mathbf{k}}_{i\sigma,j\sigma}(\tau) = -\frac{1}{N_k}\sum_{\mathbf{q}}\sum_{ab}\sum_{QQ'} G^{\mathbf{k}-\mathbf{q}}_{a\sigma,b\sigma}(\tau) V^{\mathbf{k}\mathbf{k}-\mathbf{q}}_{ia}(Q)\tilde{P}^{\mathbf{q}}_{QQ'}(\tau) V^{\mathbf{k}-\mathbf{q},\mathbf{k}}_{bj}(Q') \tag{4.39}$$

The dynamical self-energy is represented in a manner that allows for direct evaluation along the imaginary-time axis. Self-consistent iterations along this axis are both straightforward and stable. Additional approximations, such as "quasi-particle" approximations or adjustments to the off-diagonal self-energy structure, are unnecessary. Nonetheless, in order to determine real-frequency spectra and band gaps, an analytical continuation to real frequencies is essential. Recently developed techniques in complex analysis [41, 112] offer a precise means to carry out this critical step.

Chapter 5

Quantum Embedding Theories

Quantum embedding theory is a powerful approach in the field of quantum chemistry and condensed matter physics, which provides an effective way to describe the electronic structure of complex systems. The main idea behind this theory is to separate the intractable problem into a series of manageable calculations. Specifically speaking, a large-scale quantum system is divided into smaller, manageable strongly correlated subsystems and the surrounding weakly correlated environment. The subsystem is treated quantum mechanically while the interactions with the external environment are captured through effective potentials or self-energies.

Quantum embedding theory has several popular approximations, and among these, the Dynamical Mean-Field Theory (DMFT) [9, 55, 60, 113, 114] and Self-Energy Embedding Theory (SEET) [1–4] are two best known methods.

DMFT [9, 55, 60, 113, 114] is a non-perturbative method used to describe materials with strong electronic correlations. Within DMFT, the complex many-electron problem is mapped onto an effective impurity problem that can be solved numerically. The high-dimensional and intricate lattice problem is reduced to a single quantum impurity embedded in a mean-field that accounts for the lattice environment. DMFT has successfully described numerous phenomena observed in strongly correlated materials, such as Mott transitions, Kondo effect, and heavy fermion behavior.

SEET [1–4], on the other hand, is a more recent development in quantum embedding theory. The main idea of SEET is to approximate the self-energy, a crucial quantity in many-body theory, by embedding high-level self-energy calculations for small clusters into a lower-level description of the whole system. This allows the capturing of both

local and non-local correlations in a balanced way.

Both DMFT and SEET have found wide applications in the physics and chemistry of strongly correlated systems, and they represent important advancements in the field of quantum embedding theory. The development and refinement of these methods continue to be an active area of research.

5.1 Dynamical Mean-Field Theory

Dynamical Mean Field Theory (DMFT) is a powerful computational approach designed to address the intricate challenges posed by quantum many-body systems characterized by strong local Coulomb interactions [9, 113]. Over the years, DMFT has found extensive application, particularly in the study of the Hubbard model [9], and has been effectively integrated with electronic structure methods like LDA and GW to conduct materials simulations [55, 60]. The derivation of DMFT can be approached through various routes, and for a comprehensive understanding of these derivations, we direct interested readers to pertinent references [9, 113, 114].

At the essence of DMFT lies in the approximation of the self-energy $\Sigma(\mathbf{k}, i\omega_n)$ by its local contribution $\Sigma(i\omega_n)$. This approximation emanates from the transformative mapping of a lattice fermion model onto an impurity problem, where the impurity is defined as the unit cell embedded within a non-interacting dynamical mean field, representing the surrounding crystal [115, 116]. This dynamical mean field is determined through the DMFT self-consistency equations [9, 113].

In the limit of high spatial dimension (d) or a high coordination number (Z), non-local self-energies become negligible, and the mapping between the lattice model and the impurity problem becomes exact [115, 116]. In this scenario, all many-body effects are localized, and the approximation remains valid. However, for finite values of d and Z, the omission of momentum dependence in the self-energy signifies the neglect of non-local electron correlations beyond a unit cell. Nevertheless, DMFT tackles full many-body effects within a local unit cell in a non-perturbative manner by solving the impurity problem using high-level methods. The DMFT local self-energy corresponds to all skeleton self-energy diagrams, encompassing both internal and external indices, limited to a local unit cell. On the other hand, non-local (on-site) electron correlations are left unaddressed.

In the context of real materials, the electronic Hamiltonian typically encompasses a unit cell with a multitude of orbitals, yet only a select few are significantly correlated. In such cases, the strongly correlated subset extends beyond the unit cell's size. Consequently, the DMFT local approximation is adapted to accommodate this scenario, with a small subset A comprising the strongly correlated orbitals within the unit cell. The surrounding environment R includes orbitals not only from different unit cells but also from the same unit cell, excluding the correlated subset A. The local Green's function is then replaced by the local Green's function whose orbital indices are restricted to A.

We consider a system described by a Hamiltonian with one-body term t_{ij} and full two-body interaction v_{ijkl} in a finite orbital basis:

$$H = \sum_{ij}^{N} t_{ij} a_i^\dagger a_j + \sum_{ijkl}^{N} v_{ijkl} a_i^\dagger a_k^\dagger a_l a_j, \tag{5.1}$$

where the indices i, j, k and l enumerate all N basis orbitals present in the system.

The DMFT equations for this multi-orbital extension are derived, starting from the general multi-orbital Hamiltonian, and they demand that electron correlations beyond the correlated subset A are handled using advanced methods. Various quantum embedding techniques have been proposed to integrate DMFT with other electronic structure methods [55, 60]. These methods are often based on the local Green's function G and the bare Coulomb interactions U.

The foundation of DMFT bases on a Φ-derivable weakly correlated method, which approximates the self-energy of the entire crystal through truncated skeleton self-energy diagrams. This is mathematically represented as:

$$(\Sigma^{\text{weak}})^{\mathbf{k}}(i\omega_n) = F^{\text{weak}}[G^{\text{weak}}] \tag{5.2}$$

$$(G^{\text{weak}})^{\mathbf{k}}(i\omega_n) = [(i\omega_n + \mu)\mathbb{1} - t^{\mathbf{k}} - (\Sigma^{\text{weak}})^{\mathbf{k}}(i\omega_n)]^{-1} \tag{5.3}$$

Here, $F^{\text{weak}}[G]$ is a functional of the Green's function G that defines the self-energy diagrams of the weakly correlated solver.

For strongly correlated orbitals belonging to A, the local (on-site) Green's function is

given as:

$$G^{\mathbf{RR}}_{ij\in A}(i\omega_n) \approx \frac{1}{N_k}\sum_{\mathbf{k}}[(i\omega_n+\mu)\mathbb{1} - t^{\mathbf{k}} - (\Sigma^{\mathrm{DMFT}})^{\mathbf{k}}(i\omega_n)]^{-1}_{ij\in A} \tag{5.4}$$

This is further modified to include the local approximation:

$$(\Sigma^{\mathrm{DMFT}})^{\mathbf{k}}_{ij}(i\omega_n) = (\Sigma^{\mathrm{weak}})^{\mathbf{k}}_{ij}(i\omega_n) + [(\Sigma^{\mathrm{imp}})_{ij}(i\omega_n) - (\Sigma^{\mathrm{DC}})_{ij}(i\omega_n)]\delta_{ij\in A} \tag{5.5}$$

where $\Sigma^{\mathrm{DC}})(i\omega_n)$ represents the double counting (DC) self-energy responsible for the overlap between the strongly correlated and weakly correlated methods.

The self-consistency loop between the impurity Green's function and the local approximation is established, given by the Eq. 5.4 and

$$\Delta_A(i\omega_n) = (i\omega_n+\mu)\mathbb{1} - t^{\mathrm{imp}} - \Sigma^{\mathrm{imp}}(i\omega_n) - G^{\mathbf{RR},-1}_A(i\omega_n) \tag{5.6}$$

$$\Sigma^{\mathrm{imp}}(i\omega_n) = (i\omega_n+\mu)\mathbb{1} - t^{\mathrm{imp}} - \Delta_A(i\omega_n) - G^{\mathrm{imp,-1}}(i\omega_n) \tag{5.7}$$

5.2 Self-Energy Embedding Theory

5.2.1 The overview of self-energy embedding theory

Self-energy embedding theory (SEET) [1] can be comprehended as a conserving functional approximation to an exact Luttinger–Ward functional [94]. It is a versatile framework that enables the description of various physical properties, encompassing thermodynamic quantities such as energies, entropies, and frequency-dependent single-particle (Green's functions and self-energies) and two-particle quantities (susceptibilities) within a functional approach [94]. In this approach, a Φ-functional $\Phi[G]$ of the Green's function G, which contains all linked closed skeleton diagrams, and it satisfies

$$\frac{\delta\Phi}{\delta G} = \Sigma[G], \tag{5.8}$$

where the self-energy Σ is defined with respect to a non-interacting Green's function G_0 via the Dyson equation

$$G = G_0 + G_0\Sigma G. \tag{5.9}$$

The strength of the functional formalism lies in its inherent conservation of fundamental physical quantities, including electron number, energy, momentum, and angular momentum [117, 118]. This property ensures that quantities obtained through thermodynamic or coupling constant integration from non-interacting limits remain consistent [117], rendering functional theory a valuable tool for constructing both perturbative [96, 117, 119] and non-perturbative [2–4, 9, 114] diagrammatic approximations.

Nonetheless, approximations based on a Φ functional are not guaranteed to be self-consistent at the two-particle level, which can lead to disparities between the vertex functions used in one-particle self-energy calculations and those derived from functional differentiation in two-particle correlation functions, potentially violating crossing symmetries [120–122]. Resolving this issue and devising methods that inherently respect such symmetries are active areas of research [123, 124].

SEET, as delineated in studies [2–4], embarks upon the assumption that all orbitals in the system can be separated into distinct orbital subsets A_λ, each containing N_λ^A orbitals, alongside a remainder R comprising N^R orbitals. These categorizations satisfy conditions such that $N_\lambda^A << N$ for each a, and $N = \sum_{\lambda=1}^{M} N_\lambda^A + N^R$.

We presume that the orbitals located within each subset A_λ exhibit stronger correlations with each other than with any other orbitals in the system. As a result, their inner-subset impurity orbitals with indices $i, j \in A_\lambda$, sometimes called active orbitals, are characterized as groups comprising the most physically important orbitals for the problem that have correlations that are necessary to be determined using a non-perturbative method. In contrast, correlations between orbitals from two distinct sets A_λ and A_ν, where $\lambda \neq \nu$, as well as correlations related to the remaining system R, are predicted to be less pronounced. Therefore, they can be represented through a perturbative approach.

SEET unfolds in a two-step process, initially approximating the entire system's solution using a tractable yet potentially inaccurate Φ-derivable method. This method, often chosen from weak coupling methods (for instance GF2 [45, 46, 125] or the GW method [96]), yields the solution for both the self-energy and functional of the entire system. The weak correlation method's self-consistency assures the elimination of any initial starting point's influence, rendering the results self-contained. Following the weak correlation stage, correlated subspaces are identified based on certain criteria. These subspaces are then utilized to compute $[\Sigma_{\text{weak}}^A]_\lambda$ and $[\Phi_{\text{weak}}^A]_\lambda$ for each orbital subspace λ,

encompassing the weak correlation approximation exclusively for the correlated orbital subsets A_λ.

Subsequently, within each correlated subspace, the strongly correlated part of the problem $[\Sigma^A_{\text{strong}}]_\lambda$ is treated as a quantum impurity problem. This entails a transformation of interactions to the A-subspace, restricting the original interactions v_{ijkl} to this subset. The bare Green's functions G_0, which can be written in a block form as [1]

$$G_0 = \begin{pmatrix} \omega - t_A & -t_{\text{int}} \\ -t^\dagger_{\text{int}} & \omega - t_R \end{pmatrix}, \tag{5.10}$$

are also adjusted to new propagators $\mathcal{G}_0$ that account for a frequency-dependent 'hybridization function' Δ as

$$\mathcal{G}_0^{-1} = (G_0^{-1})^A - \Delta, \tag{5.11}$$

where the hybridization function is defined as

$$\Delta = [[(G_0^{-1})^{\text{int}} - \Sigma^{\text{int}}]^\dagger [(G_0^{-1})^R - \Sigma^R]^{-1} [(G_0^{-1})^{\text{int}} - \Sigma^{\text{int}}]]. \tag{5.12}$$

These propagators encompass the new hybridization function and are calculated for the strongly correlated orbital subsets, which defines a quantum impurity problem. A quantum impurity solver obtains an expression for the correlated $(G^{\text{imp}})^A$ given Δ and G_0 as well as a subset of interactions $v_{ijkl} \in A_\lambda$ in either spatial or energy basis. Using the impurity problem Dyson equation, the self-energy for a strongly correlated orbital subset is expressed as

$$[\Sigma^A_{\text{strong}}]_\lambda = \mathcal{G}_0^{-1} - ((G^{\text{imp}})^A)^{-1} \tag{5.13}$$

Once this strongly correlation $[\Sigma^A_{\text{strong}}]$ is known, the total self-energy Σ^A in subspace λ is evaluated as

$$[\Sigma^A]_\lambda = \Sigma^{\text{tot}}_{\text{weak}} + ([\Sigma^A_{\text{strong}}]_\lambda - [\Sigma^A_{\text{weak}}]_\lambda). \tag{5.14}$$

Thus the total self-energy Σ can be approximated in a matrix form as [1]

$$\Sigma^{\mathrm{SEET}} = \begin{bmatrix} [\Sigma^A]_1 & \Sigma^{\mathrm{int}} & \cdots & \cdots & \cdots \\ \Sigma^{\mathrm{int}} & [\Sigma^A]_2 & \Sigma^{\mathrm{int}} & \cdots & \cdots \\ \cdots & \cdots & \cdots & \cdots & \cdots \\ \cdots & \cdots & \Sigma^{\mathrm{int}} & [\Sigma^A]_M & \Sigma^{\mathrm{int}} \\ \cdots & \cdots & \cdots & \Sigma^{\mathrm{int}} & \Sigma^R \end{bmatrix}, \tag{5.15}$$

and the exact Φ-functional can be approximated as [1]

$$\Phi^{\mathrm{SEET}} = \Phi^{\mathrm{tot}}_{\mathrm{weak}} + \sum_{a=1}^{M} ([\Phi^A_{\mathrm{strong}}]_\lambda - [\Phi^A_{\mathrm{weak}}]_\lambda). \tag{5.16}$$

This framework ensures that non-local interactions outside of the A-subspace are treated at the perturbative level and offers an effective adjustment to the self-energy $[\Sigma^A_{\mathrm{strong}}]$ evaluated using a subset of local interactions.

5.2.2 SEET in real materials

The real space Green's function and the lattice (k-space) Green's function are related by the Fourier transform

$$G^{\mathbf{R}\mathbf{R}'}_{ij}(i\omega_n) = \frac{1}{V}\sum_{k} e^{i\mathbf{k}\mathbf{R}} G^{\mathbf{k}}_{ij}(i\omega_n) e^{-i\mathbf{k}\mathbf{R}'}. \tag{5.17}$$

We consider the GW method as the conserving low-order approximation in our case, then its momentum-resolved Green's function of the entire lattice is defined as [6]

$$(G^{\mathrm{GW}}(i\omega_n))^{\mathbf{k}} = [(i\omega_n + \mu)\mathbb{1} - t^{\mathbf{k}} - (\Sigma^{\mathrm{GW}}(i\omega_n))^{\mathbf{k}}]^{-1}, \tag{5.18}$$

where

$$(\Sigma^{\mathrm{GW}}(i\omega_n))^{\mathbf{k}} = (\Sigma^{\mathrm{GW}}_{\infty})^{\mathbf{k}} + (\Sigma^{\mathrm{GW}}(i\omega_n))^{\mathbf{k}}. \tag{5.19}$$

As a result of embedding procedure, a lattice Green's function can be expressed in this way: [6]

$$(G(i\omega_n))^{\mathbf{k}} = [(i\omega_n + \mu)\mathbb{1} - t^{\mathbf{k}} - \Sigma^{\mathbf{k}}]^{-1}, \tag{5.20}$$

where

$$\Sigma_{ij}^{\mathbf{k}} = (\Sigma^{\mathrm{GW}})_{ij}^{\mathbf{k}} + \sum_{\lambda=1}^{M}((\Sigma_{A_\lambda}^{\mathrm{imp}})_{ij} - (\Sigma_{A_\lambda}^{\mathrm{DC}})_{ij})\delta_{(ij)\in A_\lambda} \tag{5.21}$$

with $\Sigma^{\mathrm{imp}} = \Sigma_{\infty}^{\mathrm{imp}} + \Sigma^{\mathrm{GW}}(i\omega_n)$ encapsulates the self-energy diagrams that are added nonperturbatively and $\Sigma^{\text{DC-GW}} = \Sigma_{\infty}^{\text{DC-GW}} + \Sigma^{\text{DC-GW}}(i\omega_n)$ represents the removal of those diagrams that are present both in the GW resolution and the nonperturbative formulation.

The Fourier transform results in the following structure of the self-energy matrix in the real space

$$\Sigma_{ij}^{\mathbf{R}\mathbf{R}'} = (\Sigma^{\mathrm{GW}})_{ij}^{\mathbf{R}\mathbf{R}'} + \sum_{\lambda=1}^{M}((\Sigma_{A_\lambda}^{\mathrm{imp}})_{ij} - (\Sigma_{A_\lambda}^{\text{DC-GW}})_{ij})\delta_{\mathbf{R}\mathbf{R}'}\delta_{(ij)\in A_\lambda}. \tag{5.22}$$

For unit cells separated from the central cell ($\mathbf{R} \neq \mathbf{R}'$), the self-energies are addressed at a weakly correlated level, denoted as $\Sigma_{ij}^{\mathbf{R}\mathbf{R}'} = (\Sigma^{\mathrm{GW}})_{ij}^{\mathbf{R}\mathbf{R}'}$, while the self-energy within the local central cell ($\mathbf{R} = \mathbf{R}'$) incorporates nonperturbative corrections $(\Sigma_{A_\lambda}^{\mathrm{imp}})_{ij}$ for each orbital group A_λ.

Then the Green's function in the real space can be written as

$$(G(i\omega_n))_{ij\in A_\lambda}^{\mathbf{R}\mathbf{R}} = [(i\omega_n + \mu)\mathbb{1} - t_{ij\in A_\lambda}^{\mathbf{R}\mathbf{R}} - \Sigma_{ij\in A_\lambda}^{\mathbf{R}\mathbf{R}}(i\omega_n) - \Delta_{ij}^{A_\lambda}(i\omega_n)]^{-1}. \tag{5.23}$$

The hybridization matrix $\Delta_{ij}^{A_\lambda}(i\omega_n)$ arises since an inverse of a subset is not equal to a subset of an inverse, namely

$$[(G(i\omega_n))_{ij\in A_\lambda}^{\mathbf{R}\mathbf{R}}]^{-1} \neq [((G(i\omega_n))^{\mathbf{R}\mathbf{R}'})^{-1}]_{ij\in A_\lambda}^{\mathbf{R}\mathbf{R}} = [(i\omega_n+\mu)\mathbb{1} - t_{ij\in A_\lambda}^{\mathbf{R}\mathbf{R}} - \Sigma_{ij\in A_\lambda}^{\mathbf{R}\mathbf{R}}]^{-1}. \tag{5.24}$$

5.2.3 Bath fitting

We can approximate the infinite, continuous bath used to describe hybridization by a finite, discrete one. This involves determining a finite number of bath orbital energies ϵ_b and impurity-bath couplings V_{ib} to reconstruct the hybridization $\Delta(i\omega_n)$:

$$[\Delta(i\omega_n)]_{ij} \approx [\Delta^{\mathrm{fit}}(i\omega_n)]_{ij} = \sum_{b}^{N_b} \frac{V_{ib}^* V_{jb}}{i\omega_n - \epsilon_b} \tag{5.25}$$

and thereby create the impurity Hamiltonian within a finite basis. It's important to note that the indices b, ranging from 1 to N_b, correspond to the bath sites, while the i and j indices are used to label the impurity orbitals. Typically, the selection of bath orbital energies ϵ_b and impurity-bath couplings V_{ib} is optimized to minimize the overall fitting error, $[\Delta(i\omega_n)]_{ij} - [\Delta^{\text{fit}}(i\omega_n)]_{ij}$. Additional insights into the bath fitting procedure can be found in the condensed matter literature [52, 126].

5.2.4 Solution of the impurity model

SEET is a method of computational physics that utilizes the concept of embedding nonperturbative impurity models into a self-consistently adjusted hybridization with the environment. Solving impurity models, however, is a challenging task due to its computational complexity. Therefore, quantum impurity solvers such as quantum Monte Carlo (QMC) [127], numerical renormalization group (NRG) [128], exact diagonalization (ED) [51], configuration interaction (CI) [129, 130], or coupled clusters [131, 132], are needed. These solvers are sophisticated computational algorithms that are capable of handling the complex computations involved in solving impurity models.

SEET, while requiring the solution of impurity problems that may involve strong interaction, has the advantage of being able to treat multiple active spaces. This keeps the size of the impurities being treated relatively moderate, which in turn helps in managing computational complexity.

We used ED as an impurity solver for SEET problems in our case. It requires the discretization of the continuous hybridization function and its approximation by a finite number of discrete bath sites. The symmetric orthogonal basis allows for a simplification where off-diagonal elements of the hybridization function can often be neglected due to their significantly smaller magnitude compared to diagonal elements.

The approximation of the hybridization function is achieved by minimizing the fit residue using a bound-constrained nonlinear least-square method [133, 134]. This method enforces the constraint that V_{ib} are positive and ϵ_b are in the vicinity of the Fermi energy.

For practical implementation, the number of bath sites used per orbital varies depending on the number of orbitals in the problem. For example, for a two-orbital problem, 5 bath sites per orbital are used, while for a four-orbital problem only 3 bath sites per orbital are used. The impurity problems are then solved using an open-source ED

impurity solver [135].

5.2.5 Iterative self-consistent process

Inner-loop SEET process

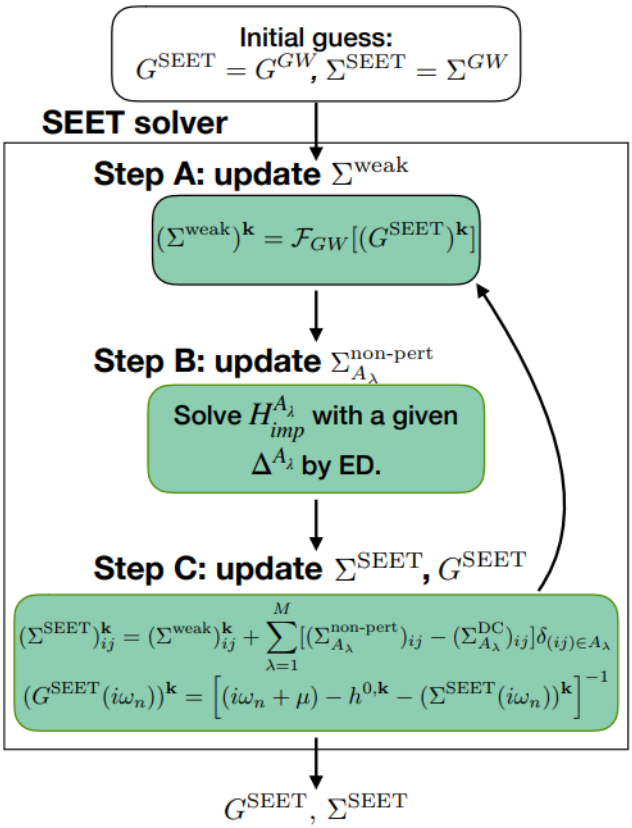

Figure 5.1: Workflow of self-consistent inner-loop SEET. From [26].

We can reorder the terms in Eq. 5.23 by splitting the static and dynamic part of each self-energy contribution: [26]

$$[(G(i\omega_n))^{\mathbf{RR}}_{ij\in A_\lambda}]^{-1} = [(i\omega_n + \mu)\mathbb{1} - \tilde{t}^{\mathbf{RR}}_{ij\in A_\lambda} - \Sigma^{\mathrm{corr},\mathbf{RR}}_{ij\in A_\lambda}(i\omega_n) - \Sigma^{\mathrm{imp}}_{ij\in A_\lambda}(i\omega_n) - \Delta^{A_\lambda}_{ij}(i\omega_n)], \tag{5.26}$$

where

$$\tilde{t}^{\mathbf{RR}}_{ij\in A_\lambda} = t^{\mathbf{RR}}_{ij\in A_\lambda} + (\Sigma^{\mathrm{GW}}_{\infty})^{\mathbf{RR}}_{ij\in A_\lambda} - (\Sigma^{\mathrm{DC}}_{A_\lambda,\infty})_{ij\in A_\lambda} \tag{5.27}$$

is the frequency-independent renormalized non-interacting Hamiltonian and

$$\Sigma^{\mathrm{corr},\mathbf{RR}}_{ij\in A_\lambda} = (\Sigma^{\mathrm{GW}}_{\mathrm{corr}})^{\mathbf{RR}}_{ij\in A_\lambda} - (\Sigma^{\mathrm{DC}}_{A_\lambda,\mathrm{corr}})_{ij\in A_\lambda} \tag{5.28}$$

is the local dynamic self-energy without double counting contribution.

In order to solve $\Sigma^{\mathrm{imp}}_{A_\lambda}$, we define the auxiliary propagator

$$g^{-1}_{A_\lambda} = g^{0,-1}_{A_\lambda} - \Sigma^{\mathrm{imp}}_{ij\in A_\lambda}, \tag{5.29}$$

where the inverse of the non-interacting auxiliary counterpart $g^{0,-1}_{A_\lambda}$ is defined as

$$g^{0,-1}_{A_\lambda} = (i\omega_n + \mu)\mathbb{1} - \tilde{t}^{\mathbf{RR}}_{ij\in A_\lambda} - \Delta^{A_\lambda}_{ij\in A_\lambda}. \tag{5.30}$$

The Green's function of Eq. 5.29 can then be obtained by solving an auxiliary quantum impurity problem [9]

$$\begin{aligned} H^{A_\lambda}_{\mathrm{imp}} = &\sum_{ij\in A_\lambda,\sigma} (\tilde{t}_{ij\sigma} - \mu\delta_{ij}) c^\dagger_{i\sigma} c_{j\sigma} + \sum_{b\sigma} \epsilon_{b\sigma} a^\dagger_{b\sigma} a_{b\sigma} \\ &+ \sum_{i\in A_\lambda,b,\sigma} (V_{ib\sigma} c^\dagger_{i\sigma} a_{b\sigma} + h.c.) + \frac{1}{2} \sum_{ijkl\in A_\lambda,\sigma\sigma'} v_{ijkl} c^\dagger_{i\sigma} c^\dagger_{k\sigma'} c_{l\sigma'} c_{j\sigma} \end{aligned} \tag{5.31}$$

The equations for Σ (as a function of G) and G (as a function of Σ) give rise to self-consistent equations that are Φ-derivable, ensuring conservation and thermodynamic consistency [1]. The SEET equations undergo iterative solving until convergence is achieved for all relevant quantities. This self-consistency process is visualized in Figure 5.1.

In step A of the process, a single iteration of GW, denoted as $F_{\mathrm{GW}}[(G^{\mathrm{SEET}})^{\mathbf{k}}]$, is executed to update $(\Sigma^{\mathrm{GW}})^{\mathbf{k}}$ for the entire system. Additionally, step B involves solving $H^{A_\lambda}_{\mathrm{imp}}$, which corresponds to the Hamiltonian for a specific impurity subset A_λ, using a quantum impurity solver. In cases where multiple subspaces A_λ are defined, $H^{A_\lambda}_{\mathrm{imp}}$ for each subset is independently solved. Finally, Σ^{SEET} and G^{SEET} are updated according to Eq. 5.20 and 5.21 with the new Σ^{GW} and $\Sigma^{\mathrm{imp}}_{A_\lambda}$ values.

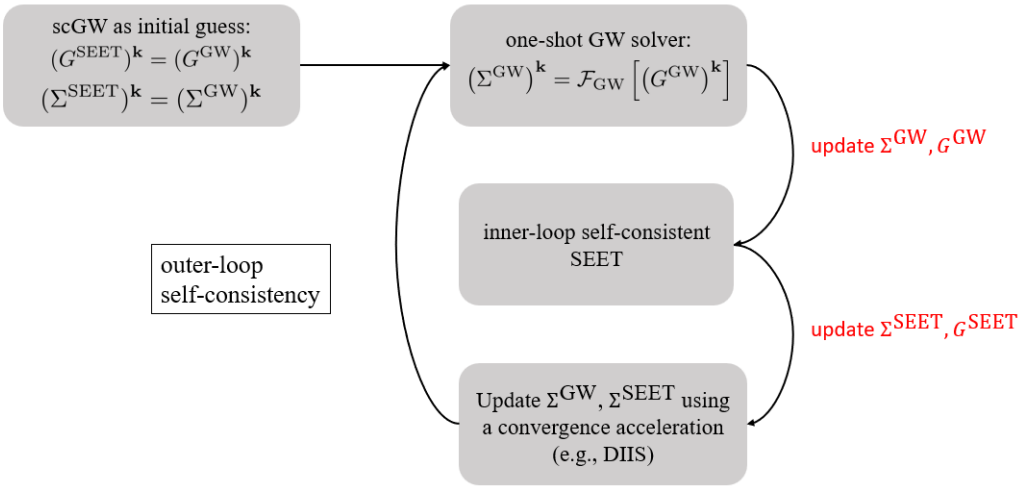

Figure 5.2: Workflow of self-consistent outer-loop SEET.

Outer-loop SEET process

In our computational approach, we employ a stepwise calculation scheme [36] that ensures the self-consistency and accuracy of our results. Initially, we utilize the outcomes obtained from the self-consistent GW calculation as our starting point. Subsequently, we employ a one-shot GW solver to bring about adjustments to the entire environment, focusing on the domain of weak correlations. This modification serves to accommodate the effects of weak correlations within the system.

Once the environment has been updated in this manner, we proceed to apply the inner-loop self-consistent SEET methodology. This inner loop involves the iterative updating of both the self-energy and the Green's function, refining their accuracy in the process. To further enhance the convergence of our computations, we employ techniques such as direct inversion in the iterative subspace (DIIS) [136] to update the self-energy components of both the weakly correlated portion and the overall system.

Following this, we reevaluate the environment, allowing for relaxation, and subsequently repeat all the aforementioned procedures to attain full self-consistency. This comprehensive iterative process is referred to as the outer-loop self-consistent SEET.

The primary objective of the outer-loop self-consistency is to accommodate the relaxation of weakly correlated orbitals in the presence of strong correlations stemming from impurity orbitals. It is important to note that the omission of the outer-loop self-

consistency is justified when the weakly correlated approach, such as the self-consistent GW (scGW) method [8] used in our current work, adequately captures the qualitative aspects of most correlations within the solid. Our empirical findings suggest that the outer loop becomes essential when scGW, or any analogous weakly correlated method, delivers a qualitatively incorrect description of the density of states. In such cases, the outer loop becomes indispensable to attain qualitatively accurate outcomes. However, when the weakly correlated method provides a qualitatively sound representation, the outer loop may primarily be necessary to achieve the highest levels of quantitative accuracy and can be omitted, leading to computational savings in most instances.

5.2.6 Iterative acceleration algorithms

Damping

Damping is a well-established iterative acceleration technique frequently employed in various computational procedures, including those in the realm of scientific simulations and numerical methods. This subsection delves into the principles underlying damping, elucidating its significance and the role it plays in enhancing convergence.

Damping, as a technique, introduces a damping factor, conventionally designated as x. This damping factor holds a pivotal role in determining the balance between the results of the current iteration and those of the previous iteration within the iterative process. In essence, it serves as a numerical ratio that combines a fraction of x times the outcome of the ongoing iteration with a complementary fraction of $(1 - x)$ times the result from the preceding iteration.

The value assigned to the damping factor x has a profound influence on the iterative process. Specifically, a smaller damping factor corresponds to a higher weight assigned to the results obtained from the current iteration when blending it with the information from the previous iteration. This, in effect, places more emphasis on the most recent updates, thereby expediting convergence by steering the iterative procedure towards its final outcome.

The incorporation of damping into iterative algorithms often leads to a more stable and expedited convergence, particularly in scenarios where oscillations or slow convergence pose challenges. The selection of an appropriate damping factor is a crucial consideration, as it directly impacts the trade-off between stability and convergence speed

in iterative processes.

Direct Inversion in the Iterative Subspace

We first define a general electronic structure solver functional $F = F[x] = x$, where x represents any quantities that requires to achieve self-consistency. In Direct Inversion in the Iterative Subspace (DIIS), a history of certain number of previous iterations is considered [136–138]. We assume the exact solution x can be expressed as a linear combination of previous guess solutions x_i,

$$x = \sum_{i=1}^{m} c_i x_i. \tag{5.32}$$

On the other hand, we define an intermediate result $\tilde{x}_{i+1}$ and residual e_i

$$\tilde{x}_{i+1} = F[x_i] \tag{5.33}$$

$$e_i = \tilde{x}_{i+1} - x_i, \tag{5.34}$$

and then we will update x_{m+1} as

$$x_{m+1} = \sum_{i=1}^{m} c_i \tilde{x}_{i+1} = \sum_{i=1}^{m} c_i x_i + \sum_{i=1}^{m} c_i e_i \tag{5.35}$$

By comparing Eq. 5.32 and 5.35, it is obvious that if the quantity achieves self-consistency, the suitable coefficient c_i will satisfy

$$\sum_{i=1}^{m} c_i e_i = 0 \tag{5.36}$$

In addition, when exact solution x is achieved,

$$x_i = x, \forall i, \tag{5.37}$$

$$x_{m+1} = \sum_{i=1}^{m} c_i x_i = x \sum_{i=1}^{m} c_i = x \tag{5.38}$$

Thus

$$\sum_{i=1}^{m} c_i = 1 \tag{5.39}$$

The DIIS methodology aims to minimize the Euclidean norm of the extrapolated error for the determination of extrapolation coefficients. The associated Lagrangian function for minimizing the squared norm, as detailed in [139], can be expressed as follows:

$$L^{\mathrm{DIIS}}(c_i, \lambda) = \frac{1}{2} \sum_{ij} c_i B_{ij} c_j - \lambda \left(1 - \sum_i c_i \right) \qquad B_{ij} = \langle e_i, e_j \rangle \tag{5.40}$$

In the context of this formulation, assuming that the extrapolation coefficients are real, differentiation of this Lagrangian yields a necessary condition for achieving the minimum

$$\begin{pmatrix} \Re B_{11} & \cdots & \Re B_{1n} & 1 \\ \cdots & \cdots & \cdots & \cdots \\ \Re B_{n1} & \cdots & \Re B_{nn} & 1 \\ 1 & \cdots & 1 & 0 \end{pmatrix} \begin{pmatrix} c_1 \\ \cdots \\ c_n \\ 1 \end{pmatrix} = \begin{pmatrix} 0 \\ \cdots \\ 0 \\ 1 \end{pmatrix} \tag{5.41}$$

While Equation 5.41 provides an analytical formula for computing the c_i values, it's important to note that there remains a degree of flexibility in determining the components of the x vector. In our specific context, we define this vector as follows:

$$x = \{F, \Sigma(\tau), \mu\} \tag{5.42}$$

Here, F, $\Sigma(\tau)$, and μ correspond to the Fock matrix, self-energy, and chemical potential, respectively. The selection of these particular components within the x vector should be driven by the underlying physical problems that are of interest.

Chapter 6

Spectral Properties and Thermodynamic Quantities

Following the comprehensive exploration of the self-consistent calculation framework in the preceding chapters, it becomes imperative to delve into the subsequent stages of our analysis. In this chapter, we navigate the complex realm of spectral functions and thermodynamic quantities, which serve as essential tools for the interpretation and presentation of our calculation results. To dissect and comprehend these subjects thoroughly, we employ a multi-faceted approach, with each component sequentially unveiled in the following sections.

Our journey begins with the quest for a high-precision representation in momentum space (commonly referred to as k-space). To achieve this, we exploit Wannier interpolation [42, 140, 141], a powerful mathematical tool that allows us to interpolate electronic band structures within the k-space domain. With a finely resolved k-space representation in hand, our focus naturally turns to identifying the orbitals by orbital projection.

Having achieved a good k resolution and identified our orbitals, we move onto the process of analytical continuation. This pivotal procedure serves as the bridge between the data residing on the imaginary axis and the real axis so that we can obtain the spectral function from the Matsubara Green's function. Within this domain, we introduce two distinct methods: the Maximum Entropy Method (MaxEnt) [38–40] and the Nevanlinna analytical continuation [41], offering diverse avenues for this crucial transformation.

Finally, for evaluating energies, the thermodynamic quantities can use statistical nature of the theory. Details are presented in Section 6.4.

6.1 Wannier interpolation

In the field of electronic structure calculations, the study of electron band structure in momentum space (k space) is a basic work. However, practical considerations often require us to use a discrete grid in k-space, which presents challenges when we try to extrapolate our insights to regions beyond this grid. This dilemma requires the intervention of a powerful technique, namely Wannier interpolation [42, 140, 141], which plays a key role in solving this problem.

The essence of Wannier interpolation lies in the transformation from the discrete k-space dispersion to a real space representation, followed by an interpolation on the real space structure to get the value of quantities on any momenta in the Brillouin zone. This transformation is founded on the implicit assumption that beyond the scope of this real space representation, electronic correlations effectively vanish. This locality approximation, while seemingly simplistic, proves to be a reasonable assumption in scenarios where the correlations indeed diminish significantly outside the system.

One of the main motivations for employing Wannier interpolation is to overcome the limitation of having only a restricted number of k points on a discrete grid. It is often necessary to evaluate the spectral function of any k-point throughout the Brillouin zone. Wannier interpolation facilitates this by allowing us to construct a smooth and continuous representation of the electronic band structure beyond a finite grid of points.

The Wannier interpolation of the self-energy can be performed by

$$\Sigma_{ij}^{\mathbf{R}} = \frac{1}{N_k} \sum_{\mathbf{k}} \Sigma_{ij}^{\mathbf{k}} e^{-i\mathbf{k}\mathbf{R}} \tag{6.1}$$

$$\Sigma_{ij}^{\mathbf{k}'} = \sum_{\mathbf{R}} \Sigma_{ij}^{\mathbf{R}} e^{i\mathbf{k}'\mathbf{R}} \tag{6.2}$$

where $\mathbf{k}$ comes from the coarse Brillouin zone sampling and $\mathbf{k}'$ is arbitrary k point that requires interpolation. Other quantities such as Fock matrix and Green's function can be interpolated in the same way.

6.2 Orbital orthogonalization and projection

The utilization of the GW approximation and Wannier interpolation is executed in the basis of the atomic orbitals (AO). It is noteworthy that within this basis, obtaining analytically continued results is difficult as the spectral functions are not strictly positive, nor normalized. To facilitate the SEET embedding procedure, as well as the operation of the impurity solvers, a transformation of the Green's function into an orthogonal basis, denoted as G^{orth}, is necessitated and achieved through the following relation:

$$G^{\mathrm{orth}} = XGX^*, \tag{6.3}$$

In our case, we adopt a symmetrical orbital orthogonalization strategy [73], specifically employing the transformation matrix X given by:

$$X = S^{1/2}, \tag{6.4}$$

Where S represents the overlap matrix as defined in Eq. 4.9. This particular basis, referred to as the symmetric atomic orbitals (SAO) basis [73], is thereby employed.

Given that the spectral function is inherently frequency-dependent and impossible to be represented in a single basis for all frequencies, we have empirically observed that the density matrix within the SAO basis is nearly diagonal. This observation suggests that the SAO basis is well-suited for orbital projection. Consequently, we study the orbital characters in proximity to the Fermi surface by projecting onto the corresponding SAO basis.

Let's consider the elemental semiconductor Silicon (Si) as a straightforward example to elucidate the concept of orbital character and the role of orbital projection. Silicon is composed of atoms arranged in a crystal lattice, and its electronic structure is central to its properties as a semiconductor.

In the realm of solid-state physics and electronic structure calculations, understanding the electronic properties of Silicon relies on the analysis of its orbital character. Orbital character essentially pertains to the specific contribution of atomic orbitals, such as the $3p$ or $3s$ orbitals in the case of Silicon, to the electronic states in the material. It allows us to discern which orbitals are primarily responsible for forming the energy bands and, subsequently, influencing the material's electrical and optical behavior.

To gain insights into the orbital character in Silicon, we employ the technique of orbital projection. Orbital projection is a method that enables us to isolate and quantify the contribution of specific atomic orbitals to the electronic states in a crystal. By performing orbital projection in Silicon, we can discern the extent to which, for example, the $3p$ orbitals of Silicon atoms contribute to the valence and conduction bands. This information is crucial for understanding the semiconductor's electronic behavior, as it elucidates the nature of the charge carriers (electrons and holes) and their mobility.

6.3 Analytical continuation

Analytical continuation [37] emerges as a critical challenge when transitioning from the realm of imaginary axis to the real axis, transforming correlation functions computed in numerical simulations into response or spectral functions accessible to experimental observation. In numerical simulations, correlation functions are naturally obtained in imaginary time (or the Fourier transform known as Matsubara frequency). However, the real axis counterparts of these functions, which are of paramount importance for experimental measurements, remain elusive through standard numerical techniques.

We start with the imaginary time Green's function

$$G(\tau) = -\langle c(\tau)c^{\dagger}(0)\rangle, \tag{6.5}$$

which is periodic for bosonic and anti-periodic for fermionic particles within $\tau \in [0, \beta]$. The Matsubara Green's function can be obtained from the imaginary time Green's function by Fourier transform:

$$G(i\omega_n) = \int_0^{\beta} e^{i\omega_n \tau} G(\tau). \tag{6.6}$$

The Matsubara frequencies are defined as $i\omega_n = 2\pi(n + 1/2)/\beta$ for fermionic operators and $i\omega_n = 2\pi n/\beta$ for bosonic operators.

In the case of fermions, Green's function on the imaginary axis is connected to that

on the real axis by

$$G(i\omega_n) = -\frac{1}{\pi}\int_{-\infty}^{\infty} \frac{d\omega \mathrm{Im}G(\omega)}{i\omega_n - \omega} \tag{6.7}$$

$$G(\tau_n) = \frac{1}{\pi}\int_{-\infty}^{\infty} \frac{d\omega \mathrm{Im}G(\omega)e^{-\tau_n\omega}}{1+e^{-\beta\omega}} \tag{6.8}$$

where τ has been discretized in some manner to N points.

The imaginary part of the Green's function defines the spectral function

$$A(\omega) = -\frac{1}{\pi}\mathrm{Im}G(\omega) \tag{6.9}$$

At the heart of this intriguing dilemma lies the exceptional ill-conditioned nature of the transformation from the imaginary axis to the real axis. Even the slightest deviations in the input data can trigger significant fluctuations in the resulting output data. Consequently, this renders direct transformations practically unfeasible in the quest to bridge the gap between the numerical world and real-world observations.

6.3.1 Maximum Entropy Method

The Maximum Entropy Method [38–40], often abbreviated as MaxEnt, is a well-established mathematical technique used in a multitude of scientific and engineering fields. The method is based on the principle of maximum entropy, which states that the probability distribution, which best represents the current state of knowledge, is the one with the largest entropy. MaxEnt is particularly useful in situations where one needs to extrapolate, interpolate, or smooth data.

The method has been widely used in the context of image reconstruction, spectral analysis, and machine learning. In the field of numerical simulations, it is especially useful in the analytical continuation of data from the imaginary to the real axis. By providing a systematic approach to handle the ill-posed nature of the problem, the Maximum Entropy Method offers a significant advantage over direct methods.

Despite its apparent complexity, the underlying concept of MaxEnt is straightforward: among all possible solutions to a problem, the one that should be chosen is the one that makes the least assumptions beyond the known constraints.

Consider a truncation of Green's function to N components, obtained by averaging a

set of M estimates for each component $G_n^{(i)}$

$$G_n = \frac{1}{M}\sum_{i=1}^{M} G_n^{(j)}, \tag{6.10}$$

where $G_n^{(i)}$ are independent and Gaussian distributed. Then the covariance matrix for different correlated components is

$$C_{nm} = \frac{1}{M(M-1)}\sum_{j=1}^{M}(G_n - G_n^{(j)})(G_m - G_m^j) \tag{6.11}$$

From Eq. 6.9, [40]

$$G_n = G(\tau_n) = \int_{-\infty}^{\infty} d\omega A(\omega) K_n(\omega) \tag{6.12}$$

where

$$K_n(\omega) = K(\tau_n, \omega) = -\frac{e^{-\tau_n \omega}}{1 + e^{-\beta\omega}} \tag{6.13}$$

is the kernel of the analytical continuation, here for a transformation of a fermionic Green's function from imaginary time to real frequencies.

Based on Eq. 6.12, a candidate spectral function $A(\omega)$ on the real axis and the associated kernel are able to create an estimate of discretized Green's function $\bar{G}_n$. A "goodness of fit" quantity χ^2 can be introduced to evaluate the consistency between $A(\omega)$ and G_n [40]

$$\chi^2 = \sum_{n,m}^{M}(\bar{G}_n - G_n)^* C_{nm}^{-1}(\bar{G}_m - G_m) \tag{6.14}$$

For the computational solution of Eq. 6.12, the most straightforward approach is to utilize a least squares fitting routine. This method aims to minimize a functional, as defined in Eq. 6.14. While back-continuation is a simple procedure that yields a distinct outcome, the inversion of Eq. 6.12 presents an ill-conditioned problem. In other words, there exist multiple solutions A for that fulfill the conditions $G = KA$ specified by within the range of uncertainty given by C_{nm} [40].

In the Maximum Entropy method, an entropy term S is considered to help regularize the solutions, then the functional that requires to be minimized becomes [40]

$$Q = \frac{1}{2}\chi^2 - \alpha S[A]. \tag{6.15}$$

Shannon entropy [142] is used to minimize spurious correlations between data [143]. Its application has a restriction that the resulting spectral function is finite and positive, so it can be treated as a probability density [39].

Entropy can be defined with respect to a reference spectral function, the default model $d(\omega)$:

$$S[A] = -\int d\omega A(\omega) \ln \frac{A(\omega)}{d(\omega)} \tag{6.16}$$

When $\alpha \gg 1$, the default model ensures a sensible solution that is ideally independent of the input data; while when $\alpha \ll 1$, this functional recover the least square fit. The final result is often insensitive to the choice of the default model.

6.3.2 Nevanlinna analytical continuation

The Maximum Entropy method is a widely-used technique in quantum physics and condensed matter physics. However, it primarily focuses on fitting, rather than interpolating, spectral functions to Matsubara data, with the added requirement of satisfying specified error bars. While MaxEnt is successful in handling noisy data, it faces challenges when dealing with high-frequency information, sharp peaks, and spectral functions containing multiple features.

A recent breakthrough, detailed in a recent letter by Fei et al. (2021) [41], introduces a novel approach that overcomes these limitations. This method employs a continued fraction interpolation of Matsubara data, utilizing the analytical "Nevanlinna" structure of the Green's function.

The core idea revolves around the relationship between the Matsubara Green's function, denoted as $\mathcal{G}(i\omega_n)$, and the retarded Green's function, $G^R(\omega+i\eta)$. By consistently replacing the variables $i\omega$ and $\omega + i\eta$ with a single complex variable, denoted as z, this method involves analytical continuation to obtain the desired G^R from $\mathcal{G}$.

In complex analysis, a Nevanlinna function is a complex function characterized by its analyticity in the open upper half-plane, denoted as $\mathcal{C}^+$, and its non-negative imaginary part, meaning it maps into the closed upper half-plane $\overline{\mathcal{C}^+}$ [144]. These Nevanlinna functions are denoted as members of the class N, and they possess specific properties that make them highly suitable for this interpolation process.

To perform the analytical continuation from the Matsubara frequencies to the real

axis, the goal is to find an interpolant for $\mathcal{NG}$ within the class of Nevanlinna functions N. The constructed function passes through all Matsubara points, as shown in Figure 6.1, and maintains a positive imaginary part in the upper half-plane, extending just above the real axis. This property ensures the intrinsic positivity of the resulting spectral function:

$$A(\omega) = \lim_{\eta \to 0^+} \frac{1}{\pi} \mathrm{Im}[\mathcal{NG}(\omega + i\eta)] \tag{6.17}$$

This approach notably overcomes common issues associated with other interpolation methods, such as Pade interpolants [145].

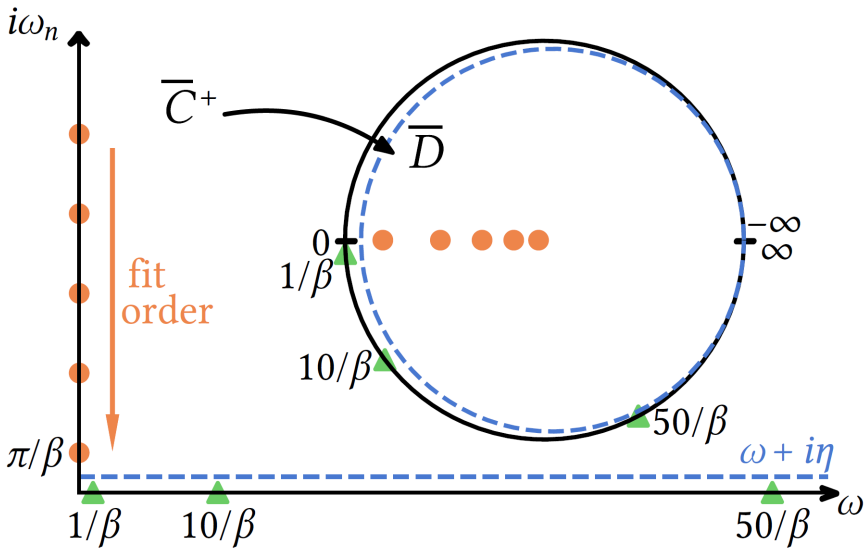

Figure 6.1: Analytical continuation setup with fermion Matsubara points at $i\omega_n$ and real frequency axis ω. The retarded Green's function is evaluated η (small) above the real axis. Inset: Mobius transform of the closed upper half plane $\overline{\mathcal{C}^+}$ to the closed unit disk $\overline{\mathcal{D}}$. From [41].

The construction of Nevanlinna interpolants is accomplished using the Schur algorithm [146]. Originally designed as a continued fraction expansion for all holomorphic disk functions mapping from the open unit disk, $\mathcal{D} = z : |z| < 1$, to the closed unit disk, $\overline{\mathcal{D}}$, this algorithm has been modified to expand contractive functions [147]. These contractive functions are holomorphic and map from $\mathcal{C}^+$ to $\overline{D}$.

An essential component of this methodology is the invertible Mobius transform, represented by the function $h(z)$:

$$z \mapsto \frac{z - i}{z + i} \tag{6.18}$$

This transform effectively maps Nevanlinna functions one-to-one to contractive functions, as shown in Figure 6.1. As a result, the Nevanlinna interpolation problem is transformed into the challenge of constructing the contractive function θ, which is Mobius transformed from $\mathcal{NG}$:

$$\theta(Y_i) = \lambda_i = h(C_i) = \frac{C_i - i}{C_i + i}, \ i = 1, 2, \dots, M, \tag{6.19}$$

where Y_i is the ith Matsubara frequency, C_i is the value of $\mathcal{NG}$ at Y_i, and λ_i is the value of θ at Y_i.

A particularly remarkable aspect of this approach is the existence criterion for Nevanlinna interpolants, which is directly based on input data. This criterion is a generalization of the Pick criterion. Nevanlinna interpolants exist if and only if the Pick matrix is positive semidefinite:

$$\left[\frac{1 - \lambda_i \lambda_j^*}{1 - h(Y_i)h(Y_j)^*}\right]_{i,j}, \ i, j = 1, 2, \dots, M. \tag{6.20}$$

Uniqueness of the solution is ensured only if this matrix is singular.

The iterative construction of the contractive interpolant is a crucial part of the methodology. A contractive function $\theta(z)$

$$\theta(z) = \frac{\frac{z - Y_1}{z - Y_1^*}\tilde{\theta}(z) + \gamma_1}{\gamma_1^* \frac{z - Y_1}{z - Y_1^*}\tilde{\theta}(z) + 1} \tag{6.21}$$

satisfies the relationship $\theta(Y_1) = \gamma_1$ for any contractive function $\tilde{\theta}(z)$ [147].

Given an interpolation problem for j nodes, $\theta(Y_k) = \gamma_k, k = 1, \dots, j$, Equation 6.21 defines an interpolation problem for the $j - 1$ nodes, $Y_2, \dots, Y_j$, for $\tilde{\theta}$. This equation arises from Schur's expansion for any disk function with a known value γ_1 at the origin [148], facilitated by the conformal map $g : \mathcal{C}^+ \to \mathcal{D}$:

$$z \mapsto \frac{z - Y_1}{z - Y_1^*} \tag{6.22}$$

Equation 6.21 suggests an iterative algorithm that starts from the original interpolation problem for $\theta_1 = \theta$ involving all M points. This defines an interpolation problem

θ_2 for $M-1$ points, and this process continues iteratively. Concatenating these interpolation problems results in a continued fraction form for θ. Each step allows for the flexibility of choosing an arbitrary contractive function θ_{M+1} at the final stage, derived from $\theta_M(Y_M) = \phi_M$, thus satisfying the interpolation problem

The recursive final θ can be expressed in a matrix form,

$$\theta(z)[z;\theta_{M+1}(z)] = \frac{a(z)\theta_{M+1}(z) + b(z)}{c(z)\theta_{M+1}(z) + d(z)}, \tag{6.23}$$

where

$$\begin{pmatrix} a(z) & b(z) \\ c(z) & d(z) \end{pmatrix} = \prod_{j=1}^{M} \begin{pmatrix} \frac{z-Y_j}{z-Y_j^*} & \phi_j \\ \phi_j^* \frac{z-Y_j}{z-Y_j^*} & 1 \end{pmatrix} \tag{6.24}$$

with j increasing from left to right. Ultimately, θ is back-transformed to a Nevanlinna interpolant via the inverse Mobius transform h^{-1}:

$$\mathcal{N}\mathcal{G}(z) = h^{-1}[\theta(z)] = \frac{i[1+\theta(z)]}{1-\theta(z)} \tag{6.25}$$

The comparison between MaxEnt and Nevanlinna analytical continuation is demonstrated in Section 8.3 and Figure 8.7.

6.4 Thermodynamic quantities

For a conserving approximation, we employ a Φ-functional denoted as $\Phi[G]$, which includes all connected closed skeleton diagrams related to the Green's function G. This functional is utilized to represent the grand potential as follows [94]

$$\Omega = \Phi - \mathrm{Tr}\{\ln G^{-1}\} - \mathrm{Tr}\{\Sigma G\} \tag{6.26}$$

where the symbol Tr contains summations over crystal momentum ($1/N_k \sum_{\mathbf{k}}$), Matsubara frequency ($1/\beta \sum_n$), and spin-orbital indices (i, σ). The Luttinger-Ward functional $\Phi[G]$ is a functional of G in the form of

$$\Phi[G] = \sum_{m=1}^{\infty} \frac{1}{2m} \mathrm{Tr}\{\{\Sigma^{(m)}[G]G\}\} \tag{6.27}$$

where $\Sigma^{(m)}[G]G$ is the mth order skeleton diagram of the self-energy Σ. It is a functional of interacting Green's function G and bare Coulomb interactions U where the functional dependence of U appears in the expression of skeleton self-energy diagrams $\Sigma^{(m)}$.

The total energy can be obtained using Galitskii-Migdal formula [149–151]

$$E = E_1 + E_2 \tag{6.28}$$

$$E_1 = \int dx \lim_{x' \to x} [-\frac{\nabla^2}{2} + V_{e-n}] G(x, x'; \tau = 0^-) = \mathrm{Tr}\{H_0 \gamma\} \tag{6.29}$$

$$E_2 = \frac{1}{2} \int_0^\beta d\tau \int dx \int dx' \Sigma(x, x'; -\tau) G(x', x; \tau) = \frac{1}{2} Tr\{\Sigma G\} \tag{6.30}$$

Chapter 7

Optical Properties for Real Materials

7.1 Introduction

7.1.1 Experimental techniques

In the field of studying strong correlated materials, a range of experimental techniques have been developed and utilized. Among them, optical spectroscopy stands out as a natural and intuitive approach. Similar to how our eyes perceive light, optical detectors collect and analyze the response of materials to incident light. However, optical spectroscopy allows us to access frequencies and corresponding phenomena that go beyond the limitations of human vision.

Optical spectroscopy is a technique that studies how matter interacts with electromagnetic radiation. It can be used to determine the chemical composition of matter and to determine its physical structure. Optical spectroscopy is a broad term that encompasses various techniques such as absorption, emission, and scattering spectroscopy. One of the advantages of optical spectroscopy is its inherent precision, which makes it suitable for monitoring changes in correlated materials. In contrast to other methods like photoemission spectroscopy or X-ray experiments, which rely on relative measurements, optical spectroscopy provides results in greater precision, making it easier to track the evolution of the system accurately.

In summary, optical spectroscopy offers a convenient and precise means of studying

correlated materials. By utilizing this technique, researchers can explore the intricate behavior of these materials under different circumstances, gaining valuable insights into their fundamental properties and potential applications.

7.1.2 Theories

Initially, in the realm of strongly correlated electrons, efforts were made to calculate the optical conductivity within the Dynamical Mean-Field Theory (DMFT) framework. The pioneering work by Pruschke et al. [152] and Jarrell et al. [153] focused on the optical responses of the Hubbard model. Building upon this foundation, Rozenberg et al. [154, 155] conducted significant research investigating the various optical behaviors exhibited by the Hubbard model across its phase diagram while also incorporating experimental observations from V_2O_3.

Expanding beyond the realm of idealized models, researchers Blümer [156] and Blümer and van Dongen [157] tackled the challenge of calculating optical conductivity within the more realistic framework of LDA+DMFT for systems with degenerate orbitals. The pioneering work of Pálsson [158] introduced a more comprehensive approach for studying thermo-electricity within this context, broadening the understanding of correlated materials. Presenting an alternative technique, Oudovenko et al. [159] proposed a method that involved diagonalizing the interacting system, allowing for the analytical evaluation of certain integrals due to the "non-interacting" form of the Green's function.

However, due to the frequency-dependent nature of the self-energy, this diagonalization procedure had to be performed individually for each momentum and frequency, involving both left and right eigenvectors. As a consequence, this approach could become computationally expensive. Additionally, it is worth noting that this technique has so far only been employed in LDA+DMFT calculations that made use of approximate impurity solvers, which introduces further nuances and limitations to the analysis.

Overall, the body of literature reviewed highlights the evolution of optical conductivity calculations within the DMFT framework. From its initial applications to the Hubbard model to more realistic scenarios with degenerate orbitals, researchers relentlessly pursued a deeper understanding of correlated materials' optical responses, incorporating experimental data and exploring alternative techniques. While advances have been made, challenges such as the computationally intensive nature of certain methods and

the need for accurate impurity solvers still exist, motivating further investigations in this field.

7.2 Current operator

7.2.1 Generic form of the current operator

The Hamiltonian for the system is taken to have the form

$$H = H_0 + H' \tag{7.1}$$

where H_0 contains all the possible interactions in the solid except the interaction with the electromagnetic field and the term H' contains the interaction between the total electric field and the particles of the system.

The effect of an electromagnetic field on particles is to shift their moments by $-e\mathbf{A}(\mathbf{r})$, where $\mathbf{A}(\mathbf{r})$ is the vector potential[160]. Here we choose the gauge $\nabla \cdot \mathbf{A} = 0$ so that the scalar potential is zero. The resulting change in the particle energy is the product of its velocity (i.e. the current) by the change in momentum. For a collection of particles,

$$\delta H' = \int d\mathbf{r}\mathbf{j}(\mathbf{r}) \cdot \delta\mathbf{A}(\mathbf{r}) \tag{7.2}$$

$$\Rightarrow \mathbf{j}(\mathbf{r}) = -\frac{\delta H}{\delta \mathbf{A}(\mathbf{r})} \tag{7.3}$$

where $\mathbf{j}(\mathbf{r})$ is an electric current. If we can express the Hamiltonian in terms of creation and annihilation operators, then we can obtain a definition of the current operator.

In a solid, the operator $\mathbf{p}$ appears only in the kinetic energy, namely $\mathbf{p} = -i\hbar\nabla$:

$$\begin{aligned} H' =& \int d\mathbf{r} \sum_\sigma c^\dagger_{\mathbf{r}\sigma} \frac{[\mathbf{p} - e\mathbf{A}(\mathbf{r})]^2}{2m} c_{\mathbf{r}\sigma} - \int d\mathbf{r} \sum_\sigma c^\dagger_{\mathbf{r}\sigma} \frac{\mathbf{p}^2}{2m} c_{\mathbf{r}\sigma} \\ =& \frac{1}{2m} \int d\mathbf{r} \sum_\sigma c^\dagger_{\mathbf{r}\sigma} [i\hbar e \nabla_{\mathbf{r}} \cdot \mathbf{A}(\mathbf{r}) + i\hbar e \mathbf{A}(\mathbf{r}) \cdot \nabla_{\mathbf{r}} + e^2 \mathbf{A}^2(\mathbf{r})] c_{\mathbf{r}\sigma} \end{aligned} \tag{7.4}$$

By using the integration by parts

$$\int d\mathbf{r} c^\dagger_{\mathbf{r}\sigma} \nabla_{\mathbf{r}} \cdot \mathbf{A}(\mathbf{r}) c_{\mathbf{r}\sigma} = -\int d\mathbf{r} \mathbf{A}(\mathbf{r}) \cdot (\nabla_{\mathbf{r}} c^\dagger_{\mathbf{r}\sigma}) c_{\mathbf{r}\sigma}, \tag{7.5}$$

we can obtain that

$$H' = -\int d\mathbf{r} \mathbf{j}(\mathbf{r}) \cdot \mathbf{A}(\mathbf{r}) \tag{7.6}$$

$$\mathbf{j}(\mathbf{r}) = \mathbf{j}^p(\mathbf{r}) + \mathbf{j}^d(\mathbf{r}) \tag{7.7}$$

$$\mathbf{j}^p(\mathbf{r}) = \frac{i\hbar e}{2m} \sum_\sigma \left[(\nabla_{\mathbf{r}} c^\dagger_{\mathbf{r}\sigma}) c_{\mathbf{r}\sigma} - c^\dagger_{\mathbf{r}\sigma} (\nabla_{\mathbf{r}} c_{\mathbf{r}\sigma}) \right] \tag{7.8}$$

$$\mathbf{j}^d(\mathbf{r}) = -\frac{e^2}{2m} \sum_\sigma \mathbf{A}(\mathbf{r}) c^\dagger_{\mathbf{r}\sigma} c_{\mathbf{r}\sigma} \tag{7.9}$$

where $\mathbf{j}^p(\mathbf{r})$ is the paramagnetic current, and $\mathbf{j}^d(\mathbf{r})$ is the diamagnetic current.

7.2.2 Current density in the plane wave basis

In order to construct a basis on which we can expand a many-particle state, we start by choosing a complete basis for the one-particle state $\phi_\alpha(1)$, where $1 \equiv (\mathbf{r}_1, \sigma_1)$. In a solid, a convenient basis is formed by the plane waves

$$\phi_{\mathbf{k}\sigma}(1) \equiv \frac{\delta_{\sigma\sigma_1}}{\sqrt{\mathcal{V}}} e^{i\mathbf{k}\cdot\mathbf{r}_1} \tag{7.10}$$

which satisfy

$$\langle \mathbf{k}\sigma | \mathbf{k}\sigma' \rangle = \delta_{\sigma\sigma'} \delta_{\mathbf{k}\mathbf{k}'} \tag{7.11}$$

$$\sum_{\mathbf{k}\sigma} |\mathbf{k}\sigma\rangle\langle\mathbf{k}\sigma| = \mathbf{1} \tag{7.12}$$

Then we are looking for a relation between $c^\dagger_{\mathbf{k}}$ and $c^\dagger_{\mathbf{r}}$ (here we ignore other quantum numbers such as σ temporarily for simplification) in the form of

$$c^\dagger_{\mathbf{k}} = \int d\mathbf{r} U_{\mathbf{k}\mathbf{r}} c^\dagger_{\mathbf{r}} \tag{7.13}$$

In the plane wave basis sets, act $c_{\mathbf{k}}^{\dagger}$ on the vacuum state $|0\rangle$ on the right and on the state $\langle \mathbf{r}_1|$ on the left:

$$\langle \mathbf{r}_1|c_{\mathbf{k}}^{\dagger}|0\rangle = \psi_{\mathbf{k}}(\mathbf{r}_1) = \int d\mathbf{r} U_{\mathbf{kr}} \langle \mathbf{r}_1|c_{\mathbf{r}}^{\dagger}|0\rangle = U_{\mathbf{kr}_1} \tag{7.14}$$

So

$$c_{\mathbf{k}}^{\dagger} = \frac{1}{\sqrt{\mathcal{V}}} \int d\mathbf{r} e^{i\mathbf{k}\cdot\mathbf{r}} c_r^{\dagger} \tag{7.15}$$

Similarly

$$c_{\mathbf{k}} = \frac{1}{\sqrt{\mathcal{V}}} \int d\mathbf{r} e^{-i\mathbf{k}\cdot\mathbf{r}} c_r \tag{7.16}$$

$$c_{\mathbf{r}}^{\dagger} = \frac{1}{\sqrt{\mathcal{V}}} \sum_{\mathbf{k}} e^{-i\mathbf{k}\cdot\mathbf{r}} c_{\mathbf{k}}^{\dagger} \tag{7.17}$$

$$c_{\mathbf{r}} = \frac{1}{\sqrt{\mathcal{V}}} \sum_{\mathbf{k}} e^{i\mathbf{k}\cdot\mathbf{r}} c_{\mathbf{k}} \tag{7.18}$$

Actually, the same argument can be extended to arbitrary one-particle basis:

$$c_{\mathbf{r}}^{\dagger} = \sum_{\alpha} \phi_{\alpha}^{*}(\mathbf{r}) c_{\alpha}^{\dagger} \tag{7.19}$$

$$c_{\alpha}^{\dagger} = \int d\mathbf{r} \phi_{\alpha}(\mathbf{r}) c_{\mathbf{r}}^{\dagger} \tag{7.20}$$

where α represents any kind of basis and $\phi_{\alpha}(\mathbf{r})$ is the corresponding basis function.

The Fourier transform of $\mathbf{j}(\mathbf{r})$ is easily evaluated by using the expression of the field operators in the plane-wave basis:

$$\begin{aligned}
\mathbf{j}^p(\mathbf{q}) =& \int d\mathbf{r} e^{-i\mathbf{q}\cdot\mathbf{r}} \frac{i\hbar e}{2m} \sum_{\sigma} \frac{1}{\mathcal{V}} \sum_{\mathbf{k}\mathbf{k}'} c_{\mathbf{k}\sigma}^{\dagger} c_{\mathbf{k}'\sigma} \left[(\nabla_{\mathbf{r}} e^{-i\mathbf{k}\cdot\mathbf{r}}) e^{i\mathbf{k}'\cdot\mathbf{r}} - e^{-i\mathbf{k}\cdot\mathbf{r}} (\nabla_{\mathbf{r}} e^{i\mathbf{k}'\cdot\mathbf{r}}) \right] \\
=& \frac{\hbar e}{2m} \sum_{\sigma} \frac{1}{\mathcal{V}} \sum_{\mathbf{k}\mathbf{k}'} (\mathbf{k}+\mathbf{k}') c_{\mathbf{k}\sigma}^{\dagger} c_{\mathbf{k}'\sigma} \int d\mathbf{r} e^{-i\mathbf{q}\cdot\mathbf{r}} e^{-i(\mathbf{k}-\mathbf{k}')\cdot\mathbf{r}} \\
=& \frac{\hbar e}{2m} \sum_{\mathbf{k}\sigma} (2\mathbf{k}+\mathbf{q}) c_{\mathbf{k}\sigma}^{\dagger} c_{\mathbf{k}+\mathbf{q},\sigma}
\end{aligned} \tag{7.21}$$

$$
\begin{aligned}
\mathbf{j}^d(\mathbf{q}) &= \int d\mathbf{r} e^{-i\mathbf{q}\cdot\mathbf{r}}(-\frac{e^2}{mc})\sum_{\sigma}\mathbf{A}(\mathbf{r})\frac{1}{\mathcal{V}}\sum_{\mathbf{k}\mathbf{k}'}c^{\dagger}_{\mathbf{k}\sigma}c_{\mathbf{k}'\sigma}e^{-\mathbf{k}\cdot\mathbf{r}}e^{i\mathbf{k}'\cdot\mathbf{r}} \\
&= -\frac{e^2}{mc\mathcal{V}}\sum_{\mathbf{k}\mathbf{k}'\sigma}c^{\dagger}_{\mathbf{k}\sigma}c_{\mathbf{k}'\sigma}\int d\mathbf{r}\mathbf{A}(\mathbf{r})e^{-i(\mathbf{q}+\mathbf{k}-\mathbf{k}')\cdot\mathbf{r}} \\
&= -\frac{e^2}{mc\mathcal{V}}\sum_{\mathbf{k}\mathbf{k}'\sigma}\mathbf{A}(\mathbf{k}-\mathbf{k}')c^{\dagger}_{\mathbf{k}\sigma}c_{\mathbf{k}+\mathbf{q},\sigma}
\end{aligned}
\tag{7.22}
$$

7.2.3 Current operator in the Bloch waves

In our work, the one-particle basis we are using is Gaussian-based Block waves $\phi_i^{\mathbf{k}}(\mathbf{r})$:

$$
\phi_i^{\mathbf{k}}(\mathbf{r}) = \sum_{\mathbf{R}}\phi_i^{\mathbf{R}}(\mathbf{r})e^{i\mathbf{k}\cdot\mathbf{R}} \tag{7.23}
$$

where

$\mathbf{R}$: unit cell index,

i: localized atomic orbital index,

$\mathbf{k}$: momentum index in the first Brillouin zone.

$\phi_i^{\mathbf{R}}(\mathbf{r})$ are atomic-centered Gaussian functions shifted to the unit cell with label $\mathbf{R}$, i.e. $\phi_i^{\mathbf{R}}(\mathbf{r}) = \varphi_i(\mathbf{r}-\mathbf{R})$ in which $\varphi_i(\mathbf{r})$ are these functions in the central unit cell.

For two Bloch basis functions,

$$
\int_{\mathcal{R}^3} d\mathbf{r}\phi_i^{\mathbf{k}*}(\mathbf{r})\phi_j^{\mathbf{k}'}(\mathbf{r}) = N\delta_{\mathbf{k}\mathbf{k}'}\sum_{\mathbf{R}}e^{i\mathbf{k}'\cdot\mathbf{R}}\int_{\mathcal{R}^3} d\mathbf{r}\phi_i^0(\mathbf{r})\phi_j^{\mathbf{R}}(\mathbf{r}) \tag{7.24}
$$

The Gaussian-type Bloch waves are orthogonal in $\mathbf{k}$.

Using the change of basis in Eq.7.19, we can express the creation and annihilation operator in the Bloch waves:

$$
c^{\dagger}_{\mathbf{r}} = \sum_{\alpha}\psi^*_{\alpha}(\mathbf{r})c^{\dagger}_{\alpha} = \sum_{\mathbf{k},\mathbf{R}}\phi_i^{\mathbf{R}*}(\mathbf{r})e^{-i\mathbf{k}\cdot\mathbf{R}}c^{\dagger}_{\mathbf{k}} \tag{7.25}
$$

$$
c_{\mathbf{r}} = \sum_{\mathbf{k},\mathbf{R}}\phi_i^{\mathbf{R}}(\mathbf{r})e^{i\mathbf{k}\cdot\mathbf{R}}c_{\mathbf{k}} \tag{7.26}
$$

The paramagnetic current can be expressed as

$$\begin{aligned}\mathbf{j}^p(\mathbf{q}) =& \frac{i\hbar e}{2m}\sum_{ij,\mathbf{k}\mathbf{k}',\sigma} c_{i\sigma}^{\mathbf{k}\dagger}c_{j\sigma}^{\mathbf{k}'}\int d\mathbf{r}e^{-i\mathbf{q}\cdot\mathbf{r}} \\ &\times\left[\phi_i^{\mathbf{k}*}(\mathbf{r})\nabla_{\mathbf{r}}\phi_j^{\mathbf{k}'}(\mathbf{r}) - \phi_j^{\mathbf{k}'}(\mathbf{r})\nabla_{\mathbf{r}}\phi_i^{\mathbf{k}*}(\mathbf{r})\right]\end{aligned} \tag{7.27}$$

7.3 Linear Response Theory

7.3.1 Kubo formula for the optical conductivity

Kubo formulas are applied to the correlation function that describes the linear response, which means that the perturbation is weak and signal is directly proportional to the intensity of the external perturbation.

In electrical conduction, the conductivity σ can be expressed as the proportionality of how the induced current J reponsed linearly to the electric field E in the solid[161]:

$$J_\alpha(\mathbf{r},t) = \sum_\beta \sigma_{\alpha\beta}(\mathbf{q},\omega)E_\beta(\mathbf{r},t) \tag{7.28}$$

$$E_\alpha(\mathbf{r},t) = \Xi_\alpha e^{i\mathbf{q}\cdot\mathbf{r}-i\omega t} \tag{7.29}$$

where the indices α,β are spatial coordinates, $\mathbf{q}$ and ω are the moment and frequency of the external field.

The Kubo formula is derived assuming that the system is linear and perturbations at different frequencies act indepently. From the derivation above:

$$H' = -\sum_\alpha \int d^3r j_\alpha(\mathbf{r})A_\alpha(\mathbf{r},t) \tag{7.30}$$

$$A_\alpha(\mathbf{r},t) = -\frac{i}{\omega}E_\alpha(\mathbf{r},t) \tag{7.31}$$

where A is the vector potential, j is the current operator and the relation Eq.7.31 is based on the choice of the gauge as $\nabla\cdot\mathbf{A}=0$.

According to the definition of the current operator in Eq.7.7, Eq.7.8 and Eq.7.9, The measured value of the current, which is the average value for the velocity of the particles

in the system, has the form of

$$\begin{aligned}\mathbf{J}(\mathbf{r},t) &= \langle \mathbf{j}(\mathbf{r},t)\rangle = \langle \mathbf{j}^p(\mathbf{r},t)\rangle + \langle \mathbf{j}^d(\mathbf{r},t)\rangle \\ &= \langle \mathbf{j}^p(\mathbf{r},t)\rangle - \frac{e^2}{2m}\langle \sum_\sigma c^\dagger_{\mathbf{r}\sigma} c_{\mathbf{r}\sigma}\rangle \mathbf{A}(\mathbf{r}) \\ &= \langle \mathbf{j}^p(\mathbf{r},t)\rangle + i\frac{n_0 e^2}{m\omega}\mathbf{E}(\mathbf{r},t)\end{aligned} \tag{7.32}$$

The second term in the current is proportional to the electric field and the first term is given by the expectation value of the current operator. These two terms can be written in the form of vectors:

$$\mathbf{J} = \mathbf{J}^{(1)} + \mathbf{J}^{(2)} \tag{7.33}$$

$$\mathbf{J}^{(1)} = \frac{i n_0 e^2}{m\omega}\mathbf{E}(\mathbf{r},t) \tag{7.34}$$

$$\mathbf{J}^{(2)} = \langle \mathbf{j}^p(\mathbf{r},t)\rangle \tag{7.35}$$

When we use the phrase "the current operator" later, we mean "the paramagnetic current operator".

First consider the case at zero temperature. Then the expectation value of the current operator in the interaction representation is

$$J^{(2)}_\alpha = \langle \Psi_0 | S^\dagger(t,-\infty) j^p_\alpha(\mathbf{r},t) S(t,-\infty)|\Psi_0\rangle \tag{7.36}$$

where $|\Psi_0\rangle$ is the groud state of the many-body Hamiltionian H_0 and

$$S(t,-\infty) = T\exp\left[-i\int_{-\infty}^{t} dt' H'(t')\right] \tag{7.37}$$

Only the terms linear in the electric field E_α are desired, which requires us to only keep terms linear in H':

$$J^{(2)}_\alpha = \langle \Psi_0 | \left[1 + i\int_{-\infty}^{t} dt' H'(t')\right] j^p_\alpha(\mathbf{r},t) \left[1 - i\int_{-\infty}^{t} dt' H'(t')\right] |\Psi_0\rangle \tag{7.38}$$

$$= \langle \Psi_0 | j^p_\alpha(\mathbf{r},t) - i\int_{-\infty}^{t} dt' \left[j^p_\alpha(\mathbf{r},t) H'(t') - H'(t') j^p_\alpha(\mathbf{r},t)\right] |\Psi_0\rangle \tag{7.39}$$

Assume that there is no current in the solid in the absence of the electric field or something equivalent:

$$\langle \Psi_0 | j^p_\alpha(\mathbf{r}, t) | \Psi_0 \rangle = 0 \tag{7.40}$$

So

$$J^{(2)}_\alpha = -i \int_{-\infty}^{t} dt' \langle \Psi_0 | \left[j^p_\alpha(\mathbf{r}, t), H'(t') \right] | \Psi_0 \rangle \tag{7.41}$$

where

$$\begin{aligned} &[j^p_\alpha(\mathbf{r}, t), H'(t')] \\ &= \frac{i}{\omega} E_\beta(\mathbf{r}, t) e^{-i\mathbf{q}\cdot\mathbf{r}} e^{i\omega(t-t')} \left[j^p_\alpha(\mathbf{r}, t), j_\beta(\mathbf{q}, t') \right] \end{aligned} \tag{7.42}$$

and

$$j_\beta(\mathbf{q}, t') = j^p_\beta(\mathbf{q}, t') + j^d_\beta(\mathbf{q}, t') \tag{7.43}$$

Since we only consider the terms that are linear with the electric field E, and j^d contains an external dependence on E, we can ignore j^d term here.

Then average over the space variable $\mathbf{r}$ to eliminate atomic fluctuations:

$$\frac{1}{\mathcal{V}} \int d^3 r e^{-i\mathbf{q}\cdot\mathbf{r}} j^p_\alpha(\mathbf{r}, t) = j^p_\alpha(-\mathbf{q}, t) = j^{p\dagger}_\alpha(\mathbf{q}, t) \tag{7.44}$$

So the Kubo formula for the conductivity is

$$\sigma_{\alpha\beta}(\mathbf{q}, \omega) = \frac{1}{\omega \mathcal{V}} \int_{-\infty}^{t} dt' e^{i\omega(t-t')} \langle \Psi_0 | \left[j^{p\dagger}_\alpha(\mathbf{q}, t), j^p_\beta(\mathbf{q}, t') \right] | \Psi_0 \rangle + i \frac{n_0 e^2}{m\omega} \delta_{\alpha\beta} \tag{7.45}$$

$$= \frac{1}{\omega \mathcal{V}} \int_{0}^{\infty} dt e^{i\omega t} \langle \Psi_0 | \left[j^{p\dagger}_\alpha(\mathbf{q}, t), j^p_\beta(\mathbf{q}, 0) \right] | \Psi_0 \rangle + i \frac{n_0 e^2}{m\omega} \delta_{\alpha\beta} \tag{7.46}$$

where Eq.7.46 is obtained from Eq.7.45 by making the variable change $t - t' \to t$.

The above derivation can be easily extended to finite temperature case by interpreting the bracket as a thermodynamic average.

7.3.2 Current-current correlation function

The Kubo formulas contain a retared, two particle correlation function, which is called the current-current correlation function:

$$\Pi_{\alpha\beta}(\mathbf{q}, t-t') = -\frac{i}{\mathcal{V}}\Theta(t-t')\langle\Psi_0|\left[j_\alpha^\dagger(\mathbf{q},t), j_\beta(\mathbf{q},t')\right]|\Psi_0\rangle \tag{7.47}$$

Using its Fourier transform, we can express the conductivity in terms of the current-current correlation function

$$\sigma_{\alpha\beta}(\mathbf{q},\omega) = \frac{i}{\omega}\left[\Pi_{\alpha\beta}(\mathbf{q},\omega) + \frac{n_0 e^2}{m}\delta_{\alpha\beta}\right] \tag{7.48}$$

It is usually easiest to calculate the retarded correlation function in the Matsubara formalism. We can quickly generalize Eq.7.47 to imaginary time, by replacing $i\langle[A(1), B(2)]\rangle \to \langle TA(1)B(2)\rangle$:

$$\Pi_{\alpha\beta}(\mathbf{q},\tau) = -\frac{1}{\mathcal{V}}\langle T_\tau j_\alpha^\dagger(\mathbf{q},\tau) j_\beta(\mathbf{q},0)\rangle \tag{7.49}$$

$$\Pi_{\alpha\beta}(\mathbf{q}, i\omega_n) = \int_0^\beta d\tau e^{i\omega_n\tau}\Pi_{\alpha\beta}(\mathbf{q},\tau) \tag{7.50}$$

The current operator contains a product of one creation and one destruction operator, so the correlation function Eq.7.49 contains at least four such operators. Substitute the expression for the current operator Eq.7.21 into the correlation function in terms of the plane wave basis:

$$\Pi(\mathbf{q},\tau) = -\frac{\hbar^2 e^2}{m^2\mathcal{V}}\sum_{\mathbf{k}\mathbf{k}'\sigma\sigma'}(2\mathbf{k}+\mathbf{q})\cdot(2\mathbf{k}'+\mathbf{q})\langle T_\tau c^\dagger_{\mathbf{k}+\mathbf{q},\sigma}(\tau)c_{\mathbf{k}\sigma}(\tau)c^\dagger_{\mathbf{k}'\sigma'}(0)c_{\mathbf{k}'+\mathbf{q},\sigma'}(0)\rangle \tag{7.51}$$

$$\begin{aligned}\Pi(\mathbf{q}, i\omega_n) = -\frac{\hbar^2 e^2}{m^2\mathcal{V}}\int_0^\beta d\tau e^{i\omega_n\tau}\sum_{\mathbf{k}\mathbf{k}'\sigma\sigma'}&(2\mathbf{k}+\mathbf{q})\cdot(2\mathbf{k}'+\mathbf{q})\\ &\times\langle T_\tau c^\dagger_{\mathbf{k}+\mathbf{q},\sigma}(\tau)c_{\mathbf{k}\sigma}(\tau)c^\dagger_{\mathbf{k}'\sigma'}(0)c_{\mathbf{k}'+\mathbf{q},\sigma'}(0)\rangle\end{aligned} \tag{7.52}$$

Here we only consider the first order contribution:

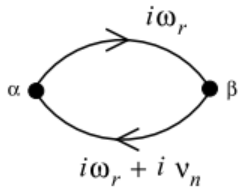

Figure 7.1: The first contribution to the current-current correlation function.

$$\begin{aligned}
\Pi^{(1)}(\mathbf{q}, i\omega_n) = &-\frac{\hbar^2 e^2}{m^2 \mathcal{V}} \int_0^\beta d\tau e^{i\omega_n \tau} \sum_{\mathbf{k}\mathbf{k}'\sigma\sigma'} (2\mathbf{k}+\mathbf{q}) \cdot (2\mathbf{k}'+\mathbf{q}) \\
&\times [T_\tau e^{\tau H_0} \langle c^\dagger_{\mathbf{k}+\mathbf{q},\sigma} c_{\mathbf{k}\sigma} \rangle e^{-\tau H_0} \langle c^\dagger_{\mathbf{k}'\sigma'} c_{\mathbf{k}'+\mathbf{q},\sigma'} \rangle \\
&- \delta_{\mathbf{k}=\mathbf{k}'} \delta_{\sigma=\sigma'} G(\mathbf{k}+\mathbf{q}, \tau) G(\mathbf{k}, -\tau)] \\
= &\frac{2\hbar^2 e^2}{m^2 \mathcal{V}} \int_0^\beta d\tau e^{i\omega_n \tau} \sum_{\mathbf{k}} (2\mathbf{k}+\mathbf{q})^2 G(\mathbf{k}+\mathbf{q}, \tau) G(\mathbf{k}, -\tau) \\
&- \frac{\hbar^2 e^2}{m^2 \mathcal{V}} \sum_{\mathbf{k}\mathbf{k}'\sigma\sigma'} (2\mathbf{k}+\mathbf{q}) \cdot (2\mathbf{k}'+\mathbf{q}) \langle c^\dagger_{\mathbf{k}+\mathbf{q},\sigma} c_{\mathbf{k}\sigma} \rangle \langle c^\dagger_{\mathbf{k}'\sigma'} c_{\mathbf{k}'+\mathbf{q},\sigma'} \rangle \int_0^\beta d\tau e^{i\omega_n \tau} \\
= &\frac{2\hbar^2 e^2}{m^2 \mathcal{V}} \int_0^\beta d\tau e^{i\omega_n \tau} \sum_{\mathbf{k}} (2\mathbf{k}+\mathbf{q})^2 G(\mathbf{k}+\mathbf{q}, \tau) G(\mathbf{k}, -\tau) \\
&- \frac{\hbar^2 e^2}{m^2 \mathcal{V}} \beta \delta_{\omega_n} \sum_{\mathbf{k}\mathbf{k}'\sigma\sigma'} (2\mathbf{k}+\mathbf{q}) \cdot (2\mathbf{k}'+\mathbf{q}) \langle c^\dagger_{\mathbf{k}+\mathbf{q},\sigma} c_{\mathbf{k}\sigma} \rangle \langle c^\dagger_{\mathbf{k}'\sigma'} c_{\mathbf{k}'+\mathbf{q},\sigma'} \rangle
\end{aligned} \tag{7.53}$$

Since $[H_0, n] = 0$ and $\langle c^\dagger_{\mathbf{k}+\mathbf{q},\sigma} c_{\mathbf{k}\sigma} \rangle$, $\langle c^\dagger_{\mathbf{k}'\sigma'} c_{\mathbf{k}'+\mathbf{q},\sigma'} \rangle$ is τ-independent, the second term of Eq.7.53 is zero unless $\omega_n = 0$.

The Matsubara function can be evaluated by using the diagrammatic techniques shown in Fig.7.1[162]:

$$\Pi^{(1)}_{\alpha\beta}(\mathbf{q}, i\nu_n) = 2\frac{\hbar^2 e^2}{m^2 \mathcal{V}} \frac{1}{\beta} \sum_{\mathbf{k}, i\omega_r} (2k_\alpha + q_\alpha)(2k_\beta + q_\beta) G(\mathbf{k}+\mathbf{q}, i\omega_r + i\nu_n) G(\mathbf{k}, i\omega_r) \tag{7.54}$$

where an extra minus sign derives from the fermion loop and the prefactor of 2 derives from the summation of the spins.

7.3.3 Correlation function in Bloch waves

In terms of the Bloch wave basis set, substitute Eq.7.27 into the definition of current-current correlation Eq.7.49:

$$\begin{aligned}\Pi(\mathbf{q},\tau)_{\alpha\beta} =& \frac{\hbar^2 e^2}{2m^2\mathcal{V}} \sum_{ijkl} \sum_{\mathbf{k}\mathbf{k}'\mathbf{p}\mathbf{p}'} \langle c_i^{\mathbf{k}\dagger}(\tau) c_j^{\mathbf{k}'}(\tau) c_k^{\mathbf{p}\dagger}(0) c_l^{\mathbf{p}'}(0)\rangle \int d^3\mathbf{r} d^3\mathbf{r}' e^{i\mathbf{q}\cdot(\mathbf{r}-\mathbf{r}')} \\ & \times \left[\phi_i^{\mathbf{k}*}(\mathbf{r})\nabla_{\mathbf{r}}\phi_j^{\mathbf{k}'}(\mathbf{r}) - \phi_j^{\mathbf{k}'}(\mathbf{r})\nabla_{\mathbf{r}}\phi_i^{\mathbf{k}*}(\mathbf{r})\right]_\alpha \\ & \times \left[\phi_k^{\mathbf{p}*}(\mathbf{r}')\nabla_{\mathbf{r}'}\phi_l^{\mathbf{p}'}(\mathbf{r}') - \phi_l^{\mathbf{p}'}(\mathbf{r}')\nabla_{\mathbf{r}'}\phi_k^{\mathbf{p}*}(\mathbf{r}')\right]_\beta \end{aligned} \tag{7.55}$$

Similarly, we only consider the first contribution here:

$$\begin{aligned}\Pi^{(1)}_{\alpha\beta}(\mathbf{q},\tau) =& \frac{\hbar^2 e^2}{2m^2\mathcal{V}} \sum_{ijkl} \sum_{\mathbf{k}\mathbf{k}'} G_{il}^{\mathbf{k}}(\tau) G_{jk}^{\mathbf{k}'}(-\tau) \int d^3\mathbf{r} d^3\mathbf{r}' e^{i\mathbf{q}\cdot(\mathbf{r}-\mathbf{r}')} \\ & \times \left[\phi_i^{\mathbf{k}*}(\mathbf{r})\nabla_{\mathbf{r}}\phi_j^{\mathbf{k}'}(\mathbf{r}) - \phi_j^{\mathbf{k}'}(\mathbf{r})\nabla_{\mathbf{r}}\phi_i^{\mathbf{k}*}(\mathbf{r})\right]_\alpha \\ & \times \left[\phi_k^{\mathbf{k}'*}(\mathbf{r}')\nabla_{\mathbf{r}'}\phi_l^{\mathbf{k}}(\mathbf{r}') - \phi_l^{\mathbf{k}}(\mathbf{r}')\nabla_{\mathbf{r}'}\phi_k^{\mathbf{k}'*}(\mathbf{r}')\right]_\beta \end{aligned} \tag{7.56}$$

In discussing the direct transitions, we need not be concerned with the momentum of the photon because it is very small in comparison to Brillouin zone. For typical optical wavelengthes from 200nm to 800nm, the corresponding momentum range in $10^{-28} \sim 10^{-27}$kg·m/s. While for a typical lattice constant around 0.1nm, the typical dimension across the Brillouin zone is 10^{-24}kg·m/s. Thus, typical direct optical interband processes excite an electron from a valence to a conduction band without a significant change in the wave vector[163].

Next, we will show why the momentum matrix elements coupling two Bloch states for a perfect crystal are diagonal in $\mathbf{k}$ and conserve crystal momentum and thus the optical transitions between them are direct transitions.

Write the Bloch wave basis set in the form of the definition of the Bloch functions:

$$\phi_i^{\mathbf{k}}(\mathbf{r}) = e^{i\mathbf{k}\cdot\mathbf{r}} u_i^{\mathbf{k}}(\mathbf{r}) \tag{7.57}$$

where from the definition of $\phi_i^{\mathbf{k}}(\mathbf{r})$ in Eq.7.23,

$$u_i^{\mathbf{k}}(\mathbf{r}) = \sum_{\mathbf{R}} \phi_i(\mathbf{r}-\mathbf{R}) e^{-i\mathbf{k}\cdot(\mathbf{r}-\mathbf{R})} \tag{7.58}$$

and it is periodic under the translation $\mathbf{r} \to \mathbf{r} + \mathbf{R}_n$, where $\mathbf{R}_n$ is any lattice vector.

So the momentum matrix element between two Bloch states is

$$\begin{aligned} \langle j\mathbf{k}'|\mathbf{p}|i\mathbf{k}\rangle &= \int_{\mathcal{R}^3} d^3\mathbf{r} e^{-i\mathbf{k}'\cdot\mathbf{r}} u_j^{\mathbf{k}'*}(\mathbf{r})(\frac{\hbar}{i}\nabla) e^{i\mathbf{k}\cdot\mathbf{r}} u_i^{\mathbf{k}}(\mathbf{r}) \\ &= \int_{\mathcal{R}^3} d^3\mathbf{r} e^{-i\mathbf{k}'\cdot\mathbf{r}} u_j^{\mathbf{k}'*}(\mathbf{r}) e^{i\mathbf{k}\cdot\mathbf{r}} (\hbar\mathbf{k} + \frac{\hbar}{i}\nabla) u_i^{\mathbf{k}}(\mathbf{r}) \end{aligned} \tag{7.59}$$

where the first term is obtained from Eq.7.24

$$\begin{aligned} &\hbar\mathbf{k} \int_{\mathcal{R}^3} d^3\mathbf{r} e^{-i\mathbf{k}'\cdot\mathbf{r}} u_j^{\mathbf{k}'*}(\mathbf{r}) e^{i\mathbf{k}\cdot\mathbf{r}} u_i^{\mathbf{k}}(\mathbf{r}) \\ =&\hbar\mathbf{k} N \delta_{\mathbf{k}\mathbf{k}'} \sum_{\mathbf{R}} e^{i\mathbf{k}'\cdot\mathbf{R}} \int_{\mathcal{R}^3} d\mathbf{r} \phi_i^{0*}(\mathbf{r}) \phi_j^{\mathbf{R}}(\mathbf{r}) \end{aligned} \tag{7.60}$$

which is diagonal in momentum $\mathbf{k}$. The remaining term in Eq.7.59 is

$$\int_{\mathcal{R}^3} d^3\mathbf{r} e^{i(\mathbf{k}-\mathbf{k}')\cdot\mathbf{r}} \frac{\hbar}{i} u_j^{\mathbf{k}'*}(\mathbf{r}) \nabla u_i^{\mathbf{k}}(\mathbf{r}) \tag{7.61}$$

The function $u_j^{\mathbf{k}'*}(\mathbf{r})\nabla u_i^{\mathbf{k}}(\mathbf{r})$ is periodic under the transition $\mathbf{r} \to \mathbf{r} + \mathbf{R}_n$, and any spatially periodic function can be Fourier expanded[163] in terms of the reciprocal lattice vector $\mathbf{G}_m$:

$$\sum_m F_m e^{i\mathbf{G}_m\cdot\mathbf{r}} = \frac{\hbar}{i} u_j^{\mathbf{k}'*}(\mathbf{r}) \nabla u_i^{\mathbf{k}}(\mathbf{r}) \tag{7.62}$$

Thus the integral in Eq.7.61 can be rewrite in the form of

$$\sum_m \int_{\mathcal{R}^3} e^{i(\mathbf{k}-\mathbf{k}')\cdot\mathbf{r}} F_m e^{i\mathbf{G}_m\cdot\mathbf{r}} \tag{7.63}$$

which vanishes unless

$$\mathbf{k} - \mathbf{k}' + \mathbf{G}_m = 0 \tag{7.64}$$

Since $\mathbf{k}$ and $\mathbf{k}'$ are momentum indices in the first Brillouin zoon according to the defini-

tion of the Bloch wave basis sets in Eq.7.23, The difference between $\mathbf{k}$ and $\mathbf{k}'$ can only be zero, i.e. $\mathbf{G}_m \equiv 0$. Therefore, the optical transitions between two Bloch states are direct transitions, which conserve the momentum during a transition. And according to the discuss above, we can ignore the momentum of the photon, which means $\mathbf{q} = 0$.

Then the first contribution to the current-current correlation function is

$$\begin{aligned}\Pi^{(1)}(\mathbf{q},\tau) =& \frac{\hbar^2 e^2}{2m^2\mathcal{V}} \sum_{ijkl} \sum_{\mathbf{k}\mathbf{k}'} G^{\mathbf{k}}_{il}(\tau) G^{\mathbf{k}'}_{jk}(-\tau) \\ & \times (P^{\mathbf{k}\mathbf{k}'}_{ij} - P^{\mathbf{k}'\mathbf{k}}_{ji})(P^{\mathbf{k}'\mathbf{k}}_{kl} - P^{\mathbf{k}\mathbf{k}'}_{lk})\end{aligned} \tag{7.65}$$

where

$$\begin{aligned}P^{\mathbf{k}\mathbf{k}'}_{ij} =& \int d^3\mathbf{r} \phi^{\mathbf{k}*}_i(\mathbf{r}) \nabla_{\mathbf{r}} \phi^{\mathbf{k}'}_j(\mathbf{r}) \\ =& \sum_{\mathbf{R},\mathbf{R}'} e^{-i\mathbf{k}\cdot\mathbf{R}} e^{i\mathbf{k}'\cdot\mathbf{R}'} \int d^3\mathbf{r} \phi^{\mathbf{R}*}_i(\mathbf{r}) \nabla_{\mathbf{r}} \phi^{\mathbf{R}'}_j(\mathbf{r}) \\ & (\tilde{\mathbf{R}} = \mathbf{R}' - \mathbf{R}) \\ =& \sum_{\mathbf{R},\tilde{\mathbf{R}}} e^{-i(\mathbf{k}-\mathbf{k}')\cdot\mathbf{R}} e^{i\mathbf{k}'\cdot\tilde{\mathbf{R}}} \int d^3\mathbf{r} \phi^{0*}_i(\mathbf{r}) \nabla_{\mathbf{r}} \phi^{\tilde{\mathbf{R}}}_j(\mathbf{r}) \\ =& N\delta_{\mathbf{k}\mathbf{k}'} \sum_{\mathbf{R}} e^{i\mathbf{k}\cdot\mathbf{R}} \int d^3 \phi^{0*}_i(\mathbf{r}) \nabla_{\mathbf{r}} \phi^{\mathbf{R}}_j(\mathbf{r})\end{aligned} \tag{7.66}$$

which is diagonal in $\mathbf{k}$.

The Mastubara function can be evaluated as

$$\begin{aligned}\Pi^{(1)}_{\alpha\beta}(\mathbf{0}, i\nu_n) =& \frac{\hbar^2 e^2}{2m^2\mathcal{V}} \sum_{ijkl} \sum_{\mathbf{k}\mathbf{k}', i\omega_r} G^{\mathbf{k}}_{il}(i\omega_r + i\nu_n) G^{\mathbf{k}'}_{jk}(i\omega_r) \\ & \times (P^{\mathbf{k}\mathbf{k}'}_{ij} - P^{\mathbf{k}'\mathbf{k}}_{ji})_\alpha (P^{\mathbf{k}'\mathbf{k}}_{kl} - P^{\mathbf{k}\mathbf{k}'}_{lk})_\beta \\ =& \frac{\hbar^2 e^2}{2m^2\mathcal{V}} \sum_{ijkl} \sum_{\mathbf{k}, i\omega_r} G^{\mathbf{k}}_{il}(i\omega_r + i\nu_n) G^{\mathbf{k}}_{jk}(i\omega_r) \\ & \times (P^{\mathbf{k}}_{ij} - P^{\mathbf{k}}_{ji})_\alpha (P^{\mathbf{k}}_{kl} - P^{\mathbf{k}}_{lk})_\beta\end{aligned} \tag{7.67}$$

Then, the corresponding dielectric function in Matsubara representation can be calculated by

$$\varepsilon^{(1)}_{\alpha\beta}(\mathbf{0}, i\nu_n) = 1 - \frac{4\pi}{(i\omega_n)^2} \left[\Pi^{(1)}_{\alpha\beta}(\mathbf{0}, i\nu_n) + \frac{n_0 e^2}{m} \delta_{\alpha\beta} \right] \tag{7.68}$$

$$\varepsilon^{(1)}(\mathbf{0}, i\nu_n) = \frac{1}{3}\sum_{\alpha} \varepsilon^{(1)}_{\alpha\alpha}(\mathbf{0}, i\nu_n) \tag{7.69}$$

7.4 Discussion

The derivation of optical conductivity in real materials serves as a pivotal aspect of our study, providing a foundational understanding of electronic response properties within the context of our self-consistent calculation framework. In our approach, we consider the lowest-order term, the bubble term, to approximate the optical conductivity. This choice is motivated by its simplicity and relevance to weak perturbations, aligning with the assumptions of linear response theory. By focusing on the bubble term, we lay the groundwork for a systematic exploration of optical properties, allowing us to gain insights into the behavior of electrons under external fields in the weak perturbation regime.

Our consideration of the optical conductivity in a Gaussian-type Bloch wave basis on the imaginary axis is a strategic choice that seamlessly integrates with our self-consistent calculation framework. The use of imaginary time and Matsubara quantities in our numerical simulations facilitates efficient calculations and maintains consistency with the Green's function language employed throughout our methodologies. This approach not only streamlines the computational aspects but also offers a practical advantage in comparing theoretical predictions with experimental data.

The derivation of optical conductivity at the lowest order serves as a stepping stone for future investigations into more intricate aspects of electronic response properties. As we progress, higher-order terms and refinements can be systematically incorporated to enhance the accuracy of our predictions. This foundational exploration of optical conductivity enriches our calculation framework, providing additional facets for comparison with experimental observations. The versatility and adaptability of our theoretical approach, coupled with the systematic exploration of optical properties, position our study to contribute meaningfully to the broader understanding of electronic behaviors in real materials.

Chapter 8

Application - $NdNiO_2$

8.1 Introduction

The discovery of a new class of superconductors marks a major development in the field of condensed matter physics. It paves the way for a comprehensive study of the commonalities and differences between these new superconductors and their existing counterparts. By discerning similarities and differences, we can gain new perspectives and insights into the mysterious and complex nature of superconductivity, revealing the elusive microscopic mechanisms behind this fascinating quantum many-body phenomenon.

The revolutionary discovery of superconductivity in layered copper-oxide materials triggered a radical shift in the landscape of condensed matter physics and materials science. This was primarily due to the unexpectedly high transition temperatures of these materials in comparison to others known during that period. What further compounded the intrigue was the marked deviation of both superconductive and non-superconductive aspects of this finding from conventional theoretical predictions. This evident disparity underscored the potential of interacting electron physics stretching beyond the mean field theory, capable of implications bearing significant relevance to fundamental physics. In certain unique scenarios, these implications even touched the boundary of commercial feasibility.

The recent discovery of superconductivity in infinite-layer [27–29, 164] and quintuple-layer [165] d^9 nickelates has been another groundbreaking event. The case of superconducting nickelates is interesting in the sense that their superconductivity was theoreti-

cally predicted based on their structural and chemical resemblance to cuprates. Interestingly, the inspection and elucidation of the properties intrinsic to these superconducting nickelates creates an enormous scientific opportunity. It carves out the pathway to enhance and refine our understanding of the interactions between the crystal structure and local chemistry on one end and revolutionary phenomena like superconductivity on the other. This, in essence, may lead us deeper into the world of quantum mechanics and materials sciences, and at the same time broaden our perspective on a diverse range of functional materials.

8.1.1 Crystal Structure

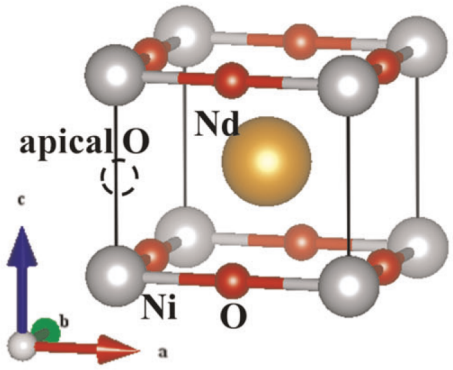

Figure 8.1: Atomic structure of tetragonal $NdNiO_2$. From Liu et al. (2020) [166].

The copper-oxide and layered nickelate materials are both transition metal oxide (TMO) compounds. These types of materials are characterized by shared structural design, particularly by the motif of the CuO_2/NiO_2 plane. This discussion begins with an examination of the simplest of these materials — the "infinite layer" $CaCuO_2$ and $NdNiO_2$. Their structure consists of transition metal ions arranged on a square planar template, with oxygen ions situated at the midpoints of the template's edges, shown as Figure 8.1. When these materials are seen in a three-dimensional context, they appear as layered compositions of transition metal/oxygen planes. In these layers, Ca/Nd ions are placed halfway between planes, directly above the square's centers formed by four transition metal ions.

There are numerous compound variations that can be formed using the CuO_2/NiO_2

motif, leading to a wide range of compounds with different detailed properties but similar overall characteristics. The focus here is on nickelate materials, not the vast variety of cuprate materials. In nickelate materials, an 'infinite layer' compound could theoretically include any rare-earth element, represented as R, as the A-site cation. Up until now, compounds inclusive of R = La, Pr, and Nd have been synthesized. Also, they can exist in multilayer forms, symbolized as $R_{1+m}Ni_mO_{2m+2}$, and can include groups of m NiO_2 planes detached by virtually insulating spacer layers of Nd and O. At present, compounds with m = 3, 4, 5 have been synthesized. Some charge transfer to spacer layers occurs, creating a distinct doping of the NiO_2 planes from the infinite layer compounds, however, their overall electronic physics is believed to be quite similar.

From a qualitative chemical perspective, the ions' electronic configurations are interpreted as $Ca^{2+}Cu^{2+}[O^{2-}]_2$ and $Nd^{3+}Ni^{1+}[O^{2-}]_2$, relating in both instances to a transition metal d^9 configuration (indicating one hole in the d-shell). Ligand field theory suggests that this hole is located in the transition metal $d_{x^2-y^2}$ orbital. It is possible to alter the chemical formula, for example, by replacing a fraction x of the Nd^{3+} with Sr^{2+}. This modification can cause changes in the Cu/Ni formal valence – altering to $d^{9\pm x}$ (either electron or hole doping). In both material families, such electron and hole doping modifications lead to dramatic changes in physical properties; more specifically, superconductivity happens exclusively within specific electron or hole doping ranges outside of the nominal d^9 valence.

8.1.2 Experiments

The prediction of nickelates to be a strong candidate for a cuprate analog can be traced back to the last century [34]. However, This claim faced opposition five years later from Kwan-Woo Lee and Warren Pickett [35]. Various groups searched for low-valence nickelates over the following fifteen years, since it is tricky to synthesize $RNiO_2$.

Finally, Hwang's group [27] reported the discovery of superconductivity in thin films of strontium-doped $NdNiO_2$, an infinite-layer nickelate, which has a similar crystal and electronic structure to copper oxide superconductors, with a T_c of about 9-15 K. To shed light on the electronic structure of these materials, X-ray spectroscopy and density functional theory have been utilized [167]. Comparisons between $LaNiO_2$, $NdNiO_2$, and cuprates have revealed notable distinctions. While similarities to cuprates exist,

infinite-layer nickelates feature a rare-earth spacer layer supporting a weakly interacting three-dimensional $5d$ metallic state. This metallic state hybridizes with a quasi-two-dimensional, strongly correlated state within the NiO_2 layers, echoing the behavior of 4f states in rare-earth heavy fermion compounds. This distinct electronic structure forms the basis from which superconductivity emerges upon doping, replacing the Mott insulator as the reference state.

Furthermore, the recent observation of superconductivity in these materials has raised fundamental questions regarding their electronic structure hierarchy. Experimental data involving state-of-the-art electron energy-loss spectroscopy have provided insights into the Mott–Hubbard character of these systems [168]. The emergence of hybridization, akin to the Zhang–Rice singlet, is a key feature, demonstrating the influence of hole doping on various electronic bands, including oxygen, nickel, and rare-earth states.

Moreover, the exploration of phase diagrams for thin films of $Nd_{1-x}Sr_xNiO_2$ on $SrTiO_3$ substrates has revealed superconducting behavior similar to cuprates [169]. These findings, however, indicate that while cuprate superconductivity exhibits boundaries between insulating and metallic phases, the nickelates demonstrate weakly insulating characteristics on either side of the superconducting dome. The normal-metallic-state Hall coefficient further supports the presence of both electron-like and hole-like bands, in agreement with band structure calculations. These discoveries have expanded our understanding of the electronic behavior in nickel oxide compounds.

In addition, experiments have extended to other nickelate compounds, such as $PrNiO_2$ [164, 170], revealing superconductivity with varying transition temperatures upon doping. These findings suggest that superconductivity in infinite layer nickelates is relatively insensitive to the details of the rare earth $4f$ configuration. They also underscore the potential for investigating a broader family of compounds based on two-dimensional NiO_2 planes, which offers opportunities for in-depth exploration of their superconducting and normal state properties and the underlying mechanisms. Notably, investigations have also touched upon the influence of rare-earth elements and ionic radii variations on the phase diagram and superconducting behavior.

Shengwei Zeng and his team [171] have meticulously conducted a research on how superconductivity varies with doping, leading to the creation of a phase diagram. The diagram displays a superconducting dome similar to that of cuprates. However, they observed that the superconductivity was marginally reduced at the center of the dome

due to the influence of multiband effects. Beyond the superconducting area, the ground state was weakly insulating, suggesting a significant deviation from the cuprates. Thus, the new nickelate bears some resemblance to the cuprates, but not entirely.

8.1.3 Theories

DFT and advanced beyond-DFT analyses have collectively unveiled a comprehensive understanding of the electronic structure of infinite layer d^9 nickelates. Similar to the cuprates, the nickelates exhibit a predominantly two-dimensional Ni-$d_{x^2-y^2}$-derived band with strong electronic correlations. However, unlike the cuprates, the Fermi surface in nickelates features an additional, more three-dimensional band derived from rare earth d-orbitals, admixing some interstitial charge and Ni($3d$) states [35, 166, 172–175]. Notably, the energy gap between Ni($3d$) and O($2p$) orbitals in nickelates is larger compared to cuprates, for example, the energy splitting in $NdNiO_2$ is almost twice larger than that in $CaCuO_2$ [35, 176, 177], putting nickelates into the Hubbard regime rather than the charge transfer regime[178]. In contrast to cuprate materials, where the relevant configurations of transition metal ions are limited to d^9 and d^{10} states, nickelate materials display some admixture of the high-spin d^8 configuration, introducing the possibility of Hund's metal physics[179].

With this general consensus, the key question pertains to which differences and similarities with cuprates are crucial for understanding the low-energy physics. In other words, it remains uncertain whether the low-energy physics of infinite layer nickelates can be comprehended within the framework of a one-band Hubbard model or if more complex physics is necessary. The resolution of this query directly influences our understanding of the mechanism behind the observed superconductivity in these materials. Unfortunately, this issue remains unresolved, partly due to varying outcomes from different flavors of the DFT + DMFT approach concerning factors like the fractional weight of high-spin d^8 configurations in the ground state, the relative energy positions of the p and d band manifolds, and the mass enhancement of various bands near the Fermi surface. Some of these disparities can be attributed to the choices inherent in the DFT+DMFT approach for correlated materials.

8.2 DFT calculations

8.2.1 Calculations with plane wave basis

We performed the DFT calculations within the Generalized Gradient Approximation (GGA) [67] and the Projector Augmented Wave (PAW) method as implemented in the Vienna ab initio simulation package (VASP) [18, 19] using the PBE [180] and B3LYP (Becke, 3-parameter, Lee–Yang–Parr) [181, 182] exchange-correlation functional. The hybrid functional demonstrates remarkable accuracy in describing systems that feature a combination of itinerant and localized electrons from different orbitals, where the delicate balance between itinerancy and localization can produce multiple competing ground states and phases [183]. In rare-earth oxides like $NdNiO_2$, both the transition metal d electrons and lanthanide f electrons play a significant role in the electronic band structure near the Fermi level [34, 35]. To effectively capture the behavior of electrons in these materials, the hybrid functional stands out as a powerful method, which can accommodate both itinerant and localized electrons seamlessly without adjustable parameters [184–186].

The currently available density functionals struggle with handling f-electrons effectively due to self-interaction errors. This is especially evident when describing the transition from an itinerant or band-like behavior, commonly observed at the onset of each period, towards localized states that typically emerge towards the period's end. This is a complex process that cannot be adequately captured by the capabilities of current DFT functionals. A widely adopted approach to handle these limitations, particularly in dealing with the localized $4f$ electrons, is to position these $4f$ electrons within the core [30]. This strategy was employed in our VASP calculations.

The lattice constants are $a = b = 3.92$ Å and $c = 3.28$ Å for $NdNiO_2$. The Brillouin zone was sampled with $6 \times 6 \times 6$ and $12 \times 12 \times 12$ mesh for DFT calculation. The kinetic energy cutoff was set to 520 eV.

Figure 8.2 shows the basic aspects of the DFT-level electronic structure of the infinite layer nickelates $NdNiO_2$. Like the cuprate band structure, nickelates exhibit a two dimensional band predominately consisting of Ni $d_{x^2-y^2}$ orbitals with a small admixture of O $2p$ character. Besides, it demonstrates an additional, much more three-dimensional band, derived from the Nd d-orbital.

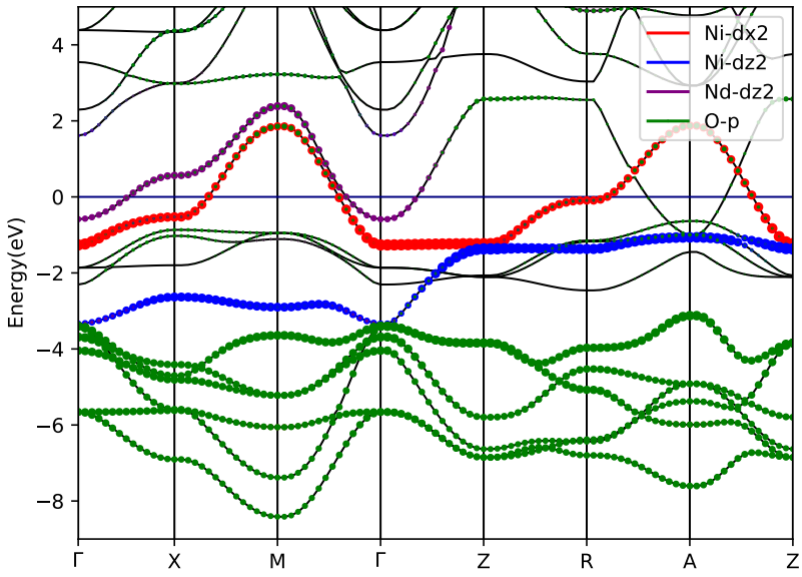

Figure 8.2: Orbital projected electronic band structures of $NdNiO_2$. The size of the red, blue, purple and green dots represents the weight of Ni $d_{x^2-y^2}$, Ni $d_{3z^2-r^2}$, Nd $d_{3z^2-r^2}$ and O p orbitals, respectively.

Charge transfer from the $d_{x^2-y^2}$-derived band to the Nd-derived band results in a phenomenon known as "self-doping". In the stoichiometric infinite layer nickelate compound, the Ni-$d_{x^2-y^2}$-derived band is partially filled. Consequently, the electronic structure of stoichiometric nickelates can be compared for the hole-doped cuprates.

It's worth highlighting that the DFT analyses, which investigate orbital admixture, rely on the projection of states onto atomic orbitals. Gu et al. [172] have discovered, through a Wannier analysis, that the extra band crossing the Fermi surfaces also has a substantial contribution originating from a charge density not centered on any specific atom. This component, known as an interstitial s orbital [172], is located at the the mid-point between two neighbouring Ni atoms along the z axis. Due to its lack of atom-centered concentration, this particular component is not easily revealed through the conventional projector analysis. Gu et al. [172] shows it by using maximally localized Wannier functions (MLWF) to fit the DFT band structure. When they add one more MLWF that corresponds to the interstitial s orbital, the fitting is improved, in particular in that Nd-derived bands are now exactly reproduced throughout the Brillouin zone.

8.2.2 Calculations with GTO basis

As outlined in Section 4.1, it's crucial to acknowledge the influence of basis set selection on the results obtained from GTO-based calculations. To address this concern, we conducted DFT calculations using two distinct computational packages, namely CRYSTAL [14, 187] and PySCF [15, 17], both of which employ GTO basis sets. The aim was to identify the most appropriate basis set for our investigations.

In our calculations for the element Nd, we considered the presence of 32 valence electrons, corresponding to the electron configuration $4s^2 4p^6 4d^{10} 4f^4 5s^2 5p^6 6s^2$. A comparison of the occupied bands derived from CRYSTAL with those from VASP reveals a noteworthy correspondence. It's important to note that in CRYSTAL, the Nd $4f$ electrons were incorporated into the valence basis, which led to a slight shift in the bands near the Fermi energy. One distinctive observation in these results is the presence of a cluster of flat bands concentrated precisely at the Fermi energy. These bands primarily correspond to the Nd $4f$ orbitals, serving as a clear indication that DFT struggles to accurately represent the behavior of rare-earth f orbitals.

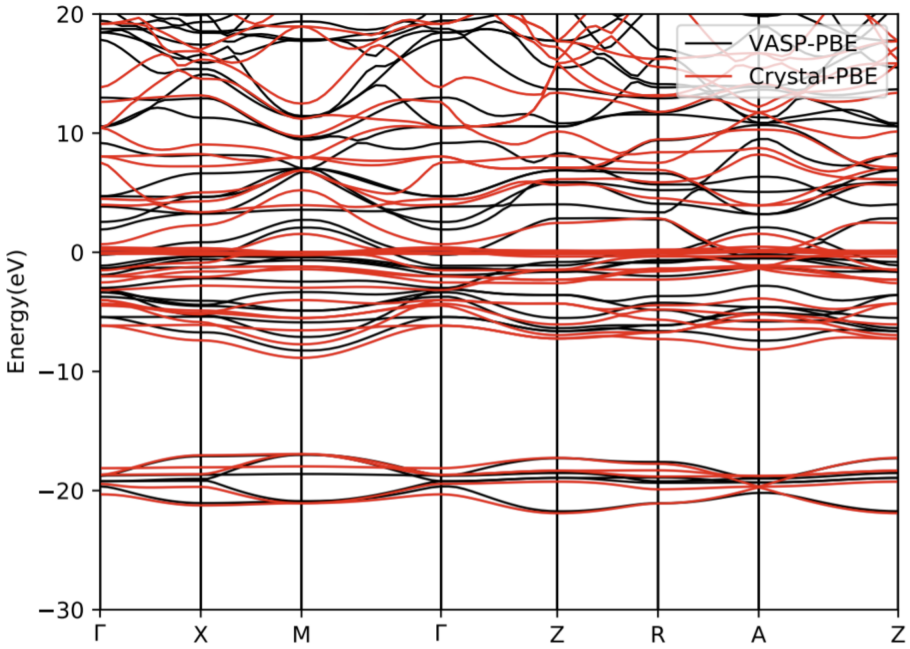

Figure 8.3: Electronic band structure of $NdNiO_2$ from VASP (black) and CRYSTAL (red) respectively. Brillouin zone was sampled with $6\times6\times6$ mesh and the exchange functional is chosen to be PBE.

Our final objective is to identify the best basis set for PySCF that provides reasonable DFT results. These results will be used as a starting point for subsequent steps. PySCF is an open-source software that simplifies the preparation of intermediate quantities such as the Fock matrix and Comloub integrals. However, PySCF is much slower than CRYSTAL, which is why we choose CRYSTAL as an intermediate step to quickly compare with VASP and find a suitable basis set. The next stage involves comparing the GTO-based results from CRYSTAL and PySCF. We sampled the Brillouin zone with a $4 \times 4 \times 4$ mesh for the DFT calculation.

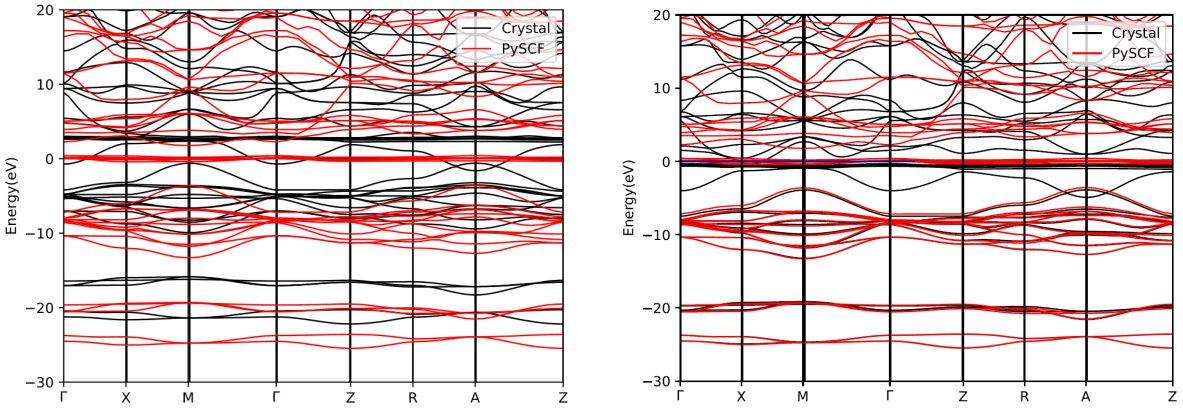

(a) original **(b) moved**

Figure 8.4: Electronic band structure of $NdNiO_2$ from CRYSTAL (black) and PySCF (red) respectively. Brillouin zone was sampled with $4 \times 4 \times 4$ mesh and the exchange functional is chosen to be PBE. On the right, the band structure of CRYSTAL has been moved to align with the occupied bands of PySCF.

It's important to highlight a notable discrepancy in the treatment of oxygen within the two computational platforms. CRYSTAL incorporates the 1s electrons of oxygen into the valence basis, while PySCF assigns these 1s electrons to the core. This differentiation arises because the 1s electrons of oxygen are situated at a significantly lower energy level. Attempting calculations with such a large energy window in PySCF could pose substantial computational challenges. This variance likely contributes to the observed energy shift between the occupied bands obtained from CRYSTAL and PySCF. However, even with the adjustment that aligns the CRYSTAL bands with the occupied bands from PySCF, certain bands in the vicinity of the Fermi surface remain unaccounted for by PySCF. It's important to note that, aside from the Nd $4f$ bands, PySCF results suggest

an insulating behavior, whereas $NdNiO_2$ is, in fact, metallic. This discrepancy highlights the limitations of PySCF in providing accurate and reliable results in this context.

8.3 GW approximation

The rationale behind undertaking GW calculations lies in the need to establish a more robust foundation for subsequent SEET calculations. While DFT serves as a valuable tool for various electronic structure investigations, its reliability may sometimes fall short in accurately representing the complex electronic interactions within the system under study. Consequently, the introduction of GW calculations aims to enhance the accuracy of our electronic structure description, making it a more suitable framework for the subsequent SEET analysis.

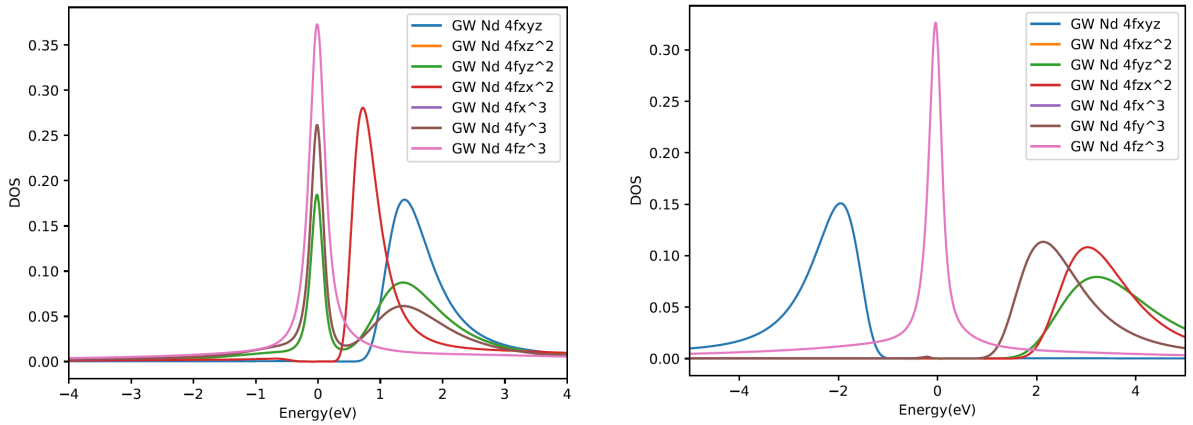

(a) Density of states of GW results starting from DFT with functional PBE.

(b) Density of states of GW results starting from DFT with functional B3LYP.

Figure 8.5: Near Fermi energy GW density of states per Nd atom resolved into Nd-4f orbitals.

Figure 8.5 illustrates self-consistent GW results originating from two different DFT starting points. Surprisingly, GW yields two disparate outcomes, a discrepancy that contradicts the expectations of self-consistent approaches.

In such scenarios, resolving this issue poses a substantial challenge, but a promising avenue emerges through the recent application of a temperature extrapolation technique, as suggested by Yu et al. [188]. This technique offers a novel perspective, as it allows self-consistent many-body methods to address the problem effectively. Although GW

may face difficulties in seeking a global minimum from a zero-temperature initial point, it can more readily identify the lowest free energy state when initialized from finite temperature results. The Caratheodory [112] temperature extrapolation technique facilitates a seamless transition across various temperatures during simulations, rendering it particularly well-suited for investigating heating and cooling processes within many-body systems. It should be noted that the starting points obtained through this method generally exhibit superior performance, especially when applied to systems characterized by phase transitions and convergence challenges.

However, it's important to note that this innovative temperature extrapolation technique is a relatively recent development, and as such, it was not employed in our specific research project. Nevertheless, it represents a promising avenue for addressing convergence issues in many-body simulations and could be valuable for future investigations in this area.

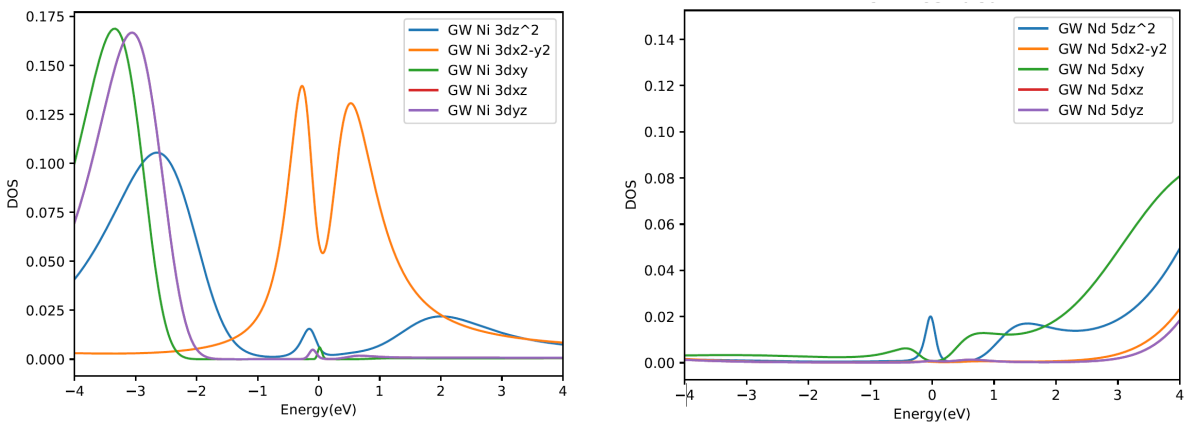

(a) Ni 3d orbitals. **(b) Nd 5d orbitals.**

Figure 8.6: Near Fermi energy GW density of states per Nd atom resolved into Ni-d and Nd-d orbitals.

Examining the data presented in Figure 8.6a, we observe that the Ni $d_{x^2-y^2}$ orbital plays a dominant role in contributing to the electronic structure near the Fermi surface. Interestingly, the Ni $d_{3z^2-r^2}$ and Ni $d_{xz/yz}$ orbitals also exhibit notable contributions at the Fermi surface. However, these contributions are primarily attributed to a form of self-doping stemming from the Nd d orbitals, a phenomenon that we will explore in more comprehensive detail in subsequent discussions.

Turning our attention to Figure 8.6b, it is evident that the Nd $5d_{3z2-r^2}$ orbital like-

wise makes a significant contribution near the Fermi energy. This observation strongly suggests the occurrence of hybridization between the Ni d and Nd d orbitals, underscoring the intricate interplay between these orbital components in shaping the electronic structure of the system.

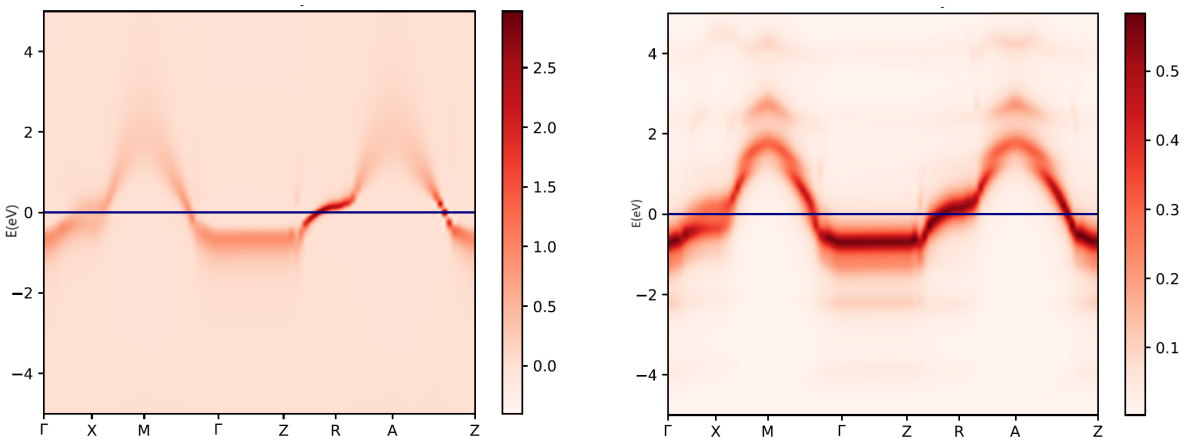

(a) GW band structure with MaxEnt analytical continuation.

(b) GW band structure with Nevanlinna analytical continuation.

Figure 8.7: Ni $3d_{x^2-y^2}$ momentum-resolved spectral functions for $NdNiO_2$ obtained from MaxEnt and Nevanlinna analytical continuation after GW calculations.

In our investigation of the predominant band at the Fermi surface, particularly focusing on the Ni $d_{x^2-y^2}$ band, we have utilized various methods for analytical continuation from the imaginary axis, as depicted in Figure 8.7. Notably, we employed two distinct techniques for this purpose, namely MaxEnt [40] and Nevanlinna [41].

As have discussed in Section 6.3, it becomes apparent that MaxEnt exhibits certain limitations in comparison to the Nevanlinna method. Specifically, MaxEnt presents a lower level of resolution, especially as we move to higher energy regimes. In contrast, Nevanlinna emerges as a more powerful approach, providing significantly enhanced resolution of the momentum-resolved spectral function near the Fermi energy.

Delving into the details of the results obtained via Nevanlinna, we discern the presence of a Z-centered pocket in the momentum-resolved spectral function. Furthermore, there are indications of a potentially existing M-centered pocket. This high level of resolution facilitated by Nevanlinna allows us to explore these nuanced features in the electronic structure near the Fermi energy.

In essence, the GW approximation is a valuable method, particularly effective for weakly correlated systems. This quantum many-body theory allows for the computation of electronic band structures and excitation energies with an accuracy often superior to that of DFT, providing a generally good starting point for SEET. In the context of describing the electronic structure of $NdNiO_2$, GW exhibits the ability to highlight the general features.

However, the GW approximation encounters challenges when applied to systems involving strongly correlated electrons. Specifically, in our case, the GW method struggles to capture the behavior of Nd f and Ni d orbitals accurately. These electrons display a high degree of correlation, characterized by strong interactions and entanglement, and hence require more sophisticated models for accurate representation.

8.4 Inner-loop SEET calculations

8.4.1 Inner-loop SEET calculations with Nd f orbitals as impurities

The initial step in Self-Energy Embedding Theory (SEET) [1–6] involves the crucial process of impurity identification. Typically, this entails selecting the specific orbitals of interest to designate as the impurity. Subsequently, the construction of the impurity Hamiltonian ensues, forming a pivotal element in the SEET framework.

What particularly fascinates us is the intriguing contrast observed in the GW results. When we initiate these calculations using the DFT framework with the B3LYP functional, a noticeable splitting pattern emerges within the $4f$ orbitals. Conversely, when employing the DFT-PBE approach, there's a distinct concentration of these orbitals at the Fermi level. This striking disparity underscores the intricate nature of f electrons within the DFT framework and the inherent challenges associated with the f bands distributed around the Fermi level, as previously observed in our DFT band structure analyses.

To address these challenges, we choose to select f orbitals as the impurities for our inner-loop SEET calculations. This choice stems from the well-established limitations of DFT in handling f electrons effectively, along with the inherent uncertainty associated with the multitude of f bands situated in the vicinity of the Fermi level. Thus, employing

f orbitals as impurities in the SEET framework allows us to circumvent these limitations and gain a more accurate representation of the material's electronic structure.

With the impurity problem delineated and f orbitals designated as impurities, the next step involves solving this impurity problem. In this endeavor, we employ Exact Diagonalization (ED) [50–53, 135], a potent computational technique that enables the treatment of up to 3 impurities. This sophisticated methodology ensures the comprehensive analysis of the electronic properties, providing valuable insights into the system under investigation while managing the computational complexities effectively.

The computational challenge with ED lies in its exponential complexity, which scales directly with the size of the impurity system [135]. This size is determined by the number of active orbitals multiplied by the number of bath orbitals adding 1. When the size of the impurity system remains relatively small, typically no more than 12, the time required for each ED solver to perform its calculations falls within acceptable limits, usually taking just several minutes.

As a consequence of this computational constraint, it's essential to carefully manage the number of active orbitals within each impurity group. To maintain computational tractability, the number of active orbitals in each group should not exceed 3. This limitation ensures that the ED calculations can be performed efficiently while still providing valuable insights into the electronic properties and interactions of the system under investigation.

Bath fitting [52] is also a vital component of embedding theory, addressing the challenge of accurately representing interactions between the active region and its environment, commonly referred to as the "bath". This interaction is crucial for modeling and understanding complex systems, encompassing disciplines such as condensed matter physics, chemistry, and materials science. Bath fitting ensures a realistic treatment of the environment's influence on the active region, including its impact on properties like charge distribution, charge transfer, and electronic coupling.

However, bath fitting is not without its challenges. It introduces additional computational complexity, particularly in large systems, leading to increased computational costs. The parameterization of the bath and the choice of its functional form can be intricate, affecting the quality and reliability of results. Additionally, bath size and the quantum mechanical methods employed for both the active region and the bath can significantly influence the quality of bath fitting. Striking the right balance between

computational accuracy and efficiency, accurate parameterization, and appropriate bath size is essential for successful bath fitting in embedding theory.

In practice, we need to adjust the related bath fitting parameters and look carefully how the minimization of the hybridization changes during the iterations. Monitoring how this hybridization evolves provides valuable insights into the convergence and stability of the calculations. It allows us to gauge whether the chosen parameters effectively describe the system's electronic structure and how they influence the accuracy and efficiency of the computational approach.

The first set of impurities is Nd $4f_{x^3}, 4f_{y^3}, 4f_{z^3}; 4f_{xz^2}, 4f_{yz^2}; 5f_{x^3}, 5f_{y^3}, 5f_{z^3}; 5f_{xz^2}, 5f_{yz^2}$ and the corresponding density of states is shown in Figure 8.8.

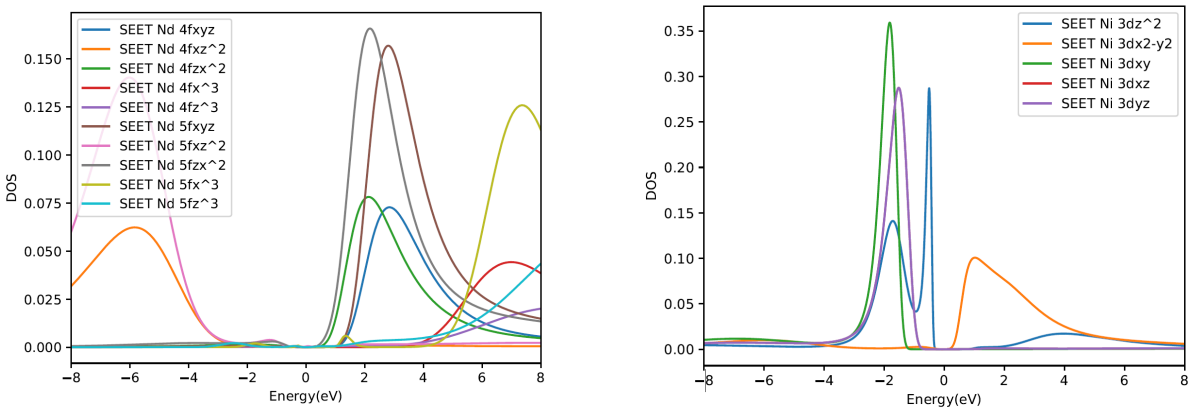

(a) Nd $4f$ orbitals. **(b) Ni $3d$ orbitals.**

Figure 8.8: Near Fermi energy inner-loop SEET density of states per Nd atom with Nd f as impurities resolved into Nd-f and Ni-d orbitals.

The observations depicted in Figure 8.8a are of significant import, shedding light on the impact of introducing Nd f orbitals as impurities within the computational framework. It is discernible that the prior arrangement of Nd f orbitals, enveloping the Fermi energy in both DFT and GW calculations, has undergone a pronounced transformation subsequent to the inclusion of these orbitals as impurities. A salient outcome of this modification is the division of the Nd f orbitals into two distinct energy regions, one situated above and the other below the Fermi energy. This bifurcation in the energy spectrum of Nd f orbitals is in concordance with the outcomes of preceding investigations, aligning with the findings reported in earlier studies [189, 190].

Upon examination of Figure 8.8a, it is observed that the Ni d orbitals, which conven-

tionally contribute significantly at the Fermi surface, much like the previously discussed Nd f orbitals, are also displaced from their initial positions around the Fermi surface. Specifically, it is anticipated that the Ni $d_{x^2-y^2}$ orbital would manifest as the primary contributor at the Fermi surface, while the Ni $d_{3z^2-r^2}$ and $d_{xz/yz}$ orbitals would make relatively minor contributions [191]. The displacement of these Ni d orbitals from their expected positions near the Fermi surface raises intriguing questions about the underlying factors influencing this behavior.

An essential facet of this investigation pertains to the introduction of Nd f orbitals as impurities, which, as elucidated earlier, correctly influence the low-energy physics of the system. Nevertheless, a contrasting outcome emerges with respect to the behavior of the Ni d orbitals, where the impurity-induced changes do not align with expectations. To address this discrepancy and acquire a more comprehensive understanding of the system's electronic behavior, the next logical step is to introduce Ni d orbitals as impurities. This additional layer of investigation will facilitate a nuanced examination of the Ni d orbitals' role and behavior within the electronic structure. By doing so, we aim to gain deeper insights into the interplay between impurities and the host system and refine our comprehension of the intricate electronic properties that emerge from these perturbations.

8.4.2 Inner-loop SEET calculation with Nd f and Ni d as impurities

Convergence and damping

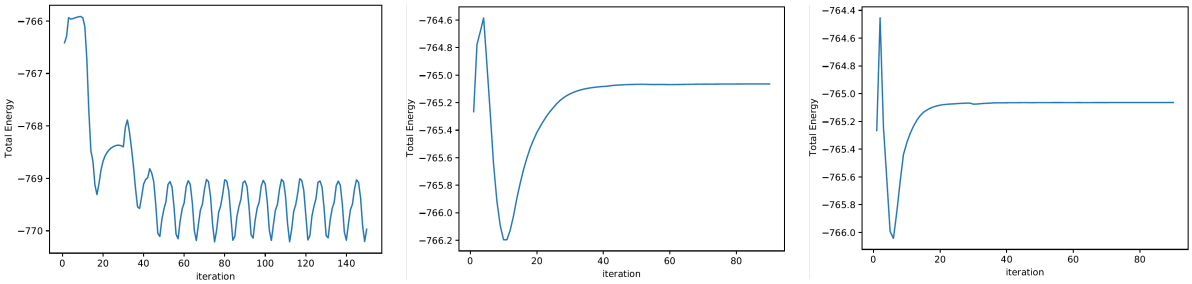

(a) damping = 0.3 **(b) damping = 0.4** **(c) damping = 0.7**

Figure 8.9: Convergence of total energy vs. iterations for inner-loop SEET calculations with Nd f and Ni d impurities under various damping conditions.

The integration of Ni d orbitals as impurities presents certain challenges, most notably that convergence becomes increasingly difficult. This difficulty arises due to the expansion of the impurity problems which, in turn, complicates their resolution. To address this, we propose utilizing an iterative acceleration method, specifically damping, to enhance the convergence process.

The damping factor, designated as x, represents a ratio that combines x times the result of the current iteration with 1-x times the one of the preceding iteration. A smaller damping factor corresponds to a higher proportion of the current iteration's results being incorporated into the mixture.

Figure 8.9 presents a visualization of the convergence, specifically demonstrating the changes in total energy across iterations, with varying damping factors applied when the designated impurities are Nd $4f_{x^3}$, $4f_{y^3}$, $4f_{z^3}$; Nd $4f_{xz^2}$, $4f_{yz^2}$; Nd $5f_{x^3}$, $5f_{y^3}$, $5f_{z^3}$; Nd $5f_{xz^2}$, $5f_{yz^2}$; Ni $3d_{x^2-y^2}$, $3d_{z^2}$; Ni $3d_{xy}$, $3d_{yz}$, $3d_{xz}$; Ni $4d_{x^2-y^2}$, $4d_{z^2}$; Ni $4d_{xy}$, $4d_{yz}$, $4d_{xz}$.

It is evident that when the damping factor is set to 0.3, the total energy exhibits fluctuations throughout the iterations, failing to converge toward a consistent energy value. Conversely, for damping factors of 0.4 and 0.7, the total energy converges to a stable level of -765.064 Hartree.

This observation underscores the critical role of the damping factor in achieving convergence in the presence of impurities, with specific values of damping influencing the convergence behavior. Notably, a damping factor of 0.4 or 0.7 appears to be the optimal choice, resulting in the convergence of total energy to a consistent and stable level, thereby enhancing the reliability of the computational results. Additionally, it is worth noting that temperature convergence methods [188] may also be employed to address these issues and further refine the results. Moreover, the use of iterative acceleration algorithms such as DIIS [192, 193] can also greatly improve the convergence rate, thereby reducing the computational time and resources required, which is particularly useful for large and complex systems.

Density of states

After the implementation of both Nd f and Ni d orbitals as impurities, shown in Figure 8.10a, the Nd f bands persist in their divided state, appearing both above and below

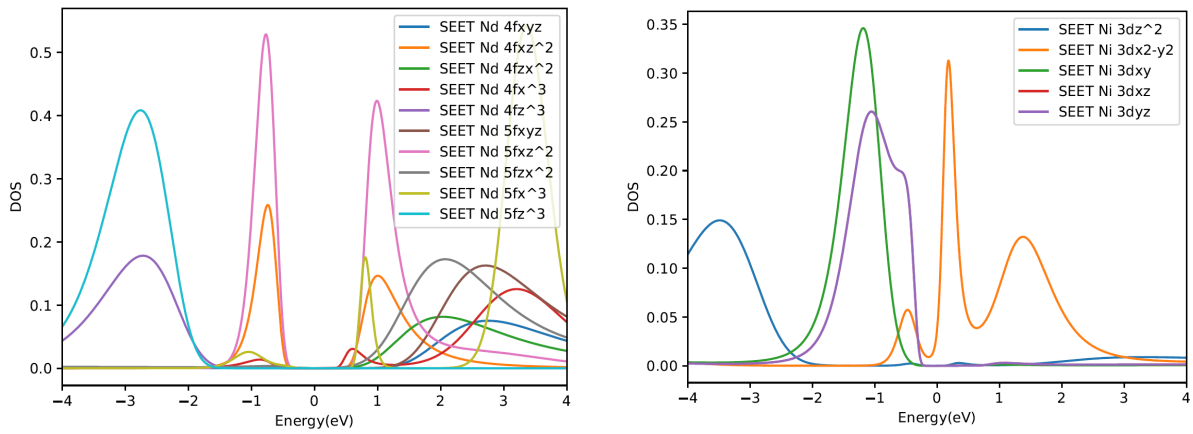

(a) Nd $4f$ orbitals. **(b) Ni $3d$ orbitals.**

Figure 8.10: Near Fermi energy inner-loop SEET density of states per Nd atom with Nd f and Ni d as impurities resolved into Nd-f and Ni-d orbitals.

the Fermi energy. This split is consistent with previous observations, and suggests that the addition of Ni d orbitals as impurity does not significantly disrupt the behavior of the Nd f bands.

Simultaneously, in Figure 8.10b, the Ni d bands display the anticipated behavior, with the Ni $d_{x^2-y^2}$ orbital primarily contributing at the Fermi surface. This phenomenon aligns with the theoretical predictions about the role and influence of this specific orbital, and further emphasizes the impact of orbital character at the Fermi surface.

Notably, the Ni d bands manifest in a manner consistent with theoretical predictions, with the Ni $d_{x^2-y^2}$ orbital playing a dominant role at the Fermi surface, while the Ni $d_{3z^2-r^2}$ orbital exhibits substantial contributions to the electronic structure below the Fermi energy. These alterations in the electronic bands are encapsulated in the local density of states, providing a comprehensive representation of the system's electronic properties.

The analysis of the ground state, as shown in Table 8.1, suggests that it is a mixture of Ni d^8, Ni d^9 and potentially Ni d^{10} configurations, with the Ni d^9 state being the most dominant. This interpretation is not unanimously agreed upon, with varying conclusions drawn from different studies.

Karp et al. [194, 195], for instance, using Density Functional Theory combined with Dynamical Mean-Field Theory (DFT+DMFT), found that the high spin d^8 configuration contributes less than 15% to the ground state. They further argued that the

Ni $3d_{x^2-y^2}$	0.83
Ni $3d_{3z^2-r^2}$	1.90
Ni $3d_{xy}$	1.98
Ni $3d_{xz/yz}$	1.95
Nd $5d_{xy}$	0.13
Nd $5d_{3z^2-r^2}$	0.12

Table 8.1: Orbital occupancies of the most relevant orbitals of $NdNiO_2$ from the Matsubara Green's function.

low-energy physics of the system is primarily dictated by the Ni-$d_{x^2-y^2}$ orbital.

On the other hand, Wang et al. [196] found a higher proportion of high spin d^8 in the ground state configuration of $LaNiO_2$—about 25.9% (and 10.8% low spin d^8). They proposed, based on this result, that the material should be considered a Hund's metal, a class of materials with unique electronic properties arising from strong spin-orbit interactions.

Interestingly, the results from Wang et al. partially align with those from a study conducted by Petocchi et al. [179] using Green's function (GW) approach and Extended Dynamical Mean-Field Theory (EDMFT). They too found that the high spin d^8 state had a significant contribution—about 25% (and a similar value for the low spin d^8 state) at the optimal doping level.

However, the discussion is far from settled. As Karp et al. [197] have shown, the choice of method used to construct the local orbitals of the downfolded model significantly impacts the results for the nickelates. This means that the precise nature of the ground state, and the relative contributions of different configurations, might vary depending on the specific computational approach used. Thus, further studies are required to conclusively determine the ground state properties of these systems.

In essence, while the introduction of the Ni d orbitals as impurities does not disrupt the splitting of the Nd f bands at the Fermi energy, it does lead to interesting behaviors in the Ni d bands themselves. Given that these findings are derived from the local density of states, it is necessary to further examine the momentum-resolved spectral function along the high symmetry path. This approach would provide a more detailed understanding of each band's character, and potentially reveal new insights into the details of electronic structure.

Momentum-resolved spectral functions

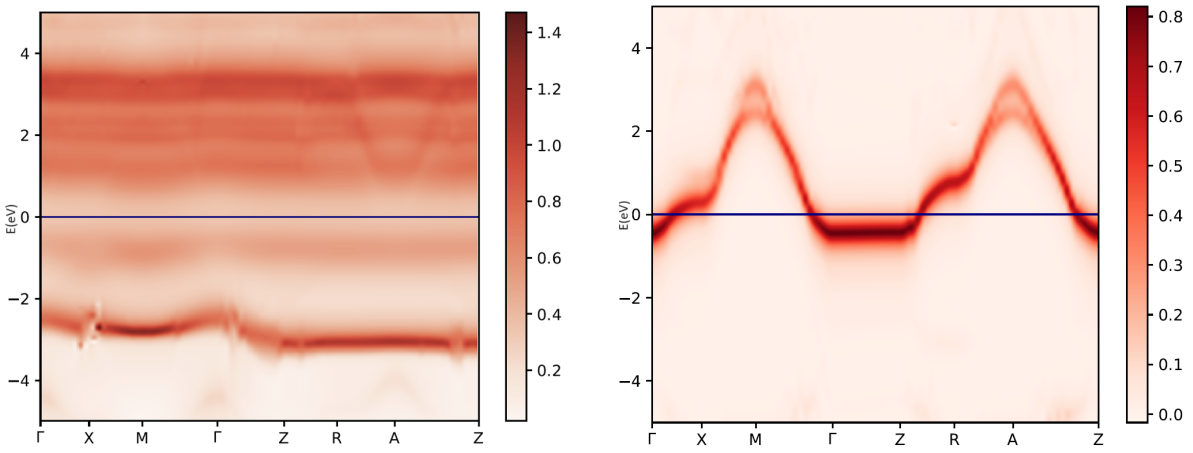

(a) Nd $4f$ **(b) Ni $3d_{x^2-y^2}$**

Figure 8.11: Momentum-resolved spectral functions for $NdNiO_2$ from inner-loop SEET calculations.

Upon examining Figure 8.11a, the Nd f bands exhibit a tendency to spread around the Fermi energy. This distribution pattern is consistent with the observations derived from the figure depicting the momentum-integrated total spectral function in Figure 8.10a, where the cumulative effect of the Nd f bands becomes evident.

In Figure 8.11b, a comprehensive insight into the behavior of the Ni-$d_{x^2-y^2}$-derived band unfolds, shedding light on its characteristics in the proximity of the Fermi energy. It becomes evident that this particular band exerts a dominant influence in the vicinity of the Fermi energy, emerging as the principal contributor to the electronic structure. Moreover, this specific band exhibits a narrowed and broadened behavior in comparison to the results deduced from DFT calculations. In terms of the band structure, the presence of an electron-like Z pocket along the Z-R path is noticeable, shown in Figure 8.12b. Notably, this feature is consistent with the predictions at the GW approximation level. This suggests that the GW approximation can provide a reasonably accurate description of the band structure in this specific region. However, an intriguing observation arises in the form of an M-centered pocket that remains conspicuously absent. Instead, the spectral function solely reflects the presence of a Γ-centered pocket in Figure 8.12a, a deviation from the anticipated outcome. This unanticipated variation in the electronic band structure characterizes the complexity of the system and highlights the impor-

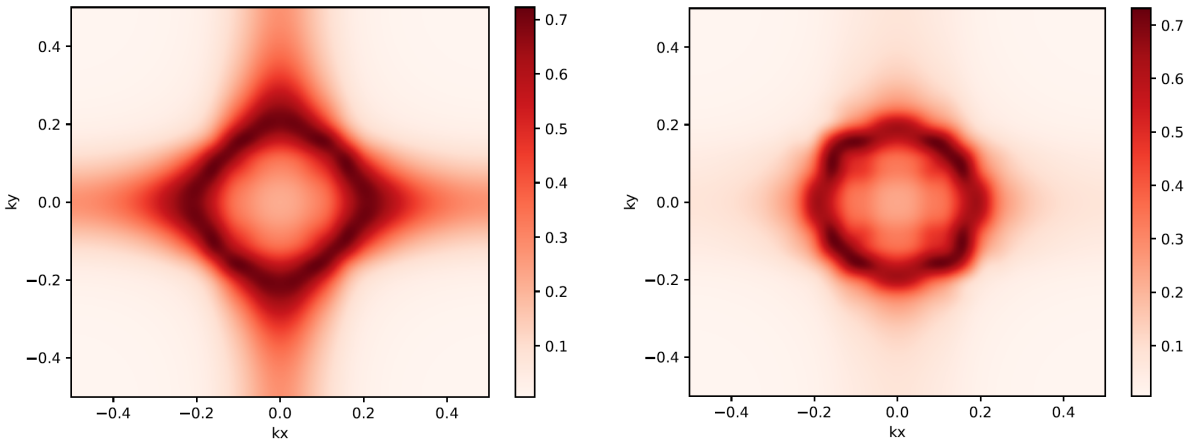

(a) Ni $3d_{x^2-y^2}$, $k_z = 0.0$ **(b) Ni $3d_{x^2-y^2}$, $k_z = 0.5$**

Figure 8.12: Many-body Fermi surfaces for $NdNiO_2$ projected to Ni $3d_{x^2-y^2}$ orbital.

tance of a meticulous and comprehensive examination to unravel the intricacies of its electronic behavior.

In Figure 8.13c and 8.13d, the analysis of the Fermi surface shows that the Nd d_{xy} orbital contributes to an oblate-shaped Fermi surface centered around the A point. This suggests that the Nd d_{xy} orbital is "doping," or adding electrons to, the Ni-$d_{xz/yz}$-derived band. This finding is consistent with results from prior calculations using DFT and DFT+U [35, 173, 198], as well as studies using DFT+DMFT [177, 194].

When we look at Figure 8.13a and 8.13b, we can also observe the A-centered pocket, which is a particular region of the Fermi surface that is centered around the A point. This observation further corroborates the doping of the Ni-$d_{xz/yz}$-derived band by the Nd d_{xy} orbital.

Table 8.1 provides additional evidence for this conclusion. The data in this table show that the Nd-derived bands hold approximately 0.1 electrons (considering both spin up and spin down states). This translates into a total doping of the Ni-$d_{xz/yz}$-derived band by about 0.1 holes, or 0.05 holes per band.

Interestingly, this level of doping is greater than what was previously identified for $LaNiO_2$ in DFT calculations [173]. The differences between these results can be attributed to the different electronegativities of the La and Nd elements. The greater electronegativity of Nd compared to La leads to a larger amount of doping, as the Nd

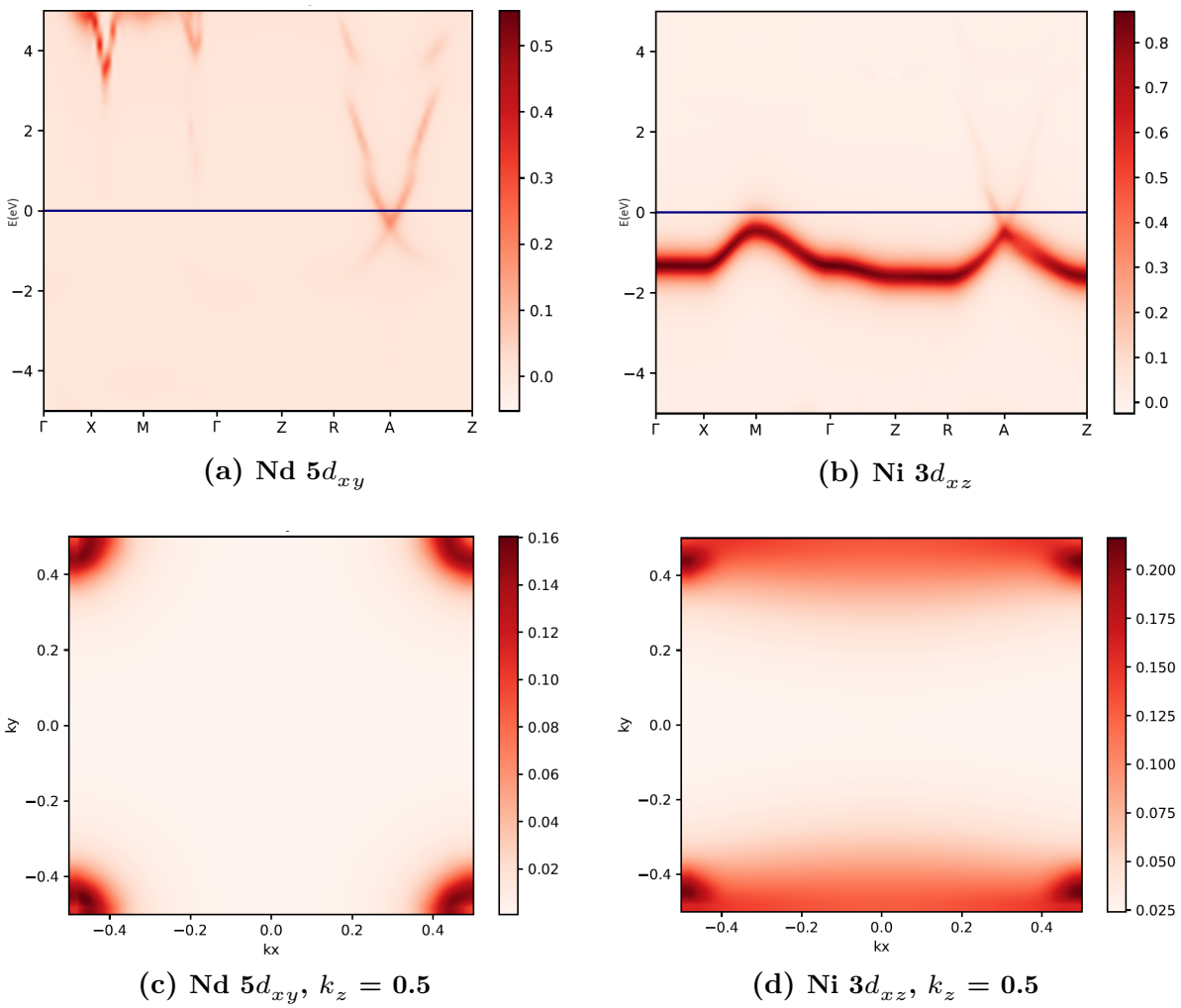

(a) Nd $5d_{xy}$ **(b) Ni $3d_{xz}$**

(c) Nd $5d_{xy}$, $k_z = 0.5$ **(d) Ni $3d_{xz}$, $k_z = 0.5$**

Figure 8.13: Momentum-resolved spectral functions and Fermi surfaces for Nd $5d_{xy}$ and Ni $3d_{xz/yz}$ orbitals.

atoms pull more electrons towards themselves, leaving more holes in the Ni-derived bands.

From Figure 8.14a and Figure 8.14b, it can be observed that the Ni-$d_{3z^2-r^2}$ orbital has a considerable degree of hybridization with the Nd-$d_{3z^2-r^2}$ band. This suggests that the Ni $d_{3z^2-r^2}$ might not just be a bystander within the system, but could have a meaningful role. Specifically, it indicates that the three-dimensional bands might not just be spectator bands, but could be involved to some degree in the correlation physics. This observation suggests that Hund's physics, characterized by the interplay

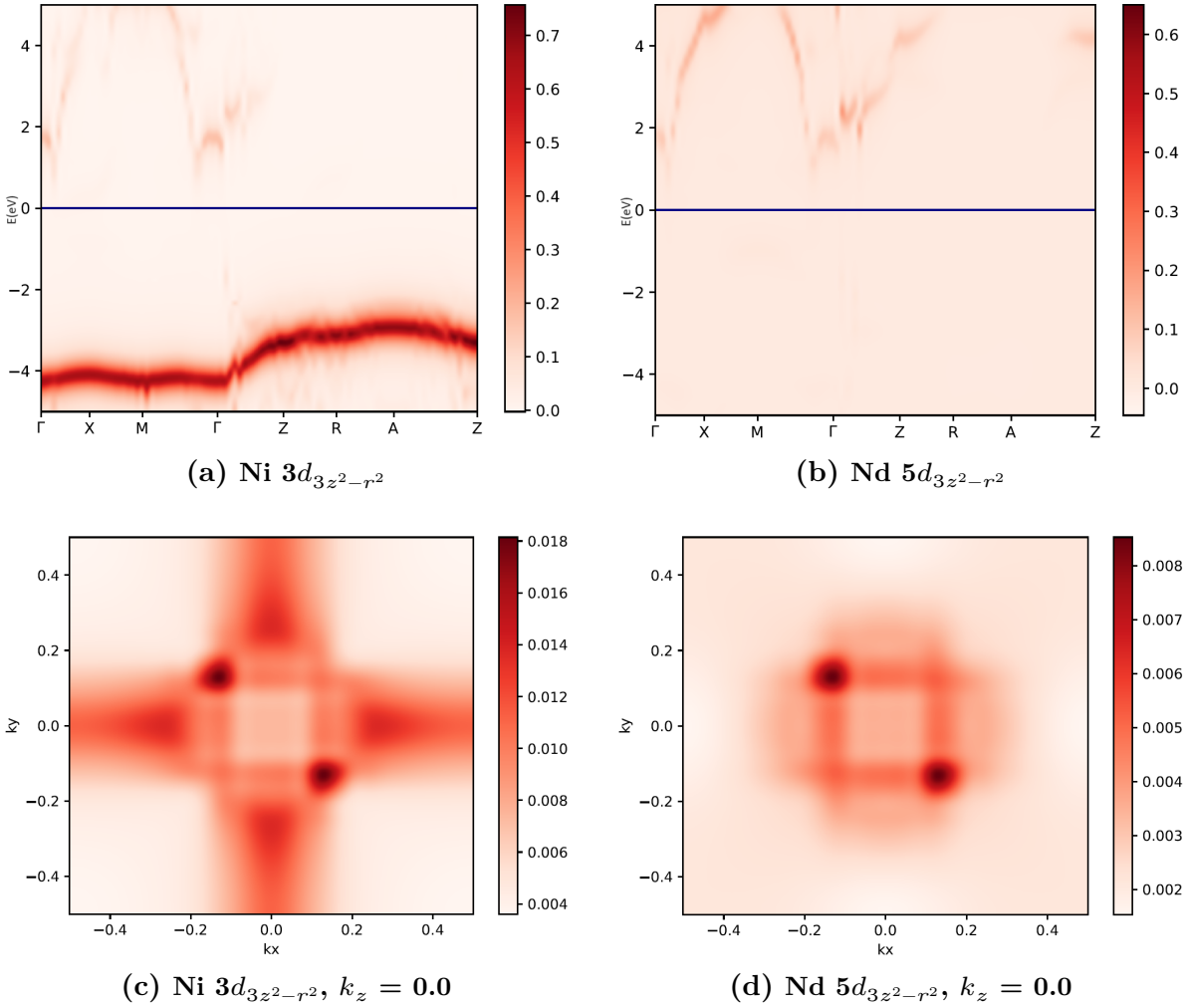

(a) Ni $3d_{3z^2-r^2}$ **(b) Nd $5d_{3z^2-r^2}$**

(c) Ni $3d_{3z^2-r^2}$, $k_z = 0.0$ **(d) Nd $5d_{3z^2-r^2}$, $k_z = 0.0$**

Figure 8.14: Momentum-resolved spectral functions and Fermi surfaces for Nd $5d_{3z^2-r^2}$ and Ni $3d_{3z^2-r^2}$ orbitals.

of electron correlations and Hund's rule coupling, could be relevant in elucidating the system's electronic behavior [191]. This notion is further supported by the findings in Table 8.1, which indicate that the Nd-$d_{3z^2-r^2}$-derived bands contribute approximately 0.1 electrons, resulting in a doping effect on the Ni-$d_{3z^2-r^2}$-derived band of about 0.1 holes.

However, it is important to note a discrepancy between the present findings and those reported by Karp et al. [194]. In their study, Karp et al. [194] documented that the Nd-$d_{3z^2-r^2}$ orbital generated a band crossing the chemical potential, consequently

giving rise to an oblate Fermi surface centered on the Γ point. In contrast, the results depicted in Figures 8.14c and 8.14d demonstrate that the Nd-$d_{3z^2-r^2}$ orbital only marginally intersects the Fermi energy, and there is no discernible Γ-centered pocket evident on the Fermi surfaces. This disparity in observations underscores the sensitivity of the electronic structure to variations in theoretical methodologies and highlights the need for further investigation to reconcile these differences and gain a comprehensive understanding of the system's electronic properties.

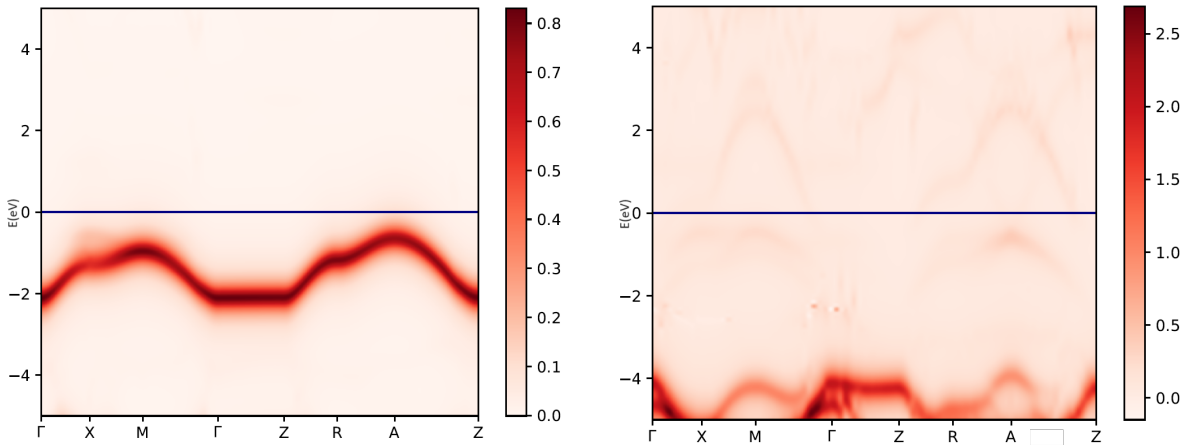

(a) Ni $3d_{xy}$ **(b) O $2p$**

Figure 8.15: Momentum-resolved spectral functions for $NdNiO_2$ from inner-loop SEET calculations (continued).

A significant consensus has emerged regarding the behavior of oxygen states in the electronic structure of $NdNiO_2$. It is widely acknowledged that the oxygen states in $NdNiO_2$ are positioned at a larger energy separation from the $d_{x^2-y^2}$ orbital compared to the cuprates [115, 173, 177, 195, 199]. Furthermore, these oxygen states exhibit weaker hybridization with the rest of the electronic structure. This implies that the incorporation of oxygen states into the electronic bands near the Fermi level is notably reduced in $NdNiO_2$ when contrasted with the cuprates. This aligns closely with the outcomes depicted in Figure 8.15b, which illustrates the limited admixture of oxygen states into the vicinity of the Fermi level bands.

However, a fundamental question still remains, namely whether $NdNiO_2$ predominantly falls within the Mott-Hubbard region or resides in a critical region characterized by a mixture of charge-transfer and Mott-Hubbard characteristics [115, 199, 200].

This distinction hinges on the nature of the material: "charge transfer" materials are governed by the energy difference between ligand and transition metal d-states, dictating their physical properties, while Mott-Hubbard materials derive their behavior from the charging energy of the transition metal d-shells [178]. Consequently, the extent to which ligand states are mixed with the transition metal states remains a pivotal and unresolved issue, significantly impacting the understanding of $NdNiO_2$'s electronic behavior. Further investigations and theoretical exploration are required to unravel this complex interplay and provide a comprehensive perspective on the material's electronic properties.

8.5 Outer-loop SEET calculations

8.5.1 Outer-loop SEET calculations with isolated Nd f orbitals as impurities

As detailed in Section 5.2.5, outer-loop SEET calculations [36] entail an iterative process where, following each inner-loop computation, an additional iteration involving weakly correlated methods, such as GW, is performed. These iterations continue until self-consistency is achieved, resulting in an self-consistent computational framework. The central objective of the outer-loop self-consistency lies in its ability to relax weakly correlated orbitals while accommodating the strong correlation effects stemming from impurity orbitals. Through empirical observations, we have discerned that the incorporation of the outer loop is particularly crucial in cases where scGW, or other weakly correlated methods, fail to provide a qualitatively accurate representation of the density of states. In this case, outer-loop SEET calculations are essential to correct these differences and generate results with excellent qualitative accuracy.

However, it is essential to acknowledged that achieving convergence in outer-loop SEET calculations can pose significant challenges. This complexity arises from the need to strike a delicate balance between strongly correlated parts of the system and weakly correlated environment. The interaction between these two states requires a rigorous convergence scheme to ensure a faithful representation of the material's electronic structure.

Given that the Nd $4f$ orbitals are inherently strongly correlated but of less immediate

interest in the context of our systems, we devised a strategic approach. In an effort to isolate the influence of these strongly correlated orbitals, we initiate the outer-loop SEET calculations with Nd f orbitals serving as impurities, without the inclusion of the bath. This strategic approach allows us to systematically disentangle the complex interactions between strongly and weakly correlated components within the system, paving the way for a more refined and precise understanding of the electronic properties of materials.

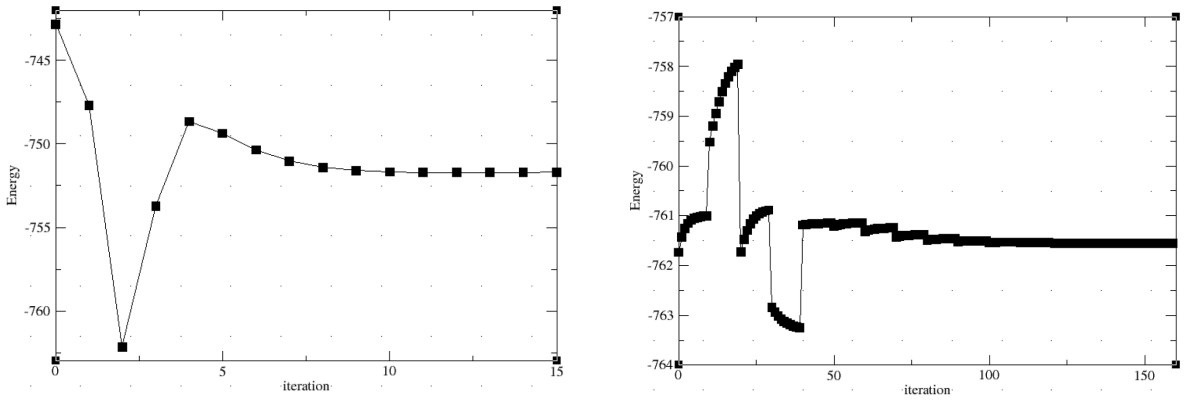

(a) Energy from GW **(b) Energy from inner-loop SEET**

Figure 8.16: Convergence of total energy vs. iterations for outer-loop SEET calculations with isolated Nd f impurities.

Figure 8.16 shows the convergence of the outer-loop SEET calculations with isolated Nd f orbitals. The trend depicted in the figure validates the efficacy of our approach of isolating the Nd f impurities for the initial outer-loop calculations. The convergence of total energy signifies that the strong correlations associated with the Nd f orbitals are being accounted for without disrupting the overall electronic structure predictions. This also indicates that the weakly correlated orbitals are effectively adapting to the strong correlation effects, thereby enhancing the accuracy and reliability of our outer-loop SEET calculations.

The comparison between results from inner-loop and outer-loop SEET calculations reveals a significant difference in the positioning of the Nd f orbitals relative to the Fermi energy. As depicted in Figure 8.17a, the outer-loop SEET calculation pushes the Nd f orbitals far from the Fermi energy.

In the context of electronic structure, the position of these orbitals relative to the Fermi energy is of critical importance. The further away these orbitals are from the

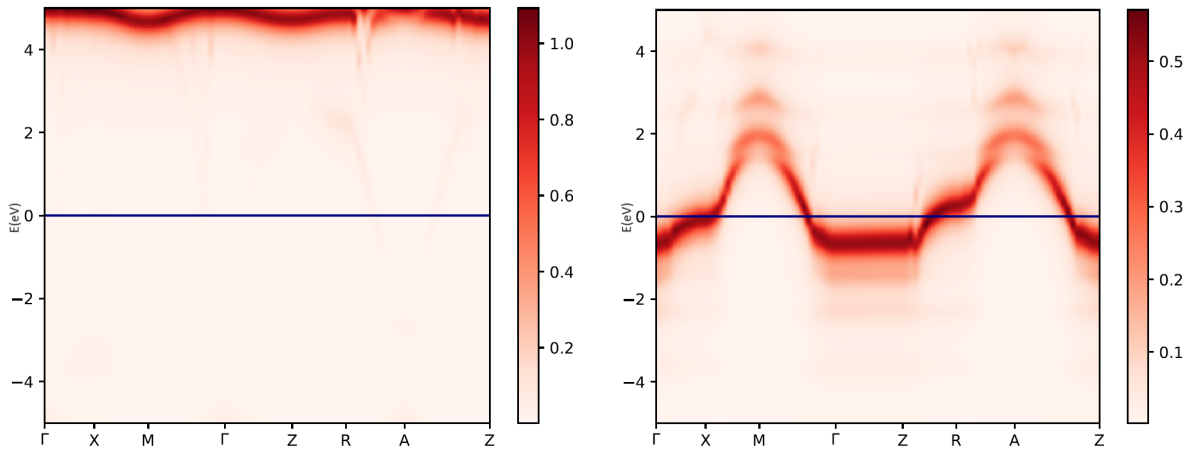

(a) Nd f **(b) Ni $3d_{x^2-y^2}$**

Figure 8.17: Momentum-resolved spectral functions for $NdNiO_2$ from outer-loop SEET calculations with isolated Nd f impurities.

Fermi energy, the less they contribute to the low-energy physics. By pushing the Nd f orbitals far from the Fermi energy, the outer-loop SEET calculations effectively isolate these orbitals from the low energy physics.

This isolation of the Nd f orbitals is in line with our expectations. By isolating these strongly correlated orbitals from the low energy physics, we can effectively reduce the complexity of the problem and obtain more accurate and reliable descriptions of the electronic structure.

Figure 8.17b presents the momentum-resolved spectral function of the Ni-$3d_{x^2-y^2}$-derived band, highlighting the distinctive features obtained through the outer-loop SEET calculation. Evidently, this methodology continues to reproduce the electron-like Z-centered pocket, a characteristic already successfully captured by the inner-loop SEET calculation, as showcased in Figure 8.18b.

However, the outer-loop SEET calculation brings a notable addition to the forefront, revealing the presence of an M-centered pocket in the momentum-resolved spectral function, as indicated in Figure 8.18a. This particular feature had eluded the inner-loop calculation but aligns with previous findings [179, 194], lending further credibility to the capabilities of the outer-loop SEET approach in providing a comprehensive description of the electronic structure.

Figure 8.19a shows that the presence of the Nd $5d_{xy}$ orbital is manifested by a con-

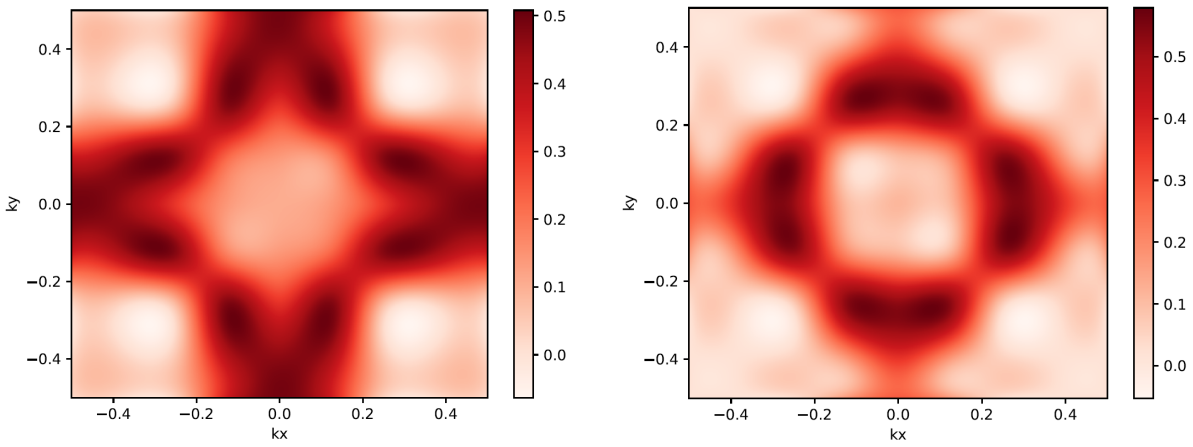

(a) Ni $3d_{x^2-y^2}$, $k_z = 0.0$ **(b) Ni $3d_{x^2-y^2}$, $k_z = 0.5$**

Figure 8.18: Fermi surfaces for Ni $3d_{x^2-y^2}$ from outer-loop SEET calculations with isolated Nd f impurities.

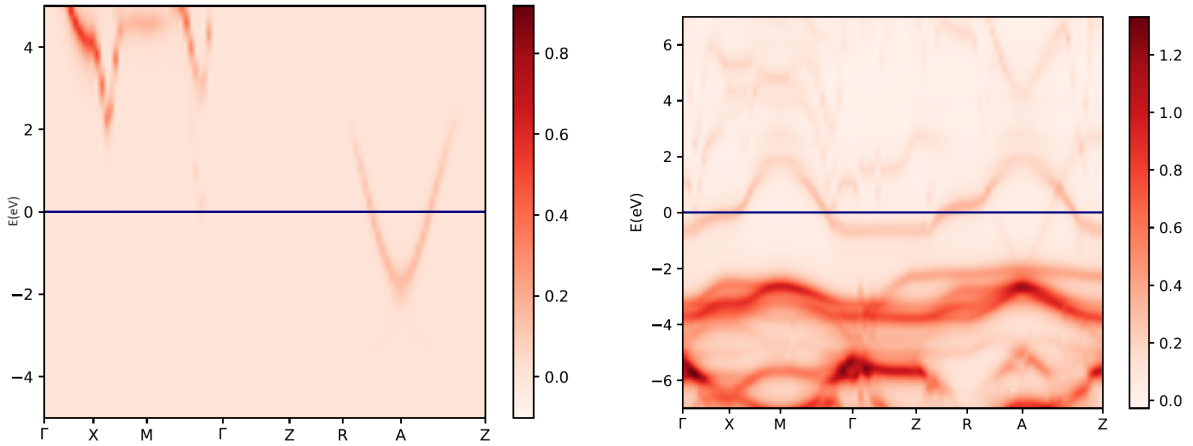

(a) Nd $5d_{xy}$ **(b) O p**

Figure 8.19: Momentum-resolved spectral functions for $NdNiO_2$ from outer-loop SEET calculations with isolated Nd f impurities (continued).

siderably larger Fermi surface which is centered at the A point. This enhanced Nd $5d_{xy}$ orbital presence exerts a more substantial influence on the Ni-$d_{xz/yz}$-derived band, effectively increasing the doping in this band when contrasted with the inner-loop calculations. This pronounced effect is further substantiated by the data in Table 8.1, which highlights a slightly larger occupation number associated with the Nd $5d_{xy}$ orbitals, directly corresponding to a greater self-doping effect.

On the other hand, Figure 8.19b delves into the behavior of the O p bands, illuminating their response to the outer-loop SEET calculation. A noticeable observation is the displacement of these bands to lower energy levels, thus implying weaker hybridization with the Ni d orbitals. This shift suggests a reduced interaction between the O p and Ni d orbitals compared to what is seen in the inner-loop calculation.

Ni $3d_{x^2-y^2}$	1.09
Ni $3d_{3z^2-r^2}$	1.79
Ni $3d_{xy}$	1.99
Ni $3d_{xz/yz}$	1.97
Nd $5d_{xy}$	0.14
Nd $5d_{3z^2-r^2}$	0.12
Nd $4f$	3.56

Table 8.2: Orbital occupancies of the most relevant orbitals of $NdNiO_2$ from outer-loop SEET calculations with isolated Nd f impurities.

These findings collectively demonstrate the capacity of the outer-loop SEET calculation to provide a more comprehensive understanding of the electronic structure and its underlying intricacies.

8.5.2 Outer-loop SEET calculations with isolated Nd f and Ni d orbitals as impurities

Building upon the successful convergence achieved in the outer-loop SEET calculations with isolated Nd f orbitals, the logical progression involves introducing Ni d orbitals as additional impurities in the outer-loop computations.

However, the situation takes an unexpected turn in the outer-loop calculations where both Nd f and Ni d orbitals are included as impurities. First of all, the calculation are not able to achieve convergence after more than 500 iterations. Then, surprisingly, the convergence process results in an occupation number for Ni $3d_{x^2-y^2}$ that exceeds 2, which is totally unphysical, as illustrated in Figure 8.20b. This peculiar behavior raises questions about the accuracy of the computed results.

Furthermore, Figure 8.21 reveals that Ni $d_{x^2-y^2}$ is pushed away from the Fermi energy, while Ni d_{xy} hovers around the Fermi energy. These findings deviate from the expected physical behavior, casting doubt on the reliability of the obtained outcomes.

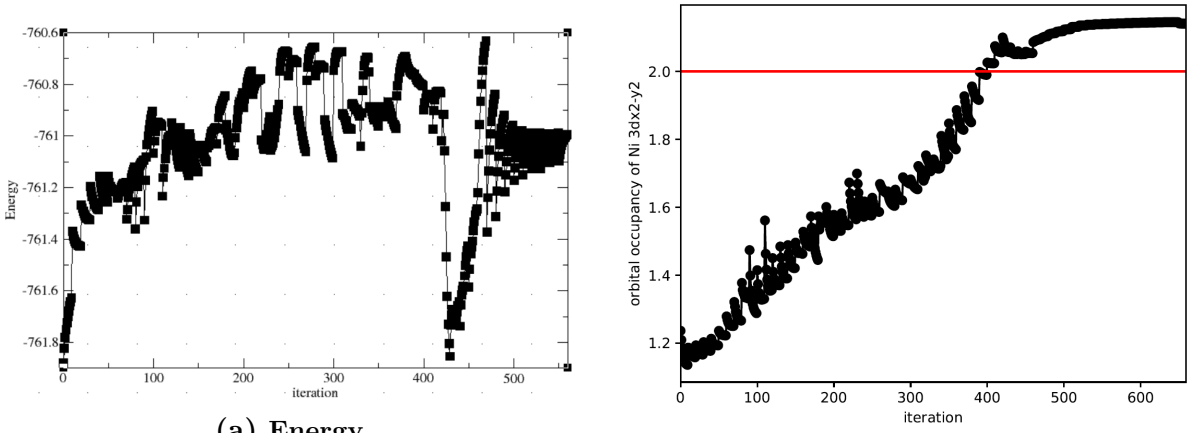

(a) Energy

(b) Orbital occupancy of Ni $3d_{x^2-y^2}$

Figure 8.20: Convergence of total energy / Ni $3d_{x^2-y^2}$ occupancy vs. iterations for outer-loop SEET calculations with isolated Nd f plus Ni d as impurities.

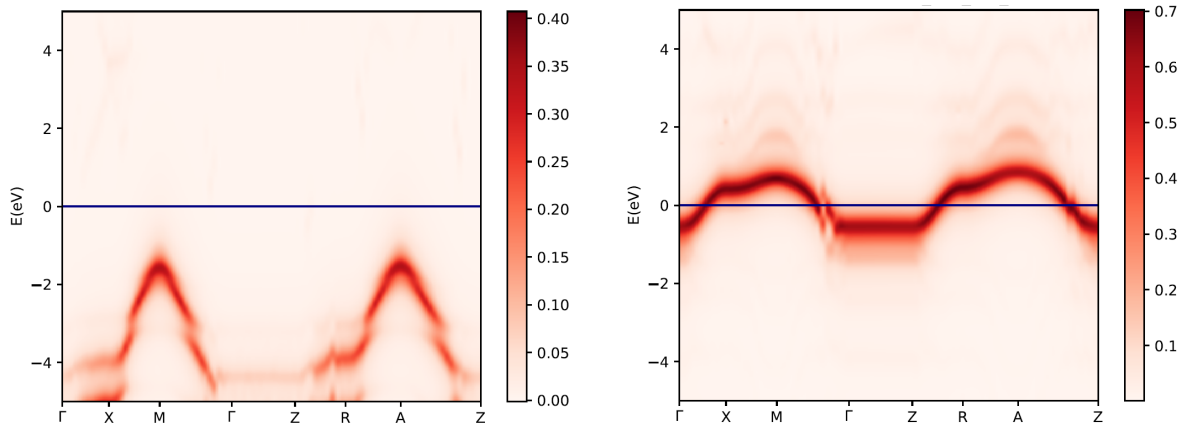

(a) Ni $3d_{x^2-y^2}$

(b) Ni $3d_{xy}$

Figure 8.21: Momentum-resolved spectral functions for $NdNiO_2$ from outer-loop SEET calculations with isolated Nd f plus Ni d as impurities.

8.5.3 Outer-loop SEET calculations with isolated Nd f and Ni d e_g orbitals as impurities

The decision to conduct outer-loop SEET calculations with isolated Nd f and Ni d e_g orbitals as impurities stems from a critical observation that Ni $d_{x^2-y^2}$ was pushed away from the Fermi energy, while Ni d_{xy} occupied a position around the Fermi energy in the previous calculation. To investigate this phenomenon further, we specifically focus

on the impurities consisting of Ni $d_{x^2-y^2}$, Ni d_{z^2} (collectively representing the e_g orbitals), and Nd f orbitals. The objective is to ascertain whether the previously observed exchange in occupancy between Ni $d_{x^2-y^2}$ and Ni d_{xy} persists in this configuration.

It's also noteworthy that achieving the convergence of the outer-loop SEET calculation may require a significant number of iterations, underscoring the computational complexity and the intricate balancing act involved in these calculations. This also emphasizes the need for iterative refinement and adjustment in electronic structure calculations to ensure that the results are not only accurate but also robust and consistent. In light of these challenges, we have incorporated iterative acceleration techniques, such as Direct Inversion in the Iterative Subspace (DIIS), as a means to expedite the convergence process and enhance the overall efficiency of the calculations. See more details in Section 5.2.6.

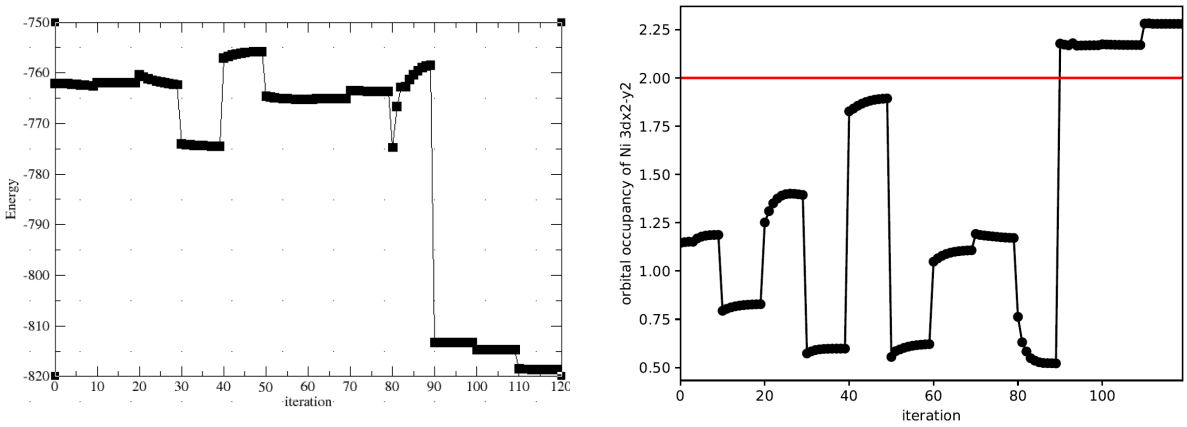

(a) Energy **(b) Orbital occupancy of Ni $3d_{x^2-y^2}$**

Figure 8.22: Convergence of total energy / Ni $3d_{x^2-y^2}$ occupancy vs. iterations for outer-loop SEET calculations with isolated Nd f plus Ni d e_g as impurities.

Even after DIIS is applied, the whole system is still hard to converge in the outer-loop calculation with Nd f and Ni d e_g orbitals as impurity. As shown in Figure 8.22b, the occupation number of Ni $3d_{x^2-y^2}$ still exceeds 2, evolving into an unphysical state.

Chapter 9

Conclusions

In this thesis, we report results from a fully self-consistent parameter-free ab initio SEET [1–6] consisting of a weakly correlated environment (treated at the level of GW) and strongly correlated orbitals (treated with ED). SEET is a hybrid approach that employs both a weakly correlated and a strongly correlated Green's function method. The self-energy of the active space is incorporated into the self-energy obtained from a perturbative approach to the treatment of non-local correlation effects. A highly accurate approach describes the selected subsystem, while a lower-level approach maintains the description of the environment at a lower level. Since SEET is derivable from a universal functional, it implicitly satisfies conservation laws and thermodynamic consistency [1] and the formulation in the Green's function language provides access not only to total energies but also to photoelectron and angular momentum resolved (ARPES) spectra as well as thermodynamic quantities. It avoids intruder states and does not require any high-order reduced density matrices [3]. The double counting problem does not appear and the accuracy can be improved either by increasing the perturbation order or by enlarging the active space [2]. The theory does not use any adjustable parameters and is fully ab initio, while being able to treat both the strong correlation and the nonlocal screening physics of these materials [6].

Our comprehensive investigation into the electronic structure of $NdNiO_2$ through the aforementioned framework with various computational methodologies has provided valuable insights and raised intriguing questions. The journey began with DFT calculations using VASP, which highlighted the two-dimensional band structure dominated by Ni $d_{x^2-y^2}$ orbitals, resembling the cuprate electronic structure. Additionally, the Nd

d orbitals contributed to a more three-dimensional band. The concept of self-doping, manifested as charge transfer between Ni $d_{x^2-y^2}$ and Nd-derived bands, underscored the intricate interplay within the stoichiometric infinite layer nickelate compound.

The exploration of different GTO-based DFT calculations using CRYSTAL and PySCF emphasized the influence of basis set selection on the results. CRYSTAL results showed a correspondence with VASP, while PySCF exhibited limitations in accurately representing the metallic behavior of $NdNiO_2$. This underscored the importance of selecting an appropriate basis set for reliable DFT outcomes.

Moving beyond DFT, our GW calculations aimed to establish a robust foundation for subsequent SEET analyses. The Ni $d_{x^2-y^2}$ orbital played a dominant role in shaping the electronic structure near the Fermi surface, while notable contributions from the Ni $d_{3z^2-r^2}$ and Ni $d_{xz/yz}$ orbitals were observed. The Nd $5d_{3z^2-r^2}$ orbital also made a significant contribution, indicating hybridization between Ni and Nd orbitals.

However, challenges arose when applying the GW approximation to systems with strongly correlated electrons, such as Nd f and Ni d orbitals. The limitations of the GW method in capturing the behavior of highly correlated electrons highlighted the need for more sophisticated models to achieve accurate representations.

The exploration of inner-loop SEET results with Nd f as impurities revealed a transformation in the arrangement of Nd f orbitals near the Fermi energy. The inclusion of Ni d orbitals in subsequent inner-loop SEET calculations led to a spread of Nd f bands and the emergence of electron-like Z and Γ-centered pockets in the Fermi surface. The self-doping effect of Nd d_{xy} and Nd $d_{3z^2-r^2}$ orbitals on Ni $d_{xz/yz}$-derived bands further highlighted the intricate interplay in the system.

Outer-loop SEET calculations, initially with isolated Nd f as impurities, successfully reproduced the electron-like Z-centered pocket and introduced an M-centered pocket in the momentum-resolved spectral function. The enhanced presence of Nd $5d_{xy}$ orbitals exerted a more substantial influence on Ni $d_{xz/yz}$-derived bands, leading to increased self-doping effects.

Surprisingly, the outer-loop SEET calculations with both isolated Nd f and Ni d as impurities faced convergence issues and yielded unphysical results, raising questions about the limitations of the methodology in capturing the complex electronic structure of $NdNiO_2$.

In summary, our investigation has uncovered the complexities and challenges in accu-

rately describing the electronic structure of $NdNiO_2$. The combination of various computational methods, from DFT to GW and inner- to outer-loop SEET, has provided valuable insights into the interplay of different orbitals and the self-doping phenomena in this unique material. The limitations observed underscore the need for further refinement and the development of advanced theoretical models to capture the intricacies of strongly correlated electron systems.

In addition to the investigation of the spectral function, our exploration of optical properties, including the derivation of optical conductivity, adds a valuable dimension to our research. By deriving optical conductivity in the Green's function language from lowest to higher order, we aim to establish a comprehensive understanding of the electronic band structure of real materials, paving the way for a more nuanced comparison with experimental data.

In looking forward, the complexities and challenges encountered in our study of $NdNiO_2$ underscore the need for continued exploration and refinement of theoretical methodologies in the realm of correlated electron systems. The limitations observed, particularly in capturing the behavior of strongly correlated Nd f and Ni d orbitals, motivate the development of advanced models that can provide more accurate representations.

The convergence issues observed in the outer-loop SEET calculations with both isolated Nd f and Ni d as impurities raise intriguing questions about the applicability of the methodology to systems with highly entangled electronic structures. Addressing these challenges will require a concerted effort to enhance the sophistication of theoretical frameworks, potentially incorporating more advanced impurity solvers and refining the embedding strategies.

Additionally, the discrepancy between the PySCF results, suggesting an insulating behavior, and the metallic nature of $NdNiO_2$ highlights the importance of benchmarking different computational packages and basis sets. Future research should focus on systematically assessing the performance of various methodologies and identifying the most suitable combination for accurately describing the electronic properties of complex materials.

As we look ahead, the study of correlated electron systems, especially those with intricate electronic structures like $NdNiO_2$, will benefit from a multi-faceted approach. Integration with experimental data, such as advanced spectroscopic techniques, will

provide critical benchmarks for validating theoretical predictions and refining computational models. Collaborative efforts between theorists and experimentalists will be essential to unravel the mysteries of these fascinating materials.

Furthermore, the exploration of materials with similar crystal and electronic structures to $NdNiO_2$, driven by the quest for additional superconductors and insights into the origins of copper oxide superconductivity, opens new avenues for research. The recent discovery of superconductivity in Sr-doped $NdNiO_2$ adds an exciting dimension to the field, prompting further investigations into the factors influencing superconducting behaviors in nickelate compounds.

Bibliography

[1] D. Zgid and E. Gull. "Finite temperature quantum embedding theories for correlated systems". In: *New Journal of Physics* 19.2 (2017), p. 023047.

[2] A. A. Kananenka, E. Gull, and D. Zgid. "Systematically improvable multiscale solver for correlated electron systems". In: *Physical Review B* 91.12 (2015), p. 121111.

[3] T. N. Lan, A. A. Kananenka, and D. Zgid. "Communication: Towards ab initio self-energy embedding theory in quantum chemistry". In: *The Journal of chemical physics* 143.24 (2015).

[4] T. Nguyen Lan, A. A. Kananenka, and D. Zgid. "Rigorous ab initio quantum embedding for quantum chemistry using Green's function theory: Screened interaction, nonlocal self-energy relaxation, orbital basis, and chemical accuracy". In: *Journal of Chemical Theory and Computation* 12.10 (2016), pp. 4856–4870.

[5] T. N. Lan and D. Zgid. "Generalized self-energy embedding theory". In: *The journal of physical chemistry letters* 8.10 (2017), pp. 2200–2205.

[6] S. Iskakov, C.-N. Yeh, E. Gull, and D. Zgid. "Ab initio self-energy embedding for the photoemission spectra of NiO and MnO". In: *Physical Review B* 102.8 (2020), p. 085105.

[7] L. Hedin and S. Lundqvist. "Effects of electron-electron and electron-phonon interactions on the one-electron states of solids". In: *Solid state physics*. Vol. 23. Elsevier, 1970, pp. 1–181.

[8] C.-N. Yeh, S. Iskakov, D. Zgid, and E. Gull. "Fully self-consistent finite-temperature G W in Gaussian Bloch orbitals for solids". In: *Physical Review B* 106.23 (2022), p. 235104.

[9] A. Georges, G. Kotliar, W. Krauth, and M. J. Rozenberg. "Dynamical mean-field theory of strongly correlated fermion systems and the limit of infinite dimensions". In: *Reviews of Modern Physics* 68.1 (1996), p. 13.

[10] W. Metzner and D. Vollhardt. "Correlated lattice fermions in d=∞ dimensions". In: *Physical review letters* 62.3 (1989), p. 324.

[11] A. Georges and G. Kotliar. "Hubbard model in infinite dimensions". In: *Physical Review B* 45.12 (1992), p. 6479.

[12] L. J. Sham and W. Kohn. "One-particle properties of an inhomogeneous interacting electron gas". In: *Physical Review* 145.2 (1966), p. 561.

[13] J. McClain, Q. Sun, G. K.-L. Chan, and T. C. Berkelbach. "Gaussian-based coupled-cluster theory for the ground-state and band structure of solids". In: *Journal of chemical theory and computation* 13.3 (2017), pp. 1209–1218.

[14] R. Dovesi, A. Erba, R. Orlando, C. M. Zicovich-Wilson, B. Civalleri, L. Maschio, M. Rérat, S. Casassa, J. Baima, S. Salustro, et al. "Quantum-mechanical condensed matter simulations with CRYSTAL". In: *Wiley Interdisciplinary Reviews: Computational Molecular Science* 8.4 (2018), e1360.

[15] Q. Sun, X. Zhang, S. Banerjee, P. Bao, M. Barbry, N. S. Blunt, N. A. Bogdanov, G. H. Booth, J. Chen, Z.-H. Cui, et al. "Recent developments in the PySCF program package". In: *The Journal of chemical physics* 153.2 (2020).

[16] T. D. Kühne, M. Iannuzzi, M. Del Ben, V. V. Rybkin, P. Seewald, F. Stein, T. Laino, R. Z. Khaliullin, O. Schütt, F. Schiffmann, et al. "CP2K: An electronic structure and molecular dynamics software package-Quickstep: Efficient and accurate electronic structure calculations". In: *The Journal of Chemical Physics* 152.19 (2020).

[17] Q. Sun, T. C. Berkelbach, N. S. Blunt, G. H. Booth, S. Guo, Z. Li, J. Liu, J. McClain, E. R. Sayfutyarova, S. Sharma, S. Wouters, and G. Chan. "Pyscf: the python-based simulations of chemistry framework". In: *WIREs Computational Molecular Science* 8 (1 2017). DOI: 10.1002/wcms.1340.

[18] G. Kresse and J. Furthmüller. "Efficiency of ab-initio total energy calculations for metals and semiconductors using a plane-wave basis set". In: *Computational materials science* 6.1 (1996), pp. 15–50.

[19] G. Kresse and J. Furthmüller. "Efficient iterative schemes for ab initio total-energy calculations using a plane-wave basis set". In: *Physical review B* 54.16 (1996), p. 11169.

[20] I. Nekrasov, N. Pavlov, and M. Sadovskii. "Consistent LDA'+ DMFT approach to the electronic structure of transition metal oxides: Charge transfer insulators and correlated metals". In: *Journal of Experimental and Theoretical Physics* 116 (2013), pp. 620–634.

[21] H. T. Dang, X. Ai, A. J. Millis, and C. A. Marianetti. "Density functional plus dynamical mean-field theory of the metal-insulator transition in early transition-metal oxides". In: *Physical Review B* 90.12 (2014), p. 125114.

[22] L. Zhang, P. Staar, A. Kozhevnikov, Y.-P. Wang, J. Trinastic, T. Schulthess, and H.-P. Cheng. "DFT+ DMFT calculations of the complex band and tunneling behavior for the transition metal monoxides MnO, FeO, CoO, and NiO". In: *Physical Review B* 100.3 (2019), p. 035104.

[23] A. Hampel, S. Beck, and C. Ederer. “Effect of charge self-consistency in DFT+ DMFT calculations for complex transition metal oxides”. In: *Physical Review Research* 2.3 (2020), p. 033088.

[24] H. T. Dang and A. J. Millis. “Theory of ferromagnetism in vanadium-oxide based perovskites”. In: *Physical Review B* 87.15 (2013), p. 155127.

[25] H. T. Dang, A. J. Millis, and C. A. Marianetti. “Covalency and the metal-insulator transition in titanate and vanadate perovskites”. In: *Physical Review B* 89.16 (2014), p. 161113.

[26] C.-N. Yeh, S. Iskakov, D. Zgid, and E. Gull. “Electron correlations in the cubic paramagnetic perovskite Sr (V, Mn) O 3: Results from fully self-consistent self-energy embedding calculations”. In: *Physical Review B* 103.19 (2021), p. 195149.

[27] D. Li, K. Lee, B. Y. Wang, M. Osada, S. Crossley, H. R. Lee, Y. Cui, Y. Hikita, and H. Y. Hwang. “Superconductivity in an infinite-layer nickelate”. In: *Nature* 572.7771 (2019), pp. 624–627.

[28] M. Osada, B. Y. Wang, B. H. Goodge, S. P. Harvey, K. Lee, D. Li, L. F. Kourkoutis, and H. Y. Hwang. “Nickelate superconductivity without rare-earth magnetism:(La, Sr) NiO2”. In: *Advanced Materials* 33.45 (2021), p. 2104083.

[29] S. Zeng, C. Li, L. E. Chow, Y. Cao, Z. Zhang, C. S. Tang, X. Yin, Z. S. Lim, J. Hu, P. Yang, et al. “Superconductivity in infinite-layer nickelate La1- xCaxNiO2 thin films”. In: *Science advances* 8.7 (2022), eabl9927.

[30] G. Kresse. “VASP the Guide”. In: *http://cms. mpi. univie. ac. at/vasp/* (2001).

[31] J. G. Bednorz and K. A. Müller. “Possible high T c superconductivity in the Ba-La- Cu- O system”. In: *Zeitschrift für Physik B Condensed Matter* 64.2 (1986), pp. 189–193.

[32] M.-K. Wu, J. R. Ashburn, C. Torng, P.-H. Hor, R. L. Meng, L. Gao, Z. J. Huang, Y. Wang, and a. Chu. “Superconductivity at 93 K in a new mixed-phase Y-Ba-Cu-O compound system at ambient pressure”. In: *Physical review letters* 58.9 (1987), p. 908.

[33] J. Orenstein and A. Millis. “Advances in the physics of high-temperature superconductivity”. In: *Science* 288.5465 (2000), pp. 468–474.

[34] V. Anisimov, D. Bukhvalov, and T. Rice. “Electronic structure of possible nickelate analogs to the cuprates”. In: *Physical Review B* 59.12 (1999), p. 7901.

[35] K.-W. Lee and W. Pickett. “Infinite-layer La Ni O 2: Ni 1+ is not Cu 2+”. In: *Physical Review B* 70.16 (2004), p. 165109.

[36] C.-N. Yeh, A. Shee, S. Iskakov, and D. Zgid. “Testing the Green’s function coupled cluster singles and doubles impurity solver on real materials within the framework of self-energy embedding theory”. In: *Physical Review B* 103.15 (2021), p. 155158.

[37] S. Fuchs, T. Pruschke, and M. Jarrell. “Analytic continuation of quantum Monte Carlo data by stochastic analytical inference”. In: *Physical Review E* 81.5 (2010), p. 056701.

[38] R. Bryan. “Maximum entropy analysis of oversampled data problems”. In: *European Biophysics Journal* 18 (1990), pp. 165–174.

[39] M. Jarrell and J. E. Gubernatis. “Bayesian inference and the analytic continuation of imaginary-time quantum Monte Carlo data”. In: *Physics Reports* 269.3 (1996), pp. 133–195.

[40] R. Levy, J. LeBlanc, and E. Gull. “Implementation of the maximum entropy method for analytic continuation”. In: *Computer Physics Communications* 215 (2017), pp. 149–155.

[41] J. Fei, C.-N. Yeh, and E. Gull. “Nevanlinna analytical continuation”. In: *Physical Review Letters* 126.5 (2021), p. 056402.

[42] G. H. Wannier. “The structure of electronic excitation levels in insulating crystals”. In: *Physical Review* 52.3 (1937), p. 191.

[43] A. J. Cohen, P. Mori-Sánchez, and W. Yang. “Insights into current limitations of density functional theory”. In: *Science* 321.5890 (2008), pp. 792–794.

[44] A.-M. Uimonen, E. Khosravi, A. Stan, G. Stefanucci, S. Kurth, R. van Leeuwen, and E. Gross. “Comparative study of many-body perturbation theory and time-dependent density functional theory in the out-of-equilibrium Anderson model”. In: *Physical Review B* 84.11 (2011), p. 115103.

[45] J. J. Phillips and D. Zgid. “Communication: The description of strong correlation within self-consistent Green’s function second-order perturbation theory”. In: *The Journal of chemical physics* 140.24 (2014).

[46] A. A. Rusakov and D. Zgid. “Second-order Green’s function perturbation theory for periodic systems”. In: *arXiv preprint arXiv:1511.03911* (2015).

[47] A. R. Welden, A. A. Rusakov, and D. Zgid. “Exploring connections between statistical mechanics and Green’s functions for realistic systems: Temperature dependent electronic entropy and internal energy from a self-consistent second-order Green’s function”. In: *The Journal of chemical physics* 145.20 (2016).

[48] S. Iskakov, A. A. Rusakov, D. Zgid, and E. Gull. “Effect of propagator renormalization on the band gap of insulating solids”. In: *Physical Review B* 100.8 (2019), p. 085112.

[49] P. Pokhilko, S. Iskakov, C.-N. Yeh, and D. Zgid. "Evaluation of two-particle properties within finite-temperature self-consistent one-particle Green's function methods: Theory and application to GW and GF2". In: *The Journal of Chemical Physics* 155.2 (2021).

[50] D. ER. "The iterativecalculationof afewof the lowesteigenvaluesand corresponding eigenvectorsof largereal-symmetric matrices". In: *Journal of Computational Physics* 17 (1975), pp. 87–94.

[51] H. Lin, J. Gubernatis, H. Gould, and J. Tobochnik. "Exact diagonalization methods for quantum systems". In: *Computers in Physics* 7.4 (1993), pp. 400–407.

[52] A. Liebsch and H. Ishida. "Temperature and bath size in exact diagonalization dynamical mean field theory". In: *Journal of Physics: Condensed Matter* 24.5 (2011), p. 053201.

[53] M. Capone, L. de'Medici, and A. Georges. "Solving the dynamical mean-field theory at very low temperatures using the Lanczos exact diagonalization". In: *Physical Review B* 76.24 (2007), p. 245116.

[54] D. Medvedeva, S. Iskakov, F. Krien, V. V. Mazurenko, and A. I. Lichtenstein. "Exact diagonalization solver for extended dynamical mean-field theory". In: *Physical Review B* 96.23 (2017), p. 235149.

[55] G. Kotliar, S. Y. Savrasov, K. Haule, V. S. Oudovenko, O. Parcollet, and C. Marianetti. "Electronic structure calculations with dynamical mean-field theory". In: *Reviews of Modern Physics* 78.3 (2006), p. 865.

[56] F. Lechermann, A. Georges, A. Poteryaev, S. Biermann, M. Posternak, A. Yamasaki, and O. Andersen. "Dynamical mean-field theory using Wannier functions: A flexible route to electronic structure calculations of strongly correlated materials". In: *Physical Review B* 74.12 (2006), p. 125120.

[57] A. Lichtenstein, M. Katsnelson, and G. Kotliar. "Finite-temperature magnetism of transition metals: An ab initio dynamical mean-field theory". In: *Physical Review Letters* 87.6 (2001), p. 067205.

[58] X. Ren, I. Leonov, G. Keller, M. Kollar, I. Nekrasov, and D. Vollhardt. "LDA+ DMFT computation of the electronic spectrum of NiO". In: *Physical Review B* 74.19 (2006), p. 195114.

[59] L. Vaugier, H. Jiang, and S. Biermann. "Hubbard U and Hund exchange J in transition metal oxides: Screening versus localization trends from constrained random phase approximation". In: *Physical Review B* 86.16 (2012), p. 165105.

[60] S. Biermann, F. Aryasetiawan, and A. Georges. "First-Principles Approach to the Electronic Structure of Strongly Correlated Systems: Combining the G W Approximation and Dynamical Mean-Field Theory". In: *Physical review letters* 90.8 (2003), p. 086402.

[61] J. M. Tomczak, M. Casula, T. Miyake, F. Aryasetiawan, and S. Biermann. "Combined GW and dynamical mean-field theory: Dynamical screening effects in transition metal oxides". In: *Europhysics Letters* 100.6 (2012), p. 67001.

[62] F. Aryasetiawan and O. Gunnarsson. "The GW method". In: *Reports on Progress in Physics* 61.3 (1998), p. 237.

[63] V. Fock. "Näherungsmethode zur Lösung des quantenmechanischen Mehrkörperproblems". In: *Zeitschrift für Physik* 61 (1930), pp. 126–148.

[64] P. Hohenberg and W. Kohn. "Inhomogeneous electron gas". In: *Physical review* 136.3B (1964), B864.

[65] W. Kohn and L. J. Sham. "Self-consistent equations including exchange and correlation effects". In: *Physical review* 140.4A (1965), A1133.

[66] L. Hedin and B. I. Lundqvist. "Explicit local exchange-correlation potentials". In: *Journal of Physics C: Solid state physics* 4.14 (1971), p. 2064.

[67] J. P. Perdew, K. Burke, and Y. Wang. "Generalized gradient approximation for the exchange-correlation hole of a many-electron system". In: *Physical review B* 54.23 (1996), p. 16533.

[68] M. Born and W. Heisenberg. "Zur quantentheorie der molekeln". In: *Original Scientific Papers Wissenschaftliche Originalarbeiten* (1985), pp. 216–246.

[69] J. Iliopoulos, C. Itzykson, and A. Martin. "Functional methods and perturbation theory". In: *Reviews of Modern Physics* 47.1 (1975), p. 165.

[70] J. Paldus et al. "Time-independent diagrammatic approach to perturbation theory of fermion systems". In: *Advances in Quantum Chemistry*. Vol. 9. Elsevier, 1975, pp. 105–197.

[71] D. Phillips and I. Afnan. "The classification of diagrams in perturbation theory". In: *Annals of Physics* 240.2 (1995), pp. 266–314.

[72] C. D. Sherrill and H. F. Schaefer III. "The configuration interaction method: Advances in highly correlated approaches". In: *Advances in quantum chemistry*. Vol. 34. Elsevier, 1999, pp. 143–269.

[73] A. Szabo and N. S. Ostlund. *Modern quantum chemistry: introduction to advanced electronic structure theory*. Courier Corporation, 2012.

[74] M. A. Marques and E. K. Gross. "Time-dependent density functional theory". In: *Annu. Rev. Phys. Chem.* 55 (2004), pp. 427–455.

[75] H. Eschrig and W. Pickett. "Density functional theory of magnetic systems revisited". In: *Solid State Communications* 118.3 (2001), pp. 123–127.

[76] K. Capelle and G. Vignale. "Nonuniqueness of the potentials of spin-density-functional theory". In: *Physical Review Letters* 86.24 (2001), p. 5546.

[77] K. Capelle and G. Vignale. "Nonuniqueness and derivative discontinuities in density-functional theories for current-carrying and superconducting systems". In: *Physical Review B* 65.11 (2002), p. 113106.

[78] E. H. Lieb. "Density functionals for Coulomb systems". In: *Inequalities: Selecta of Elliott H. Lieb* (2002), pp. 269–303.

[79] L. H. Thomas. "The calculation of atomic fields". In: *Mathematical proceedings of the Cambridge philosophical society*. Vol. 23. 5. Cambridge University Press. 1927, pp. 542–548.

[80] E. Fermi. "Eine statistische Methode zur Bestimmung einiger Eigenschaften des Atoms und ihre Anwendung auf die Theorie des periodischen Systems der Elemente". In: *Zeitschrift für Physik* 48.1-2 (1928), pp. 73–79.

[81] J. P. Perdew, R. G. Parr, M. Levy, and J. L. Balduz Jr. "Density-functional theory for fractional particle number: Derivative discontinuities of the energy". In: *Physical Review Letters* 49.23 (1982), p. 1691.

[82] J. P. Perdew and M. Levy. "Physical content of the exact Kohn-Sham orbital energies: band gaps and derivative discontinuities". In: *Physical Review Letters* 51.20 (1983), p. 1884.

[83] L. Sham and M. Schlüter. "Density-functional theory of the band gap". In: *Physical Review B* 32.6 (1985), p. 3883.

[84] R. M. Dreizler, E. K. Gross, R. M. Dreizler, and E. K. Gross. "Density functional theory of relativistic systems". In: *Density Functional Theory: An Approach to the Quantum Many-Body Problem* (1990), pp. 245–271.

[85] J. P. Perdew, K. Burke, and M. Ernzerhof. "Generalized gradient approximation made simple". In: *Physical review letters* 77.18 (1996), p. 3865.

[86] L. A. Curtiss, P. C. Redfern, and K. Raghavachari. "Assessment of Gaussian-3 and density-functional theories on the G3/05 test set of experimental energies". In: *The Journal of chemical physics* 123.12 (2005).

[87] J. P. Perdew, A. Ruzsinszky, G. I. Csonka, O. A. Vydrov, G. E. Scuseria, L. A. Constantin, X. Zhou, and K. Burke. "Restoring the density-gradient expansion for exchange in solids and surfaces". In: *Physical review letters* 100.13 (2008), p. 136406.

[88] R. S. Mulliken. "Spectroscopy, molecular orbitals, and chemical bonding". In: *Science* 157.3784 (1967), pp. 13–24.

[89] S. F. Boys. "Electronic wave functions-I. A general method of calculation for the stationary states of any molecular system". In: *Proceedings of the Royal Society of London. Series A. Mathematical and Physical Sciences* 200.1063 (1950), pp. 542–554.

[90] C. Schwartz, B. Alder, S. Fernbach, and M. Rotenberg. "Methods in Computational Physics". In: *Alder, B* (1963), p. 241.

[91] H. Taketa, S. Huzinaga, and K. O-ohata. "Gaussian-expansion methods for molecular integrals". In: *Journal of the physical society of Japan* 21.11 (1966), pp. 2313–2324.

[92] G. H. Diercksen, B. T. Sutcliffe, and A. Veillard. *Computational Techniques in Quantum Chemistry and Molecular Physics: Proceedings of the NATO Advanced Study Institute Held at Ramsau, Germany, 4–21 September, 1974*. Vol. 15. Springer Science & Business Media, 2012.

[93] L. Kleinman and D. M. Bylander. "Efficacious Form for Model Pseudopotentials". In: *Phys. Rev. Lett.* 48 (20 May 1982), pp. 1425–1428. DOI: 10.1103/PhysRevLett.48.1425. URL: https://link.aps.org/doi/10.1103/PhysRevLett.48.1425.

[94] J. M. Luttinger and J. C. Ward. "Ground-state energy of a many-fermion system. II". In: *Physical Review* 118.5 (1960), p. 1417.

[95] L. Holleboom and J. Snijders. "A comparison between the Mo/ller–Plesset and Green's function perturbative approaches to the calculation of the correlation energy in the many-electron problem". In: *The Journal of chemical physics* 93.8 (1990), pp. 5826–5837.

[96] L. Hedin. "New method for calculating the one-particle Green's function with application to the electron-gas problem". In: *Physical Review* 139.3A (1965), A796.

[97] N. W. Ashcroft and N. D. Mermin. *Solid state physics*. Cengage Learning, 2022.

[98] A. Abrikosov, L. P. Gorkov, and I. E. Dzyaloshinski. *Methods of quantum field theory in statistical physics*. Courier Corporation, 2012.

[99] C. Møller and M. S. Plesset. "Note on an approximation treatment for many-electron systems". In: *Physical review* 46.7 (1934), p. 618.

[100] K. B. Wiberg. *Ab Initio Molecular Orbital Theory by WJ Hehre, L. Radom, P. v. R. Schleyer, and JA Pople, John Wiley, New York, 548pp. Price:* 79.95(1986). 1986.

[101] J. A. Pople, J. S. Binkley, and R. Seeger. "Theoretical models incorporating electron correlation". In: *International Journal of Quantum Chemistry* 10.S10 (1976), pp. 1–19.

[102] P. Y. Ayala, K. N. Kudin, and G. E. Scuseria. "Atomic orbital Laplace-transformed second-order Møller–Plesset theory for periodic systems". In: *The Journal of Chemical Physics* 115.21 (2001), pp. 9698–9707.

[103] A. Grüneis, M. Marsman, and G. Kresse. "Second-order Møller–Plesset perturbation theory applied to extended systems. II. Structural and energetic properties". In: *The Journal of Chemical Physics* 133.7 (2010).

[104] K. Held, C. Taranto, G. Rohringer, and A. Toschi. "Hedin equations, GW, GW+ DMFT, and all that". In: *arXiv preprint arXiv:1109.3972* (2011).

[105] L. Boman, H. Koch, and A. Sánchez de Merás. "Method specific Cholesky decomposition: Coulomb and exchange energies". In: *The Journal of chemical physics* 129.13 (2008).

[106] H.-J. Werner, F. R. Manby, and P. J. Knowles. "Fast linear scaling second-order Møller-Plesset perturbation theory (MP2) using local and density fitting approximations". In: *The Journal of chemical physics* 118.18 (2003), pp. 8149–8160.

[107] X. Ren, P. Rinke, V. Blum, J. Wieferink, A. Tkatchenko, A. Sanfilippo, K. Reuter, and M. Scheffler. "Resolution-of-identity approach to Hartree–Fock, hybrid density functionals, RPA, MP2 and GW with numeric atom-centered orbital basis functions". In: *New Journal of Physics* 14.5 (2012), p. 053020.

[108] H.-Z. Ye and T. C. Berkelbach. "Fast periodic Gaussian density fitting by range separation". In: *The Journal of Chemical Physics* 154.13 (2021).

[109] O. Vahtras, J. Almlöf, and M. Feyereisen. "Integral approximations for LCAO-SCF calculations". In: *Chemical Physics Letters* 213.5-6 (1993), pp. 514–518.

[110] H. F. Schurkus and C. Ochsenfeld. "Communication: An effective linear-scaling atomic-orbital reformulation of the random-phase approximation using a contracted double-Laplace transformation". In: *The Journal of Chemical Physics* 144.3 (2016).

[111] I. Duchemin, J. Li, and X. Blase. "Hybrid and constrained resolution-of-identity techniques for coulomb integrals". In: *Journal of Chemical Theory and Computation* 13.3 (2017), pp. 1199–1208.

[112] J. Fei, C.-N. Yeh, D. Zgid, and E. Gull. "Analytical continuation of matrix-valued functions: Carathéodory formalism". In: *Physical Review B* 104.16 (2021), p. 165111.

[113] A. Georges and W. Krauth. "Numerical solution of the d=∞ Hubbard model: Evidence for a Mott transition". In: *Physical review letters* 69.8 (1992), p. 1240.

[114] M. Potthoff. "Self-energy-functional approach to systems of correlated electrons". In: *The European Physical Journal B-Condensed Matter and Complex Systems* 32 (2003), pp. 429–436.

[115] P. Maioli, T. Meunier, S. Gleyzes, A. Auffeves, G. Nogues, M. Brune, J. Raimond, and S. Haroche. "Nondestructive rydberg atom counting with mesoscopic fields in a cavity". In: *Physical review letters* 94.11 (2005), p. 113601.

[116] E. Müller-Hartmann. "Fermions on a lattice in high dimensions". In: *International Journal of Modern Physics B* 3.12 (1989), pp. 2169–2187.

[117] G. Baym. "Self-consistent approximations in many-body systems". In: *Physical review* 127.4 (1962), p. 1391.

[118] G. Baym and L. P. Kadanoff. "Conservation laws and correlation functions". In: *Physical Review* 124.2 (1961), p. 287.

[119] N. Bickers and D. Scalapino. "Conserving approximations for strongly fluctuating electron systems. I. Formalism and calculational approach". In: *Annals of Physics* 193.1 (1989), pp. 206–251.

[120] N. Bickers. "Self-consistent many-body theory for condensed matter systems". In: *Theoretical Methods for Strongly Correlated Electrons*. Springer, 2004, pp. 237–296.

[121] C. De Dominicis and P. C. Martin. "Stationary entropy principle and renormalization in normal and superfluid systems. I. Algebraic formulation". In: *Journal of Mathematical Physics* 5.1 (1964), pp. 14–30.

[122] C. De Dominicis and P. C. Martin. "Stationary entropy principle and renormalization in normal and superfluid systems. II. Diagrammatic formulation". In: *Journal of Mathematical Physics* 5.1 (1964), pp. 31–59.

[123] G. Rohringer and A. Toschi. "Impact of nonlocal correlations over different energy scales: A dynamical vertex approximation study". In: *Physical Review B* 94.12 (2016), p. 125144.

[124] E. G. van Loon, F. Krien, H. Hafermann, E. A. Stepanov, A. I. Lichtenstein, and M. I. Katsnelson. "Double occupancy in dynamical mean-field theory and the dual boson approach". In: *Physical Review B* 93.15 (2016), p. 155162.

[125] N. E. Dahlen and R. van Leeuwen. "Self-consistent solution of the Dyson equation for atoms and molecules within a conserving approximation". In: *The Journal of chemical physics* 122.16 (2005).

[126] C. Mejuto-Zaera, L. Zepeda-Núñez, M. Lindsey, N. Tubman, B. Whaley, and L. Lin. "Efficient hybridization fitting for dynamical mean-field theory via semidefinite relaxation". In: *Physical Review B* 101.3 (2020), p. 035143.

[127] E. Gull, A. J. Millis, A. I. Lichtenstein, A. N. Rubtsov, M. Troyer, and P. Werner. "Continuous-time Monte Carlo methods for quantum impurity models". In: *Reviews of Modern Physics* 83.2 (2011), p. 349.

[128] R. Bulla, T. A. Costi, and T. Pruschke. "Numerical renormalization group method for quantum impurity systems". In: *Reviews of Modern Physics* 80.2 (2008), p. 395.

[129] D. Zgid and G. K. Chan. “Dynamical mean-field theory from a quantum chemical perspective”. In: *The Journal of chemical physics* 134.9 (2011).

[130] D. Zgid, E. Gull, and G. K.-L. Chan. “Truncated configuration interaction expansions as solvers for correlated quantum impurity models and dynamical mean-field theory”. In: *Physical Review B* 86.16 (2012), p. 165128.

[131] A. Shee and D. Zgid. “Coupled cluster as an impurity solver for Green’s function embedding methods”. In: *Journal of chemical theory and computation* 15.11 (2019), pp. 6010–6024.

[132] T. Zhu, C. A. Jiménez-Hoyos, J. McClain, T. C. Berkelbach, and G. K.-L. Chan. “Coupled-cluster impurity solvers for dynamical mean-field theory”. In: *Physical Review B* 100.11 (2019), p. 115154.

[133] M. A. Branch, T. F. Coleman, and Y. Li. “A subspace, interior, and conjugate gradient method for large-scale bound-constrained minimization problems”. In: *SIAM Journal on Scientific Computing* 21.1 (1999), pp. 1–23.

[134] C. Voglis and I. Lagaris. “A rectangular trust region dogleg approach for unconstrained and bound constrained nonlinear optimization”. In: *WSEAS International Conference on Applied Mathematics*. Vol. 7. 2004, pp. 9780429081385–138.

[135] S. Iskakov and M. Danilov. “Exact diagonalization library for quantum electron models”. In: *Computer Physics Communications* 225 (2018), pp. 128–139.

[136] T. P. Hamilton and P. Pulay. “Direct inversion in the iterative subspace (DIIS) optimization of open-shell, excited-state, and small multiconfiguration SCF wave functions”. In: *The Journal of chemical physics* 84.10 (1986), pp. 5728–5734.

[137] P. Pulay. “Convergence acceleration of iterative sequences. The case of SCF iteration”. In: *Chemical Physics Letters* 73.2 (1980), pp. 393–398.

[138] P. Pulay. “Improved SCF convergence acceleration”. In: *Journal of Computational Chemistry* 3.4 (1982), pp. 556–560.

[139] P. Pokhilko, C.-N. Yeh, and D. Zgid. “Iterative subspace algorithms for finite-temperature solution of Dyson equation”. In: *The Journal of Chemical Physics* 156.9 (2022).

[140] J. R. Yates, X. Wang, D. Vanderbilt, and I. Souza. “Spectral and Fermi surface properties from Wannier interpolation”. In: *Physical Review B* 75.19 (2007), p. 195121.

[141] N. Marzari, A. A. Mostofi, J. R. Yates, I. Souza, and D. Vanderbilt. “Maximally localized Wannier functions: Theory and applications”. In: *Reviews of Modern Physics* 84.4 (2012), p. 1419.

[142] C. E. Shannon. “A mathematical theory of communication”. In: *The Bell system technical journal* 27.3 (1948), pp. 379–423.

[143] S. F. Gull and J. Skilling. “Maximum entropy method in image processing”. In: *Iee proceedings f (communications, radar and signal processing)*. Vol. 131. 6. IET. 1984, pp. 646–659.

[144] R. Nevanlinna. “Uber beschrankte Funktionen, die in gegeben Punkten vorgeschrieben Werte annehmen”. In: *Ann. Acad. Sci. Fenn. Ser. A 1 Mat. Dissertationes* (1919).

[145] G. A. Baker and P. R. Graves-Morris. “Padé Approximants Second Edition: Extensions of Padé approximants”. In: 1996. URL: https://api.semanticscholar.org/CorpusID:119049321.

[146] J. Schur. “Über Potenzreihen, die im Innern des Einheitskreises beschränkt sind.” In: *Journal für die reine und angewandte Mathematik (Crelles Journal)* 1918.148 (1918), pp. 122–145.

[147] V. M. Adamyan, J. Alcober, and I. Tkachenko. “Reconstruction of distributions by their moments and local constraints”. In: *Applied Mathematics Research eXpress* 2003.2 (2003), pp. 33–70.

[148] G. S. Ammar and W. B. Gragg. “The generalized Schur algorithm for the superfast solution of Toeplitz systems”. In: *Rational Approximation and its Applications in Mathematics and Physics*. Ed. by J. Gilewicz, M. Pindor, and W. Siemaszko. Berlin, Heidelberg: Springer Berlin Heidelberg, 1987, pp. 315–330. ISBN: 978-3-540-47412-8.

[149] V. M. Galitskii and A. B. Migdal. “Application of quantum field theory methods to the many body problem”. In: *Sov. Phys. JETP* 7.96 (1958), p. 18.

[150] B. Holm and F. Aryasetiawan. “Total energy from the Galitskii-Migdal formula using realistic spectral functions”. In: *Physical Review B* 62.8 (2000), p. 4858.

[151] N. E. Dahlen, R. van Leeuwen, and U. von Barth. “Variational energy functionals of the Green function and of the density tested on molecules”. In: *Physical Review A* 73.1 (2006), p. 012511.

[152] T. Pruschke, D. L. Cox, and M. Jarrell. “Hubbard model at infinite dimensions: Thermodynamic and transport properties”. In: *Physical Review B* 47.7 (1993), p. 3553.

[153] M. Jarrell, J. K. Freericks, and T. Pruschke. “Optical conductivity of the infinite-dimensional Hubbard model”. In: *Physical Review B* 51.17 (1995), p. 11704.

[154] M. Rozenberg, G. Kotliar, H. Kajueter, G. Thomas, D. Rapkine, J. Honig, and P. Metcalf. “Optical conductivity in Mott-Hubbard systems”. In: *Physical review letters* 75.1 (1995), p. 105.

[155] M. Rozenberg, G. Kotliar, and H. Kajueter. "Transfer of spectral weight in spectroscopies of correlated electron systems". In: *Physical Review B* 54.12 (1996), p. 8452.

[156] N. Blümer. *Mott Hubbard Metal Insulator Transition and Optical Conductivity in High Dimensions*. Citeseer, 2003.

[157] N. Blümer and P. G. Van Dongen. "Transport Properties of Correlated Electrons in High Dimensions: Proceedings of the ARW NATO Workshop Hvar, Croatia, October 2002". In: *Concepts in Electron Correlation* (2003), pp. 335–343.

[158] G. Palsson. *Computational studies of thermoelectricity in strongly correlated electron systems*. Rutgers The State University of New Jersey, School of Graduate Studies, 2001.

[159] V. Oudovenko, G. Palsson, S. Savrasov, K. Haule, and G. Kotliar. "Calculations of optical properties in strongly correlated materials". In: *Physical Review B* 70.12 (2004), p. 125112.

[160] C. Berthod. "Applications of the Many-Body Formalism in Condensed-Matter Physics". In: *Lecture Notes, University of Geneva* (2009).

[161] G. D. Mahan. *Many-particle physics*. Springer Science & Business Media, 2013.

[162] P. Coleman. *Introduction to many-body physics*. Cambridge University Press, 2015.

[163] M. Dresselhaus. "Solid state physics part ii optical properties of solids". In: *Lecture Notes (Massachusetts Institute of Technology, Cambridge, MA)* 17 (2001).

[164] M. Osada, B. Y. Wang, B. H. Goodge, K. Lee, H. Yoon, K. Sakuma, D. Li, M. Miura, L. F. Kourkoutis, and H. Y. Hwang. "A superconducting praseodymium nickelate with infinite layer structure". In: *Nano letters* 20.8 (2020), pp. 5735–5740.

[165] G. A. Pan, D. Ferenc Segedin, H. LaBollita, Q. Song, E. M. Nica, B. H. Goodge, A. T. Pierce, S. Doyle, S. Novakov, D. Córdova Carrizales, et al. "Superconductivity in a quintuple-layer square-planar nickelate". In: *Nature materials* 21.2 (2022), pp. 160–164.

[166] Z. Liu, Z. Ren, W. Zhu, Z. Wang, and J. Yang. "Electronic and magnetic structure of infinite-layer NdNiO2: trace of antiferromagnetic metal". In: *npj Quantum Materials* 5.1 (2020), p. 31.

[167] M. Hepting, D. Li, C. Jia, H. Lu, E. Paris, Y. Tseng, X. Feng, M. Osada, E. Been, Y. Hikita, et al. "Electronic structure of the parent compound of superconducting infinite-layer nickelates". In: *Nature materials* 19.4 (2020), pp. 381–385.

[168] B. H. Goodge, D. Li, K. Lee, M. Osada, B. Y. Wang, G. A. Sawatzky, H. Y. Hwang, and L. F. Kourkoutis. "Doping evolution of the Mott–Hubbard landscape in infinite-layer nickelates". In: *Proceedings of the National Academy of Sciences* 118.2 (2021), e2007683118.

[169] D. Li, B. Y. Wang, K. Lee, S. P. Harvey, M. Osada, B. H. Goodge, L. F. Kourkoutis, and H. Y. Hwang. "Superconducting dome in Nd 1- x Sr x NiO 2 infinite layer films". In: *Physical review letters* 125.2 (2020), p. 027001.

[170] M. Osada, B. Y. Wang, K. Lee, D. Li, and H. Y. Hwang. "Phase diagram of infinite layer praseodymium nickelate Pr 1- x Sr x NiO 2 thin films". In: *Physical Review Materials* 4.12 (2020), p. 121801.

[171] S. Zeng, C. S. Tang, X. Yin, C. Li, M. Li, Z. Huang, J. Hu, W. Liu, G. J. Omar, H. Jani, et al. "Phase diagram and superconducting dome of infinite-layer Nd 1- x Sr x NiO 2 thin films". In: *Physical Review Letters* 125.14 (2020), p. 147003.

[172] Y. Gu, S. Zhu, X. Wang, J. Hu, and H. Chen. "A substantial hybridization between correlated Ni-d orbital and itinerant electrons in infinite-layer nickelates". In: *Communications Physics* 3.1 (2020), p. 84.

[173] A. S. Botana and M. R. Norman. "Similarities and differences between LaNiO 2 and CaCuO 2 and implications for superconductivity". In: *Physical Review X* 10.1 (2020), p. 011024.

[174] J. Kapeghian and A. S. Botana. "Electronic structure and magnetism in infinite-layer nickelates R NiO 2 (R= La- Lu)". In: *Physical Review B* 102.20 (2020), p. 205130.

[175] P. Jiang, L. Si, Z. Liao, and Z. Zhong. "Electronic structure of rare-earth infinite-layer R Ni O 2 (R= La, Nd)". In: *Physical Review B* 100.20 (2019), p. 201106.

[176] M. Jiang, M. Berciu, and G. A. Sawatzky. "Critical nature of the Ni spin state in doped NdNiO 2". In: *Physical Review Letters* 124.20 (2020), p. 207004.

[177] F. Lechermann. "Late transition metal oxides with infinite-layer structure: Nickelates versus cuprates". In: *Physical Review B* 101.8 (2020), p. 081110.

[178] J. Zaanen, G. Sawatzky, and J. Allen. "Band gaps and electronic structure of transition-metal compounds". In: *Physical review letters* 55.4 (1985), p. 418.

[179] F. Petocchi, V. Christiansson, F. Nilsson, F. Aryasetiawan, and P. Werner. "Normal State of Nd 1- x Sr x NiO 2 from Self-Consistent G W+ EDMFT". In: *Physical Review X* 10.4 (2020), p. 041047.

[180] A. V. Krukau, O. A. Vydrov, A. F. Izmaylov, and G. E. Scuseria. "Influence of the exchange screening parameter on the performance of screened hybrid functionals". In: *The Journal of chemical physics* 125.22 (2006).

[181] A. D. Becke. “Density-functional thermochemistry. I. The effect of the exchange-only gradient correction”. In: *The Journal of chemical physics* 96.3 (1992), pp. 2155–2160.

[182] P. J. Stephens, F. J. Devlin, C. F. Chabalowski, and M. J. Frisch. “Ab initio calculation of vibrational absorption and circular dichroism spectra using density functional force fields”. In: *The Journal of physical chemistry* 98.45 (1994), pp. 11623–11627.

[183] B. G. Janesko, T. M. Henderson, and G. E. Scuseria. “Screened hybrid density functionals for solid-state chemistry and physics”. In: *Physical Chemistry Chemical Physics* 11.3 (2009), pp. 443–454.

[184] P. J. Hay, R. L. Martin, J. Uddin, and G. E. Scuseria. “Theoretical study of CeO2 and Ce2O3 using a screened hybrid density functional”. In: *The Journal of chemical physics* 125.3 (2006).

[185] J. L. Da Silva, M. V. Ganduglia-Pirovano, J. Sauer, V. Bayer, and G. Kresse. “Publisher’s Note: Hybrid functionals applied to rare-earth oxides: The example of ceria [Phys. Rev. B 75, 045121 (2007)]”. In: *Physical Review B* 75.8 (2007), p. 089901.

[186] J. Hong, A. Stroppa, J. Íniguez, S. Picozzi, and D. Vanderbilt. “Spin-phonon coupling effects in transition-metal perovskites: A DFT+ U and hybrid-functional study”. In: *Physical Review B* 85.5 (2012), p. 054417.

[187] R. Dovesi, V. Saunders, C. Roetti, R. Orlando, C. Zicovich-Wilson, F. Pascale, B. Civalleri, K. Doll, N. Harrison, I. Bush, et al. “CRYSTAL17”. In: (2017).

[188] Y. Yu, S. Iskakov, and E. Gull. “Heating and cooling in self-consistent many-body simulations”. In: *arXiv preprint arXiv:2305.01452* (2023).

[189] M.-Y. Choi, K.-W. Lee, and W. E. Pickett. “Role of 4 f states in infinite-layer NdNiO 2”. In: *Physical Review B* 101.2 (2020), p. 020503.

[190] R. Zhang, C. Lane, B. Singh, J. Nokelainen, B. Barbiellini, R. S. Markiewicz, A. Bansil, and J. Sun. “Magnetic and f-electron effects in LaNiO2 and NdNiO2 nickelates with cuprate-like 3 dx 2- y 2 band”. In: *Communications Physics* 4.1 (2021), p. 118.

[191] H. Chen, A. Hampel, J. Karp, F. Lechermann, and A. J. Millis. “Dynamical mean field studies of infinite layer nickelates: Physics results and methodological implications”. In: *Frontiers in Physics* 10 (2022), p. 835942.

[192] P. Császár and P. Pulay. “Geometry optimization by direct inversion in the iterative subspace”. In: *Journal of Molecular Structure* 114 (1984), pp. 31–34.

[193] X. Li, J. M. Millam, G. E. Scuseria, M. J. Frisch, and H. B. Schlegel. "Density matrix search using direct inversion in the iterative subspace as a linear scaling alternative to diagonalization in electronic structure calculations". In: *The Journal of chemical physics* 119.15 (2003), pp. 7651–7658.

[194] J. Karp, A. S. Botana, M. R. Norman, H. Park, M. Zingl, and A. Millis. "Many-body electronic structure of NdNiO 2 and CaCuO 2". In: *Physical Review X* 10.2 (2020), p. 021061.

[195] J. Karp, A. Hampel, M. Zingl, A. S. Botana, H. Park, M. R. Norman, and A. J. Millis. "Comparative many-body study of Pr 4 Ni 3 O 8 and NdNiO 2". In: *Physical Review B* 102.24 (2020), p. 245130.

[196] Y. Wang, C.-J. Kang, H. Miao, and G. Kotliar. "Hund's metal physics: From SrNiO 2 to LaNiO 2". In: *Physical Review B* 102.16 (2020), p. 161118.

[197] J. Karp, A. Hampel, and A. J. Millis. "Dependence of DFT+ DMFT results on the construction of the correlated orbitals". In: *Physical Review B* 103.19 (2021), p. 195101.

[198] T. Liu, H. Wu, T. Jia, X. Zhang, Z. Zeng, H. Lin, and X. Li. "Dimensionality-induced insulator-metal crossover in layered nickelates Lan+ 1NinO2n+ 2 (n= 2, 3, and∞)". In: *Aip Advances* 4.4 (2014).

[199] G. A. Sawatzky. *Superconductivity seen in a non-magnetic nickel oxide*. 2019.

[200] Y. Shen, J. Sears, G. Fabbris, J. Li, J. Pelliciari, I. Jarrige, X. He, I. Bo žovi ć, M. Mitrano, J. Zhang, J. F. Mitchell, A. S. Botana, V. Bisogni, M. R. Norman, S. Johnston, and M. P. M. Dean. "Role of Oxygen States in the Low Valence Nickelate $La_4Ni_3O_8$". In: *Phys. Rev. X* 12 (1 Mar. 2022), p. 011055. DOI: 10.1103/PhysRevX.12.011055. URL: https://link.aps.org/doi/10.1103/PhysRevX.12.011055.